

## Survey article

# Computational vascular fluid dynamics: problems, models and methods

Alfio Quarteroni<sup>1,2</sup>, Massimiliano Taveri<sup>3,4</sup>, Alessandro Veneziani<sup>5</sup>

<sup>1</sup> Dipartimento di Matematica “F. Brioschi”, Politecnico di Milano, Piazza Leonardo da Vinci 32, I-20133 Milano, Italy

<sup>2</sup> Département de Mathématiques, École Polytechnique Fédérale de Lausanne, CH-1015, Lausanne, Switzerland

<sup>3</sup> Centro di Ricerca, Sviluppo e Studi Superiori in Sardegna (CRS4), Via N. Sauro 10, I-09123 Cagliari, Italy

<sup>4</sup> Clinica “S.Elena”, Viale Marconi 160, Quartu S’Elena, I-09123 Cagliari, Italy

<sup>5</sup> Dipartimento Scientifico e Tecnologico, Università degli Studi di Verona Ca’ Vignal 2, Strada Le Grazie, I-37134 Verona, Italy

Received: 10 December 1998 / Accepted: 30 August 1999

Communicated by: G. Wittum

## 1 Introduction

In the cardiovascular system, morphology and functionality are closely related. Altered flow conditions, such as separation and flow-reversal zones, low and oscillatory shear-stress zones, play an important role in the development of arterial disease. In turn, all these flow conditions are modified by arterial wall changes such as intimal thickening or atherosclerotic plaques. A detailed understanding of the local hemodynamic environment, the influence of wall modifications on flow patterns and the long-term adaptations of the vascular wall after surgical procedures can have useful clinical applications, especially in view of reconstruction and revascularization operations. Some of these alterations are not well understood, making it quite difficult to foresee short- and long-term evolution of the atherosclerotic disease and to plan an aggressive approach. Recent advances in data-acquisition technology are now providing physicians with large amounts of quantitative information on vascular geometry that, together with the availability of sophisticated three-dimensional simulation methods, can be used to build patient-parametrized models able to give detailed predictions on, e.g., flow shears stresses and zones of recirculation in the arterial wall regions.

In the past, the adoption of mathematical investigation was discouraged because of the difficulty of devising significant mathematical models of the cardiovascular system and, in particular, of the flow in specific districts where atherosclerosis arises. Several types of difficulties have so far limited the applicability of mathematical models to simple paradigms such as flow in morphologically simple districts (e.g. Poiseuille or Womersley solutions) or those based on electric network analogies (see e.g. [93, 119]). The complexity is due on the one hand to strong nonlinear interactions among different parts of the system; on the other hand, it arises from the wide variety of individual vascular morphologies.

Still in the Seventies, experiments on *in vitro* models or on animals were the main device for cardiovascular investigations (see e.g. [123]). In recent years, however, the development of computational techniques in fluid dynamics (CFD), together with the increasing performances of the hardware,

found a promising field of application in the framework of vascular research (see e.g. [48, 74, 79, 82, 91, 111, 114]). Indeed, CFD allows the carrying out of simulations at low costs and in completely controlled conditions. Besides, physical quantities that are troublesome to measure “in vivo” can be computed using real geometries, with the support of modern medical imaging devices (such as, e.g., the Nuclear Magnetic Resonance, the Digital Subtraction Angiography, the Spiral Computed Tomography) and 3D geometrical reconstruction algorithms (see e.g. [80, 114]).

Three different issues are relevant to this subject and will be mainly addressed in this note.

1. *Definition of suitable mathematical models*: due to the complexity of the cardiovascular system, a preliminary analysis aiming at introducing suitable simplifying assumptions in the mathematical modelling process is mandatory. Obviously, different kind of simplifications are suitable for different vascular districts. These issues will be discussed in Sect. 3 for blood, and Sect. 4 for the vascular walls, with a particular emphasis on large- and medium-sized vessels, where atherosclerosis usually develops.
2. *Preprocessing of clinical data*: the suitable treatment of clinical data is crucial for the definition of a real (i.e. taken from a patient) geometrical model, which is of utmost importance for the meaningfulness of numerical results. This aspect demands geometrical reconstruction algorithms in order to achieve simulation in real vascular morphologies. We briefly consider this issue in Sect. 3.4.
3. *Development of appropriate numerical techniques*: the geometrical complexity of the vascular districts suggests the use of unstructured grids (in particular for Finite Element Method (FEM)), while the strongly unsteady nature of the problem demands effective time-advancing methods. In particular, for the numerical simulation of the flow equations in a vascular district, fractional step methods that separate the computation of velocity from that of pressure field seem to be adequately accurate and computationally effective (see Sect. 5.1).

When the compliance of the vascular walls is taken into account, specific techniques such as the *Arbitrary Lagrangian Eulerian* (ALE) method for the numerical solution of the fluid equations in moving domains have to be used and will be considered in Sect. 5.2 and Sect. 5.3. Finally, in Sect. 5.4 it is considered the coupling of the equation for the fluid in ALE formulation and those for the vessel walls, in view of the numerical simulation of the fluid-structure interaction problems.

The virtual hemodynamic environment based on mathematical models, preprocessing of clinical data and numerical devices, as described in this note, provides the physicians approaching this complex bio-medical field with different options, among which we mention: the understanding of the intimate correlation between any modification of vessel morphology and the associated alteration of flow patterns, with its impact on long-term results; the basis for a sophisticated planning, before performing real procedures on the patient; the possibility of altering vascular geometries in order to study or foresee end-results of any vascular procedure (see also [1] and [114]).

The numerical results addressed at the end of this work demonstrate the potentiality of these interdisciplinary studies.

## 2 Physiological aspects of the cardiovascular system

In this Section we analyze some basic features of the pathophysiology of blood flow and vessel walls.

The major functions of the cardiovascular system are to distribute metabolites and oxygen to all body cells and to collect waste products and carbon dioxide for excretion. The heart provides the driving force for this system, the arteries serve as distribution channels to the organs. The arteries have to adapt timely to the peripheral organ demands, following the changing conditions of pressure and flow. To fulfil this function, the aorta and large arteries have thick walls with high collagen and elastin contents and function primarily to deliver and distribute blood under high pressure to the various tissue beds. They also accommodate the stroke volume of the heart because of their distensibility. In addition to the vessel being distensible, the elastic recoil provides pressure to maintain blood flow during the diastolic phase of the cardiac cycle (see [37]).

Small arteries and arterioles, with larger proportions of smooth muscle, act as variable resistors, driving blood flow to individual organs and tissue beds according to changing local

**Table 1.** Relationship between arterial size, number of arteries and cross-sectional area (see [3])

Vessel	Radius (cm)	Number	Area (cm <sup>2</sup> )	Wall thickness (cm)
Aorta	1.25	1	4.5	0.2
Arteries	0.2	159	20	0.1
Arterioles	$1.5 \times 10^{-3}$	$5.7 \times 10^7$	400	$2 \times 10^{-3}$
Capillaries	$3 \times 10^{-4}$	$1.6 \times 10^{10}$	4500	$1 \times 10^{-4}$
Venules	$1 \times 10^{-3}$	$1.3 \times 10^9$	4000	$2 \times 10^{-4}$
Veins	0.25	200	40	0.05
Vena cava	1.5	1	18	0.15

**Table 2.** Endothelial responses to shear stress as determined in vitro cell culture studies

Phenomena	Reference
cell-shape modifications	[21, 55]
cell-orientation modifications	[21, 55]
cytoskeletal organization	[122]
mechanical stiffness modifications	[110]
cell proliferation	[58]
secretion of vasoactive substances	[31, 59, 102]
transendothelial transport	[107]
intracellular signaling	[77, 102]

needs. These vessels have a relatively large lumen-to-wall-thickness ratio, so as to minimize the pressure drop due to resistance losses (see Table 1).

Arteries are formed by three layers: an *intima*, a *media* and an *adventitia*. Each segment of the circulation has an ideal combination of size, wall composition, wall thickness and cross-sectional area that best fulfils its function. These layers form a morpho-functional unity, being able to influence each other reciprocally.

The intima consists of a thin monolayer of *endothelial cells*, usually oriented along the direction of blood flow. Beneath the endothelium there is the *basal lamina*, a fibrillar layer which binds the endothelium to the subendothelial tissue. The *internal elastic lamina* separates the intima from the media which is rich in *elastin* and *smooth muscle cells*. The adventitia is separated from the media by an *external elastic lamina* (see Fig. 1).

### 2.1 Endothelium in its environment

Endothelial cells form a monolayer that constitutes the primary interface between the bloodstream and all extravascular tissue. It is strategically located to serve as a sensory tissue assessing hemodynamic conditions such as blood flow and pressure (see [130]).

Endothelial cells are subjected to forces induced by the blood, which for the sake of convenience we divide into shear

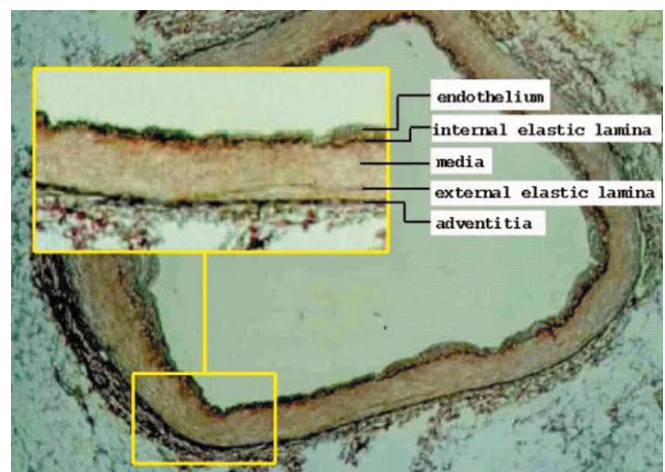


**Fig. 1.** Wall of an artery in cross-section, showing the concentric arrangement of tunica intima, media, and adventitia. The lumen is large, without any narrowing by atheromatous plaque. Silver stained (40X)

stress, pressure and circumferential stress. Once dismissed as a passive interface between the bloodstream and the tissue, the endothelium is increasingly being recognized as an important modulator of such different processes as blood-vessel remodeling, regulation of vascular tone, smooth-muscle-cell migration and atherogenesis (see [64,65]). Given its role as a regulator of the vascular wall, any dysfunction, usually caused by metabolic, mechanical or immunologic injuries, may have profound effects on vascular integrity and function. It is now well known that hemodynamics influences cell morphology, orientation, cell function, cell turnover rate and transendothelial transport of this cellular interface (see Table 2). The change in orientation, shape and secretion does not occur immediately with the onset of the hemodynamic stimulation (see [71]), rather after few minutes. Some phenomena, such as elongation and proliferation, proceed at a slower rate (see [105]).

The endothelial cell acts mostly as a wall stress sensor. Hemodynamic forces play an important role in stimulating vascular remodeling and the development of lesions. In response to the hemodynamic solicitations, the endothelium synthesizes and secretes biologically active substances that control smooth-muscle-cell tone, vessel diameter and wall composition. Experimental data show that arteries, in regions of denuded endothelium, lose the capacity to adapt their diameter in response to modifications of blood flow. This implies the lack of production of important factors by the endothelium, that allow the vessel wall to adapt timely to modified flow patterns (see [52]).

In recent years, experiments have shown the same importance of the *cyclic stretch* that acts on endothelial cells. Exposure of endothelial cells to cyclic stretch elicited rapid, however sometimes transient, modifications of their shape, secretion and permeability (see [32, 71, 94, 104]).

New discoveries of how vascular cells transduce the hemodynamic forces to which they respond have been reported. Force-sensitive gene transcription occurs by well characterized transcription factors that bind to both estab-

lished and novel responsive elements in promoter regions of relevant genes (see [16]). In particular, two proteins, endothelin-1 and endothelial constitutive nitric oxide synthase, seem to be mechanical-force-dependent and depend directly on the levels of shear stress.

## 2.2 Smooth muscle cell in its environment

The *media* comprises smooth muscle cells oriented circumferentially, in an elastin and collagen matrix, which may be up to 500  $\mu\text{m}$  thick. It consists of smooth muscle cells and elastin fibers in alternating layers forming lamellar units. Each unit is composed of a smooth muscle cell with elastin fibers on either side. The elastin fibers permit distension of the artery while the collagen bundles provide tensile strength, limit distension and prevent disruption.

These overlapping musculo-elastic fascicles are usually aligned in the direction of resultant tensile forces at any given location and the size is closely related to the vessel-wall curvature. This organization corresponds to the distribution and magnitude of tensile stress (see [29]). A deviation from this orientation may reflect a non-null axial component of the tensile stress. In particular the tensile stress depends on the distance from the heart, the artery diameter and pressure. The thickness of the media decreases with distance from the heart, in keeping with the decrease in radius and consequently in tangential tension. Chronic high pressure levels determine adaptive changes in resistance vessels that are characterized by smooth-muscle-cell hypertrophy and hyperplasia, increased extracellular matrix, increased stiffness and resistance to stress (see [38]).

The contraction of smooth-muscle-cell can increase wall stiffness. This effect may be offset by the reduction of the arterial size and shift stress bearing from the stiff collagen fibers to the more distensible elastin fibers. This behavior would be at the basis of the negligible increase in overall wall stress without any increase in the incremental elastic modulus (see [9, 10]). Such a capacity of modulating smooth-muscle-cell tone, while allowing acute arterial diameter reduction, protects the artery from dramatic pressure elevations. These changes of the blood pressure are usually associated with changes in wall thickness. More precisely, the remodeling is achieved by proliferation of the smooth-muscle cell without altering the vessel length. Data demonstrate that wall expansion usually associated with rapid vessel enlargement involves hyperplasia of both endothelial cells and smooth muscle cells: however smooth-muscle-cell proliferation does not occur until after wall shear stress is reduced (see [115]). The specific cellular adaptations that occur during dramatic arterial enlargement (e.g. the creation of an arterio-venous fistula) may depend on the level of wall shear stress and shear-dependent modulation of endothelial growth factors (see [109, 130]). Such an adaptation usually implies a smooth-muscle-cell activation that consists of a shift of the smooth-muscle-cell from a contractile to a synthetic phenotype with proliferation, migration and synthesis of extracellular matrix. Some of these smooth-muscle-cell are resident in the intima, but a large amount of them get to the intima from the adventitia (see [98, 106]).

Experimental models able to show this migration of smooth-muscle-cell to subintimal space are balloon dilations

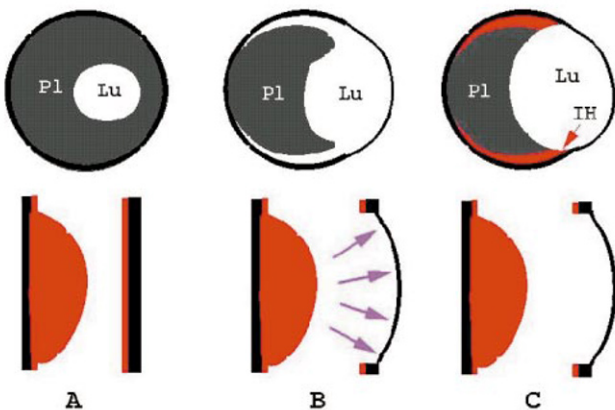


**Fig. 2.** Pl = plaque; Lu = lumen. In **A**, a plaque narrowing the arterial lumen is shown. In **B**, the artery after wall disruption. The tunica media has ruptured by the action of the balloon catheter and the tunica adventitia (pink) has been stretched. Lumen integrity is always maintained by the tunica adventitia, now alone responsible for the mechanical strength in that part of the wall. In **C**, remodeling after balloon dilatation. Intimal hyperplasia (red) occurs early but in this phase the lumen maintains a larger area and a new flow pattern has established itself

performed in endovascular surgery, in which the atherosclerotic intima is ruptured and partially dehisced (Fig. 2A). This frees the media from the restraint of the atherosclerotic intima, allowing it to become overstretched with damage to the elastic properties of its elastic collagen and muscle fibers (see [40, 128]). The increased blood flow through the lesion keeps the media distended as it heals by collagen deposition. The first step after this injury is the proliferation and migration of smooth muscle cells in the subintimal space from the adventitia where deposition of matrix fibers occurs (Fig. 2B – see [106]).

Most of these reactions are strictly controlled and regulated by the endothelium. This influence is evident during increases of blood-flow rate, in which the artery increases its size or in the early phases of arterial disease, in which a wall remodeling occurs. Flow would modulate the smooth muscle cells' proliferative response, suggesting that arterial healing (with the associated morphological changes) would be affected by the wall shear stress levels (see [6]).

### 2.3 The adventitia in its environment

The adventitia is separated from the media, in most arteries, by the external elastic lamina. The adventitia consists of sparse fibroblasts with layers of elastin and collagen fibers, which add further mechanical strength to the wall. This role is particularly evident after *endarterectomy* (i.e. the resection of a plaque), in which the reduction in the wall thickness (usually about one third of its original size) is not accompanied by the expected increase in tangential stress, indicating clearly that the components responsible for the mechanical strength are located in the remaining outer layers of the arterial wall (see [126]).

The adventitia is a site in which important metabolic and proliferation processes occur. Studies performed after *angioplasty* (i.e. forced modifications of the vascular walls) have clearly shown that the first major site of cell proliferation within 2–3 days after angioplasty is the adventitia and not the medial wall. Only seven days after angioplasty, cell proliferation is predominant in the neointima and is reduced in the media and adventitia. The proliferating adventitial cells are myofibroblasts that migrate into the neointima and contribute to the mass of restenosis lesion. These myofibroblasts contribute to the problem of post-angioplasty restenosis by proliferating, thus forming a fibrotic scar surrounding the angioplastied site and migrating in the neointima (see [106]).

### 2.4 Intimal thickening

Arterial wall integrity, as well as atherogenesis development, needs a normal endothelial sheet. Such an integrity depends mainly on the maintenance in large arteries of normal levels of two components: *wall shear stress* (approximately  $15 \text{ dynes cm}^{-2}$ ), tangential to the wall, which depends on the blood flow, viscosity and radius of the vessel; and *tensile stress* (approximately  $1000\text{--}2000 \text{ dynes cm}^{-1}$ ), normal to the wall, which is equal to wall tension divided by the wall thickness. Generally, the arterial thickness changes proportionally to the wall tension in order to maintain the tensile stress at a baseline level (see [29, 51]).

The endothelial cell “sees” pressure (as tensile stress) directly and “rides” on its basal membrane, being cyclically stretched by the pulsatile behavior of blood flow. However, the endothelial cells “feel” the wall shear stress more than the tensile stress, even if the former is of smaller magnitude. Therefore, the endothelium would act essentially as a shear-stress sensor, mediating both the normal response and the variety of vascular disease. There is a wide range in the level of wall shear stress to which the endothelial cells are exposed. The highest levels are encountered at the region of the flow divider of any bifurcation of large vessels; lowest values are usually measured on the opposite side with respect to the flow divider of bifurcations of normal vessels, (e.g. at the carotid sinus), in which wall shear stress can be negative or oscillating both spatially and temporally (see [38, 61, 118]).

Kamiya and Togawa first showed that arterial thickening served essentially to restore vessel stresses to within normal levels (see [52]). Intimal thickening is a morphological change of the arterial wall characterized by an intimal deposition of matrix fibers, myofibroblasts and smooth-muscle-cell. Wall thickening appears to be the ultimate fate of any arterial modification due to altered flow patterns (Fig. 3). Indeed, reduction of blood-flow velocity (with low wall shear stress) is considered a stimulus for *intimal thickening* with consequent lumen narrowing and normalization of wall shear stress. Increases in blood-flow velocity determine an increase in lumen radius that results in an arterial enlargement until a restitution to the baseline wall shear stress occurs. The arterial enlargement is always followed by a *medial thickening* in order to compensate the increase in wall tension. Intimal thickening, whether or not followed by medial rearrangement, occurs preferentially at the site of low or oscillating shear stress, such as the inlet side of branch ostia or on the opposite side with respect to the flow divider in the internal carotid artery. In this site, intimal thickening and plaque depositions tend to localize in the outer wall of the carotid sinus, a region of low and oscillating shear stress and high particle residence time. The flow divider, characterized by axial flow and high wall shear stress levels, is usually spared from lesions.

Another important site of deposition of intimal thickening is the end-to-side vascular-bypass graft, in which the end of a graft is connected to the side of a host vessel. This deposition at this site is a primary cause of short-term graft failure.

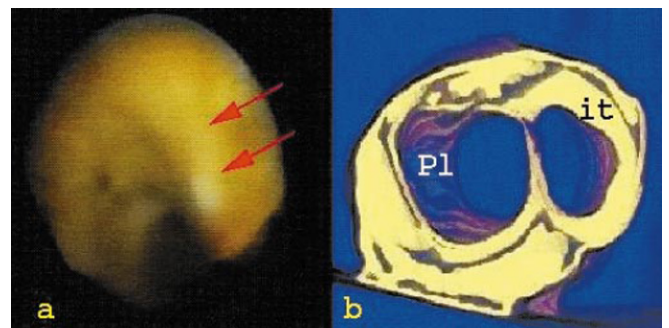


**Fig. 3a,b.** In **a**, the angioscopic view shows an intact endothelial sheet of an autoptic specimen of carotid bifurcation. The red arrows show an intimal thickening localized in the external wall of the external carotid artery. In **b**, (it) shows the wall lesion in a 3D reconstruction of the same arterial specimen seen from above; (Pl) shows a large fibrotic plaque narrowing the lumen of the internal carotid artery

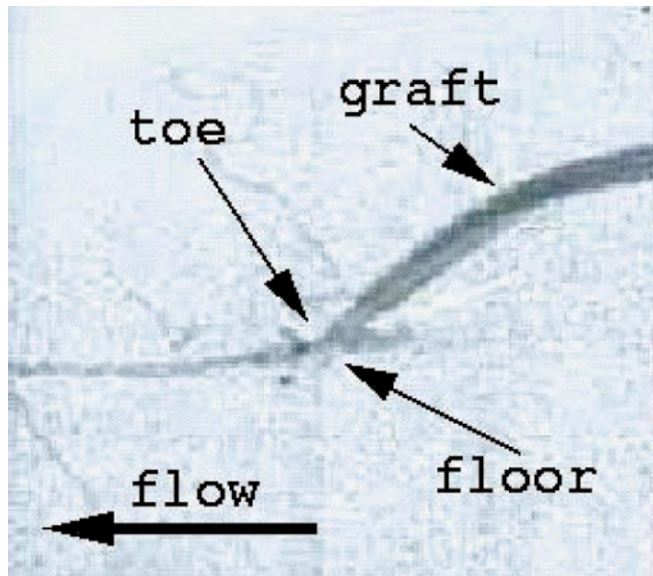
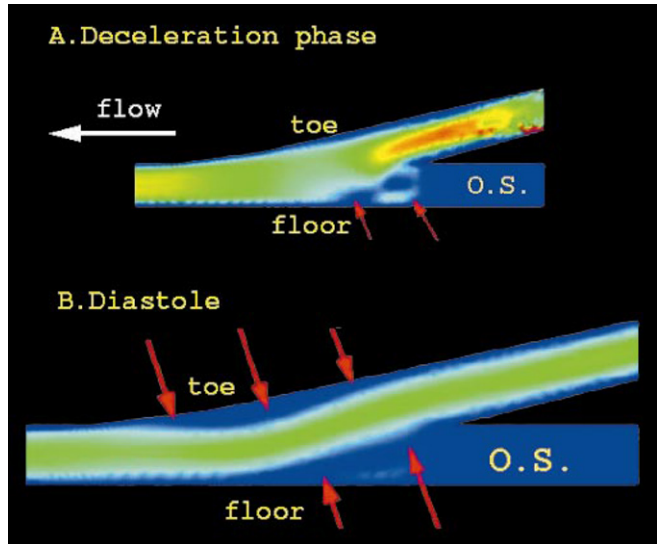


**Fig. 4.** The angiogram shows the localization of advanced atherosclerotic plaques in an end-to-side vascular by-pass graft. Atherosclerotic depositions are localized more often at the toe and at the floor of the graft, in which an altered flow pattern occurs. The picture shows the reconstruction of a parametrized model of the same type of vascular graft. A separation zone begins in the early deceleration phase at the floor of the anastomosis **A** and becomes larger involving also the toe of the graft in the diastole **B**



The healing process and graft mismatch are often invoked to explain the early failure of the graft. However, the localization of lesions at the toe and at the floor of the graft-junction suggests that the hemodynamic factors are quite relevant. These regions of intimal thickening correspond to regions of flow oscillation and relatively low wall shear stress (Fig. 4 – see [8] and also Sect. 6.3 and Sect. 6.4).

An interesting aspect appears to be the role of endothelial cells and intimal thickening in the healing process after a vascular procedure. Animal model studies on restenosis after angioplasty showed that areas where the endothelial sheet has rapidly regenerated have less marked intimal thickening than areas in which endothelial regeneration occurs later or was incomplete. These properties of the endothelium are very critical for the prevention of luminal narrowing due to neointimal thickening (see [6, 67]), given its ability to modulate the healing process after any procedure. Anyway, endothelial-cell dysfunction may often occur at sites of regenerating endothelium. This impairment in the endothelial-cell function may be considered one of the major regulatory elements in the restenotic process (see [63]).

As intimal thickening proceeds due to unresolved modification of flow patterns, arteries tend to preserve lumen cross-sectional area. This compensatory enlargement can prevent narrowing of the arterial lumen, and the stenosis may be delayed until the lesion occupies 40% of the internal elastic lamina (see [36, 130]).

A diseased artery, e.g. coronary artery, thus dilates and maintains normal luminal dimensions despite changes in wall structure as long as the intimal lesion does not exceed 40% of the area encompassed by the internal elastic lamina. Beyond this point, pathological narrowing begins (*Glagov phenomenon*) (Fig. 6 – see [47, 108]).

The internal elastic lamina represents the potential lumen area, which is what the actual lumen area would be if there was no plaque (Fig. 5 – see [108]). This intimal enlargement leads to an important underestimation of stenosis up to an an-

giographically determined degree of approximately 50% area stenosis and 30% diameter stenosis. This observation shows that compensatory enlargement is a major source of error in the assessment of coronary lesions by angiography. The nature of this compensatory enlargement is not completely clear. The limit of this enlargement may be related to the progression of the plaque density or to the rigidity of the arterial wall. However, it could also be explained by the mechanical behavior of the wall in order to balance the changed levels of both wall shear stress and tensile stress (see [61]).

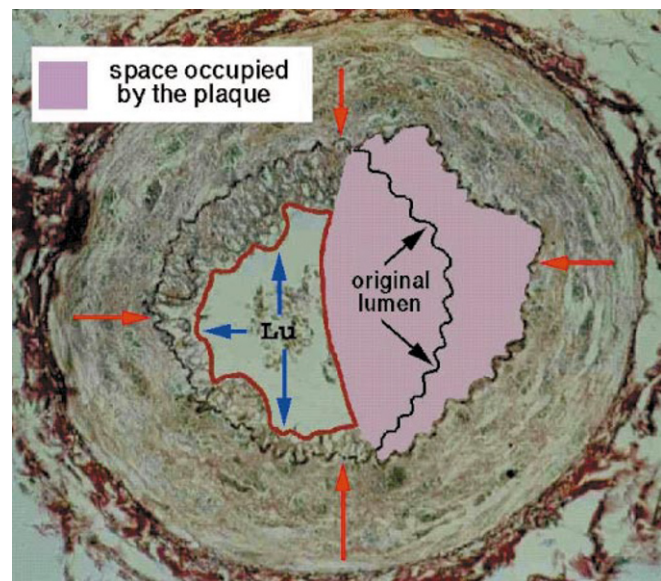


**Fig. 5.** Area occupied by the plaque is surrounded by internal elastic lamina. Potential lumen area is defined as area encompassed by internal elastic lamina (red arrows)

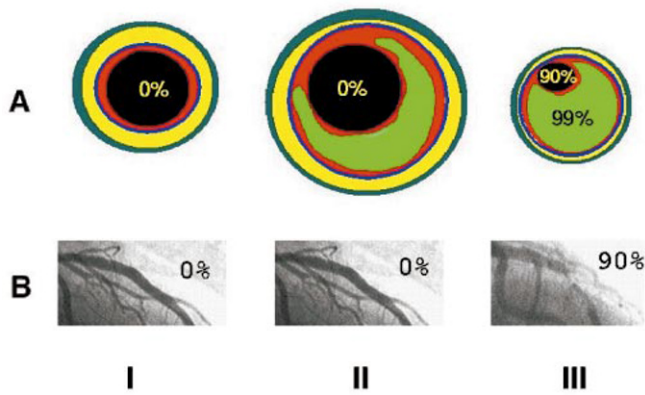


**Fig. 6.** **A:** area stenosis. **B:** diameter stenosis. In column I, a normal artery is shown. The angiographer and the pathologist see the same artery. In column II, the artery shows a 50% stenosis. Because of the Glagov phenomenon, the angiographer sees a normal lumen, but the pathologist sees 50% of the cross-sectional area occupied by the plaque. In column III, the artery shows a 95% stenosis. Now the angiographer sees a lumen that is 90% less in diameter than the normal artery near it. The pathologist sees a larger plaque that occupies 95% of the arterial cross-sectional area

### 2.5 Disease development

Atherosclerosis is a focal chronic inflammatory fibroproliferative disease of the arterial intima caused by the retention of modified low-density lipoprotein and by hemodynamic stress (see [46]). This disease is the main cause of death in Western countries, with a tremendous medical, social and economic impact. It is a progressive disorder that causes a gradual and uneven narrowing of medium- and large-sized arteries through the development of fibrous or fatty plaques within the arterial walls (see [95]). Vascular sequelae are due either to obstruction of blood flow or to dilation of localized segments of the arterial system. Indeed, morbidity and mortality usually result from localized plaque deposition rather than diffuse diseases (see [126]). The genesis and the evolution of atherosclerotic disease involves many processes such as the infiltration of leukocytes into the vessel wall, alterations in lipid metabolism, cell migration through the extracellular matrix and eventually thrombosis caused by platelet aggregation at the site of stenosis (Fig. 7). However, the fundamental event causing the plaque to develop is the enlargement of the intima by the infiltration and accumulation of lipoproteins and the associated cellular and synthetic reactions (see [95]).

The localized deposition in susceptible zones of the arterial tree is relatively constant and predictable. It is now accepted that hemodynamic forces are localizing factors in atherogenesis (see [98, 99]).

At the carotid bifurcation, the flow divider is usually spared from lipid deposition in 85% of patients examined in the literature (see [126]). In the neighborhood of this site the flow is laminar, unidirectional, featuring high levels of wall shear stress. The carotid sinus opposite the flow divider, a preferential site of lipid deposition, is characterized by oscillatory levels of wall shear stress, flow-reversal zones and increased particle residence time (up to 2–3 seconds) (Fig. 8 – see [27, 51, 57, 100, 127]).

In these zones of the arterial tree the hemodynamic environment may allow a longer cell-to-cell interaction at the

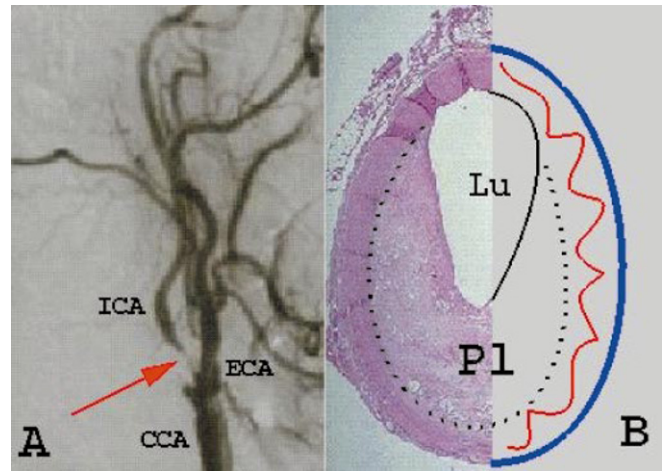


**Fig. 7.** In **A**, the angiogram shows a critical stenosis of the internal carotid artery (red arrow), localized in the outer wall of the carotid sinus, opposite the flow divider (CCA = common carotid artery; ICA = internal carotid artery; ECA = external carotid artery). In **B**, the carotid artery shown here has narrowing of the lumen due to build up of atherosclerotic plaque. This microscopic cross section of the carotid shows a large overlying atheroma (Pl). Cholesterol clefts are numerous in this atheroma. Severe narrowing can lead to angina, ischemia, and infarction. Atheromatous emboli from this lesion are rare (or at least, complications of them are rare)

endothelium-blood interface. It has also been guessed that a failure of the endothelium clearance mechanisms could occur where flow patterns are changed (see [127]).

It has been confirmed by clinical observations that atherosclerotic lesions develop in areas of disturbed flow patterns, particularly at branches and bifurcations. These types of flow also influence the infiltration of monocytes during the development of vascular lesions (see [13]).

Whether a stable fatty-streak develops depends largely on mechanical forces acting on specific parts of the arterial wall. Early atherosclerotic lesions are usually located in predictable sites of focal adaptive intimal thickening (e.g. the carotid sinus).

The prediction of the localization of advanced atherosclerotic lesions is very difficult and sometimes plaques can occur

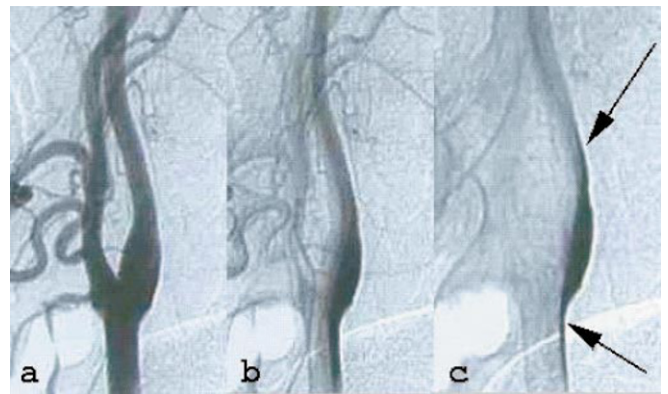


**Fig. 8a–c.** The angiogram shows the carotid flow pattern during three different steps of the cardiac cycle. **a** systole; **b** deceleration phase; **c** diastole. It is very interesting to note the behavior of the contrast medium in the outer part of the carotid sinus during diastole. At this level, the contrast medium shows an increased residency time with a longer blood-endothelium interaction

in parts of the vessel geometry not apparently involved in altered flow patterns. This can be due to the fact that intimal and medial thickenings and wall remodeling associated with different responses of the artery to injury may induce asymmetric vascular narrowings that affect the lumen configuration. This situation modifies flow patterns and the distribution of tensile and shear forces in the arterial wall, altering the “physiological” deposition of the plaque (see [12, 24, 127]).

### 3 Mathematical modelling of blood flow

The complexity of the cardiovascular system features a tremendous variety of districts like large arteries, vases of medium caliber as well as capillaries. Their size ranges from few centimeters in diameter down to few micrometers (see Table 1). Except for the very tiny capillaries, the blood flow can be assumed to behave as a continuum (see e.g. [17, 101]), as well as incompressible, apart from severe pathological situations. As such, its macroscopical behavior can be described by its velocity and pressure fields, related by the momentum and mass conservation laws, which we are going to illustrate.

We adopt the following notation:  $\Omega$  is a three-dimensional region denoting the portion of the district on which we focus our attention, and  $\mathbf{x} = (x_1, x_2, x_3)$  is an arbitrary point of  $\Omega$ ;  $\mathbf{v} = \mathbf{v}(\mathbf{x}, t)$  denotes the blood velocity. For  $\mathbf{x} \in \Omega$  and  $t > 0$ , the conservation of momentum and mass is described by the following equations:

$$\begin{cases} \rho \frac{D\mathbf{v}}{Dt} - \nabla \cdot \mathbf{T} = \rho \mathbf{f} & \mathbf{x} \in \Omega, t > 0 \\ \nabla \cdot \mathbf{v} = 0 & \mathbf{x} \in \Omega, t > 0 \end{cases} \quad (1)$$

where  $\rho$  is the density of the fluid and  $\mathbf{f} = \mathbf{f}(\mathbf{x}, t)$  is a possible volume source term which is prescribed for all  $\mathbf{x} \in \Omega$  and  $t > 0$ . Actually, the blood density  $\rho$  depends on the red-cell concentration  $c$ . However, in physiological conditions, the value of  $\rho$  is almost constant. Therefore, for the sake of simplicity, in the remainder of this paper,  $\rho$  will be considered constant. We remark that in the momentum equation (1)<sub>1</sub>, the symbol:

$$\frac{D\mathbf{v}}{Dt} = \frac{\partial \mathbf{v}}{\partial t} + \mathbf{v} \cdot \nabla \mathbf{v} \quad (2)$$

denotes the *total (or material) derivative* of  $\mathbf{v}$  with respect to  $t$ , while  $\mathbf{T}$  is the stress tensor of the fluid.

In this section, we investigate the specific features and the limits of system (1) as a mathematical model of blood. First of all, we consider the features of the blood as a fluid. Particularly, we consider the functional dependence of  $\mathbf{T}$  on  $\mathbf{v}$  and the blood pressure  $P = P(\mathbf{x}, t)$ , which is the field of *blood rheology* (Sect. 3.1).

Then, we analyze some relevant properties of blood flow in specific districts such as arteries. A peculiar feature is the flow unsteadiness, or, more precisely, the *pulsatility* induced by the periodic contractive and relaxing motion of the heart. Another feature is the absence of turbulence in almost every vascular district. These issues will be discussed in Sect. 3.2

In view of the numerical solution of equations (1) in a *specific* vascular district, a suitable set of conditions has to be prescribed at the initial time  $t_0$  and at the domain boundary  $\Gamma$ .

This issue is far from being trivial, especially as far as the boundary conditions are concerned, since the assigned data have to be mathematically correct, and, on the other hand, they have to correspond to quantities actually measurable. We will face this problem in Sect. 3.3.

Finally, since the vessel geometry strongly influences the local flow patterns and henceforth the presence, localization and development of intimal thickening and plaques, as illustrated in the previous section, an accurate geometrical reconstruction of the vascular district at hand is essential for this kind of problem. Different analytical solutions are available for some simplified geometries which can be provided for the system (1) correspondingly to different set of boundary conditions (see e.g. [73]). Nonetheless, in order to set up a tool for clinical purposes, it is worthwhile reconstructing the individual vascular morphologies from medical imaging data and then simulating the blood flow in such geometries. This issue will be introduced briefly in Sect. 3.4 and will be substantiated by the numerical results given in Sect. 6.

#### 3.1 Blood rheology

In order to provide a brief acquaintance with the complex field of blood rheology, let us recall some basic notions from fluid mechanics. We denote by  $\mathbf{T}$  the *stress tensor* of the fluid and by  $\mathbf{d}$  the strain rate tensor, defined as follows:

$$\mathbf{d} = \frac{1}{2} (\nabla \mathbf{v} + \nabla \mathbf{v}^T),$$

which is obviously symmetric. Assessing the dependence law of  $\mathbf{T}$  from  $\mathbf{d}$  is the field of *rheology*. This relation is called the *constitutive law* and, in many cases, it can be expressed by an equation in the following form:

$$\mathbf{T} = -P\mathbf{I} + \mathbf{S}, \quad (3)$$

where  $\mathbf{I}$  is the Kronecker tensor (identified by an identity matrix). In this case, tensor  $P\mathbf{I}$  is called the *isotropic tensor*,  $P$  is the *pressure* of the fluid, while  $\mathbf{S}$  is the so-called *extra-stress tensor*.

If  $\mathbf{S}$  is a linear function of the rate-of-strain tensor, i.e.

$$\mathbf{S} = 2\mu \mathbf{d} = \mu (\nabla \mathbf{v} + \nabla \mathbf{v}^T), \quad (4)$$

the fluid is called *Newtonian*. The constant  $\mu$  represents the (*dynamic*) *viscosity* of the fluid. The Newtonian law (4) is the simplest one which can be encountered in the study of viscous flows. Other relations between the stress tensor and the rate-of-strain tensor are actually observed in the experiments, identified under the general definition of *non-Newtonian fluids*. Strictly speaking, blood is not Newtonian, due to its complex nature. Therefore, in order to investigate the specific blood rheology adequately, we will give some introductory notions about non-Newtonian fluids. More complete reviews of these topics can be found e.g. in [92, 120] and [125].

For the sake of simplicity, let us start considering the case of a fluid confined between two plates, as illustrated in Fig. 9. The lower plate is fixed, while the upper one moves with a constant velocity  $V\mathbf{e}_{x_1}$  ( $\mathbf{e}_{x_1}$  being the unit vector along the  $x_1$ -axis). The velocity field is therefore given by:  $\mathbf{v} = V\mathbf{e}_{x_1}$ , where  $V$  is a linear function of  $x_2$ .

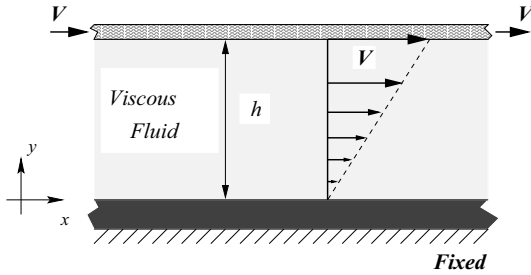


Fig. 9. Fluid confined between two plates (see [120])

In this configuration, the only non-zero component in  $\mathbf{d}$  is obviously  $d_{12}(=d_{21})$ , whereas the one of  $\mathbf{T}$  is  $T_{12}$  (the mixed component of shear stress).

Let us consider some of the relationships between  $d_{12}$  and  $T_{12}$  which could be experimentally observed, different from the linear dependence (identified by the number 1, in Fig. 10) of the Newtonian case.

*Dilatant or shear thickening fluids*: the strain rate-stress curve is convex, i.e. the ratio between shear stress and strain rate (*apparent viscosity*) increases when the strain rate increases. In the case of a fluid confined between two plates, we could, for example, describe this situation by the simple equation  $T_{12} = k(d_{12})^n$  with  $k$  constant and  $n > 1$ . This is equivalent to assuming that the apparent viscosity  $\mu = T_{12}/d_{12}$  has the following functional dependence on the strain rate:

$$\mu = k(d_{12})^{n-1} \quad \text{with } n > 1. \quad (5)$$

In more general cases, this equation still holds, substituting an invariant of the stress tensor for the component  $d_{ij}$  (see below).

*Pseudoplastic or shear thinning fluids*: the strain rate-stress curve is concave, the apparent viscosity decreases when the strain rate increases. The counterpart of equation (5) is:

$$\mu = c(d_{12})^{n-1} \quad \text{with } n < 1. \quad (6)$$

*Bingham plastic fluids*: the relationship between stress and strain rate is still linear; however, there is a threshold value of the stress (*yield stress*) beyond which there is deformation.

*Plastic*: the thinning effects are very strong.

In some cases, the rheological properties of the fluid could depend on the time-history of its stress. In simple cases, we

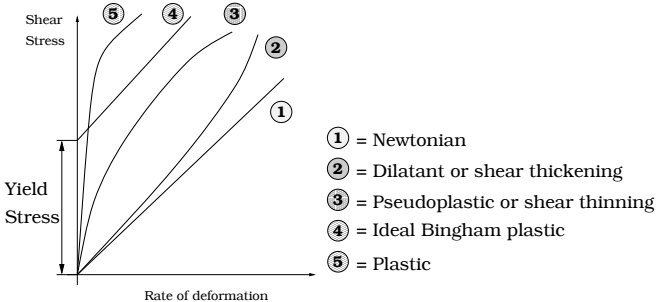


Fig. 10. Representation of different kinds of non-Newtonian time-independent fluids. Shear stress vs. Rate-of-strain diagram (see [120])

have an apparent viscosity depending on time; in particular, we could have (see Fig. 11):

*Rheopectic fluids*, with apparent viscosity increasing in time (at constant strain rate);

*Thixotropic fluids*, with apparent viscosity decreasing in time (at constant strain rate).

In general, whenever  $\mathbf{S}$  is a tensor-valued function in the form:

$$\mathbf{S} = \mathbf{f} \left( \mathbf{d}, \frac{D\mathbf{d}}{Dt}, \frac{D^2\mathbf{d}}{Dt^2}, \dots, \frac{D^k\mathbf{d}}{Dt^k} \right)$$

the fluid is said to be of *differential type* (with grade  $k$ ). The constitutive laws considered so far belong to this class. However, in more complex cases, these models could be unsuitable (see e.g. [92]). This is the case of fluids exhibiting a *viscoelastic behavior*. In particular, when a constant stress is imposed on a continuum (solid or fluid), induced deformations can increase in time (*creep*). In some cases, such deformation does not vanish even when the stress is suddenly switched to zero. Conversely, when a constant strain is imposed on a fluid, it could happen that the stress needed to maintain the constant strain will decrease continuously in time (*stress relaxation*). In all these cases, the suitable constitutive laws relating  $\mathbf{S}$  and  $\mathbf{d}$  are in the form:

$$\frac{D^j\mathbf{S}}{Dt^j} = \mathbf{f} \left( \mathbf{S}, \frac{D\mathbf{S}}{Dt}, \dots, \frac{D^{j-1}\mathbf{S}}{Dt^{j-1}}; \mathbf{d}, \frac{D\mathbf{d}}{Dt}, \dots, \frac{D^k\mathbf{d}}{Dt^k} \right).$$

The fluid is then called of *rate type*.

As an example, we quote the *Maxwell linear viscoelastic constitutive law*, given by the direct sum of an elastic and a viscous term. Among the nonlinear models, the *Oldroyd-B* one is defined by the constitutive law (see [92]):

$$\mathbf{S} + \lambda_1 \left[ \frac{D\mathbf{S}}{Dt} - \nabla\mathbf{v}\mathbf{S} - \mathbf{S}(\nabla\mathbf{v})^T \right] = \mu\mathbf{d} + \lambda_2 \left[ \frac{D\mathbf{d}}{Dt} - \nabla\mathbf{v}\mathbf{d} - \mathbf{d}(\nabla\mathbf{v})^T \right], \quad (7)$$

where  $\lambda_1$  and  $\lambda_2$  are characteristic constants (*viscoelastic constants*) and  $\mu$  is a constant.

For the sake of completeness, we should also mention a third kind of fluid, called of *integral type*, accounting for memory effects as well (see [125]).

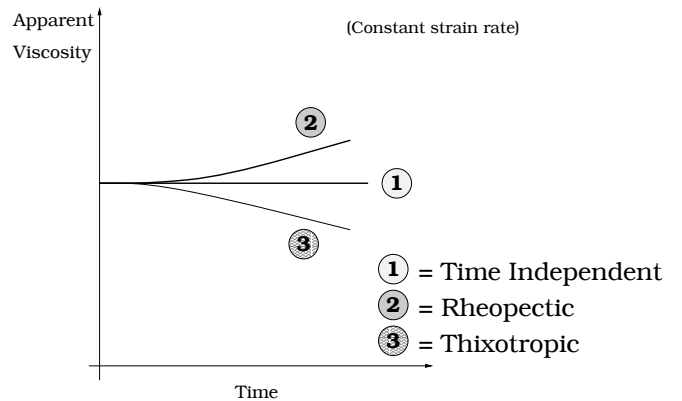


Fig. 11. Representation of some different kinds of non-Newtonian time-dependent fluids (see [120])

Blood is a suspension of different particles (*red cells*, *white cells*, *platelets*) in an aqueous solution (*plasma*). In particular, red cells influence the blood rheology to a much larger extent than white cells and platelets, due to their different concentration. Red cells are deformable, with physical and chemical features which vary in time, and are able to aggregate. Besides, in some districts red cells flow in pipes whose size is comparable with their own (*microcirculation*). Altogether, these circumstances explain the rheological features of blood, which can be summarized as follows (see, e.g., [17, 68, 125]):

- *shear thinning behavior* (see Fig. 12),
- *nonlinear viscoelastic nature*,
- *microcirculation effects*.

In particular, the shear thinning behavior can be justified by the experimentally observed formation of macroaggregates, called *roleaux*, when the strain rate is low. Roleaux formation results in an increment of apparent viscosity when the strain rate decreases. On the other hand, when the strain rate increases, roleaux break down and the role of the deformability of red cells becomes more relevant for the shear thinning behavior of blood (see [17]).

The following models have been empirically introduced in order to describe this pseudo-plastic behavior. We denote by  $c$  the red-cell concentration, by  $D_{II} = \sum_{i,j=1}^3 d_{ij}d_{ij}$  the second invariant of the strain rate tensor, and by  $\dot{\gamma} = 2\sqrt{D_{II}}$  the shear rate (in a simple shear fluid – see [83]); finally,  $k_0$ ,  $k_1$ ,  $m$  and  $\mu_0$  and  $\mu_\infty$  are functions depending on  $c$ , the temperature as well as other specific features of the fluid.

i) Casson's law (see, e.g. [83]):

$$\mu(\dot{\gamma}) = \frac{1}{\dot{\gamma}} \left( k_0 + k_1 \sqrt{\dot{\gamma}} \right)^2; \quad (8)$$

ii) Power law (see, e.g. [42, 124]):

$$\mu(\dot{\gamma}) = m |\dot{\gamma}|^{n-1}; \quad (9)$$

iii) Bird–Carreau law (or Modified–Cross law – see, e.g. [81]):

$$\mu(\dot{\gamma}) = \mu_\infty + \frac{\mu_0(c) - \mu_\infty(c)}{[1 + (\lambda\dot{\gamma})^b]^a}. \quad (10)$$

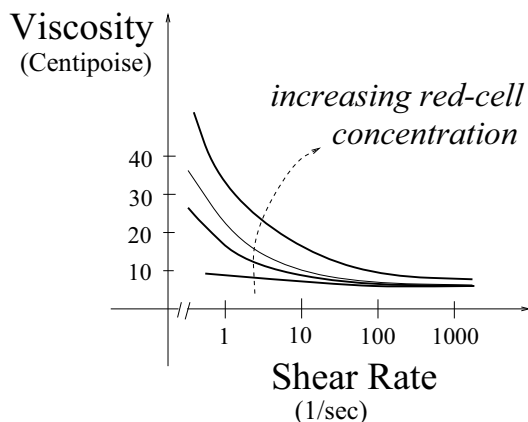


**Fig. 12.** Viscosity–Shear Rate curves corresponding to different values of red-cell concentration ([68])

Several other models describing fluids of differential type have been proposed in the literature: for an overview see e.g. [17, 125]. All these models are potentially able to describe the shear thinning behavior of blood, although for a limited range of shear rates. However, they cannot account for the viscoelasticity of blood. For this reason, blood has been investigated as a nonlinear fluid of rate type. In particular, the Oldroyd-B model (7) has recently been generalized, in order to account for both viscoelasticity and shear thinning phenomena. Roughly speaking, the model adopted in [125] is a modification of (7), where  $\mu(\mathbf{d})$  is this time a function of  $\mathbf{d}$  accounting for the shear thinning nature of blood over a wide range of shear rate values.

The rheological properties of blood, however, may depend dramatically on the vessel size. For instance, when the vessel diameter reduces to a size comparable with one of the red cells (below 12  $\mu\text{m}$ ), blood could no longer be considered a continuum. However, as the vascular bed size decreases below 500  $\mu\text{m}$ , a further reduction of apparent viscosity is observed (*Fahraeus–Lindqvist effect*) due to the physiological decreasing of red-cell concentration in capillaries.

In the framework of large and medium vessels, it is generally agreed that, under physiological conditions, the Newtonian model for blood rheology can be considered acceptable at a first level of approximation (see [68, 83, 124]). For this reason, in the sequel, we will consider blood as a Newtonian fluid, even if we are aware that a more precise accounting of the rheological properties of blood could bring a meaningful improvement to the investigation of specific clinical cases.

### 3.2 Features of blood flow in arteries

As pointed out in Sect. 1, the motion of blood in arteries is induced by the periodic contraction of the heart muscles which pump the fluid down to the arterial system from the aorta up to the capillaries. More precisely, a heart beat consists of two phases. During the first one, called *systole*, the left ventricular pressure becomes higher than the aortic one, due to an isovolumic contraction of the muscular fibers; the aortic valve opens and the blood is pumped into the aorta. In physiological cases, this phase occupies about one third of the whole beat. During the second phase, called *diastole*, the ventricular pressure is balanced by the aortic pressure, the valve closes, the ventricular pressure falls quickly, while the aortic pressure decreases slowly and the blood flows to the peripheral sites.

Therefore, one of the most evident features of blood flow in arteries is the periodic unsteadiness, or, more precisely, the *pulsatility* (see [68]). This term refers properly to the feature of a first rapid increase and decrease of the flow rate, followed by a longer phase, when the flow rate becomes small and almost constant. Figure 13, for instance, illustrates the flow rate during a heart beat at the entrance of the carotid bifurcation.

The periodic pulsatility influences in a decisive way the actual velocity profiles of blood in the arteries. A way to confirm this fact is to compare the different velocity profiles whenever steady and unsteady periodic conditions are applied to some district. Indeed, when the morphology of the fluid domain is simple, analytical solutions of equations (1) are available either for the steady and the unsteady flows. More precisely, let us consider equations (1) for a Newtonian fluid.

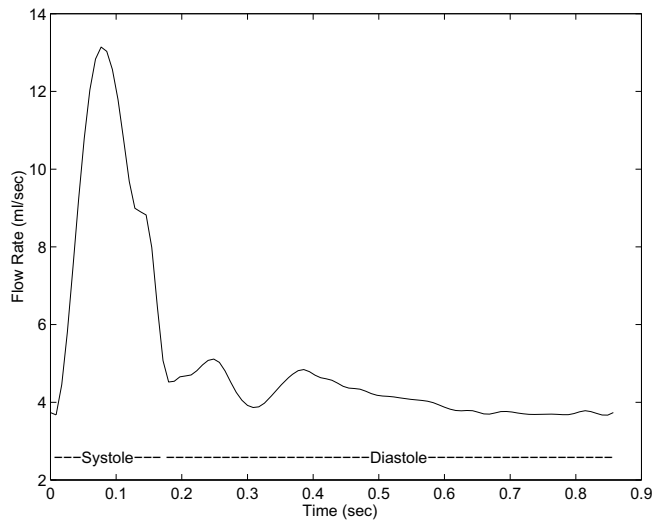


Fig. 13. Waveforms of the flow rate at the entrance of the carotid (see [82])

In this case, they read:

$$\begin{cases} \frac{\partial \mathbf{v}}{\partial t} + (\mathbf{v} \cdot \nabla) \mathbf{v} - \nu \Delta \mathbf{v} + \nabla p = \mathbf{f} \\ \nabla \cdot \mathbf{v} = 0 \end{cases}, \quad (11)$$

for  $\mathbf{x} \in \Omega$  and  $t > 0$ . In (11), we set  $p = P/\rho$  and  $\nu = \mu/\rho$  (the so-called *kinematic viscosity*). In the sequel, with a little abuse of language,  $p$  will simply be called *pressure*. Suppose, moreover, that  $\Omega$  is an infinite cylindrical pipe, and denote by  $u, v, w$  respectively the longitudinal, the radial and the circumferential components of the velocity.  $z$  is the longitudinal coordinate,  $r$  the radial and  $\theta$  the circumferential one. The walls of the pipe are supposed to be rigid and the velocity zero on them (*non-slip conditions*, see Sect. 3.3).

Let us consider two cases:

1. *Hagen–Poiseuille flow* (see e.g. [120]): if the gradient of  $p$  in (11) is a vector with radial and circumferential components zero and the longitudinal one constant and equal to  $-C$ , i.e.:

$$\frac{\partial p}{\partial z} = -C, \quad \frac{\partial p}{\partial r} = 0, \quad \frac{\partial p}{\partial \theta} = 0,$$

then the velocity profile is given by:

$$u = \frac{C}{4\nu} (r_0^2 - r^2), \quad v = 0, \quad w = 0 \quad (12)$$

(see e.g. [120]);

2. *Womersley flow*: in the case of a longitudinal pressure gradient changing periodically in time according to the law:

$$\frac{\partial p}{\partial z} = A \cos(\omega t), \quad \frac{\partial p}{\partial r} = 0, \quad \frac{\partial p}{\partial \theta} = 0, \quad (13)$$

then the velocity profile is ([121]):

$$u = \mathcal{R} \left( \frac{A}{i\omega} \left\{ 1 - \frac{J_0 \left( i^{\frac{3}{2}} \sqrt{\frac{\omega}{\nu}} r \right)}{J_0 \left( i^{\frac{3}{2}} \sqrt{\frac{\omega}{\nu}} r_0 \right)} \right\} e^{i\omega t} \right), \quad v = 0, \quad w = 0. \quad (14)$$

In (14),  $J_0$  denotes the Bessel function of order 0 with complex argument ( $i$  is the imaginary unit,  $\mathcal{R}(\cdot)$  is the real part). In this framework, the *Womersley parameter*  $\alpha$ :

$$\alpha = r_0 \sqrt{\frac{\omega}{\nu}}, \quad (15)$$

summarizes the information about the time periodic regime of the fluid and its viscosity. Obviously, it changes in the arterial system on the basis of the vessel dimension. In men (about 70 heart beats per minute),  $\alpha$  is equal to 20 in the aorta, 5 in the femoral artery, and decreases quickly in the capillaries.

Figure 14 illustrates the presence of flow-reversal zones in the Womersley 2D solution (see [116, 117]).

The Womersley flow can be considered the unsteady counterpart of the Poiseuille solution; it is indeed a *fully developed* unsteady flow in the case of a cylindrical right pipe. For blood flow, the time-dependence of the pressure gradient is not expressed by a simple sinusoidal law (see Fig. 13). Nonetheless, the Womersley solution may still be useful: indeed, since in the Womersley solution (as well as in the Poiseuille solution), the nonlinear term of equations (11) actually vanishes, the problem at hand is linear. Therefore, it is possible to extract the different frequency components of the flow-rate waveform on the inflow boundary and correspondingly sum up the contribution at each frequency of the Womersley profiles associated (see [48, 111, 114]).

Another feature of blood flow in arteries is the presence in some specific districts and in some instants of the beat of turbulence phenomena, i.e. of irregular eddying motion, in which random, even chaotic, perturbations in time and space of the velocity and pressure fields occur about their mean values; the components of perturbation extend over a continuous hierarchy of scales or frequencies so that they must be characterized by statistical means (see [68]). In particular, the

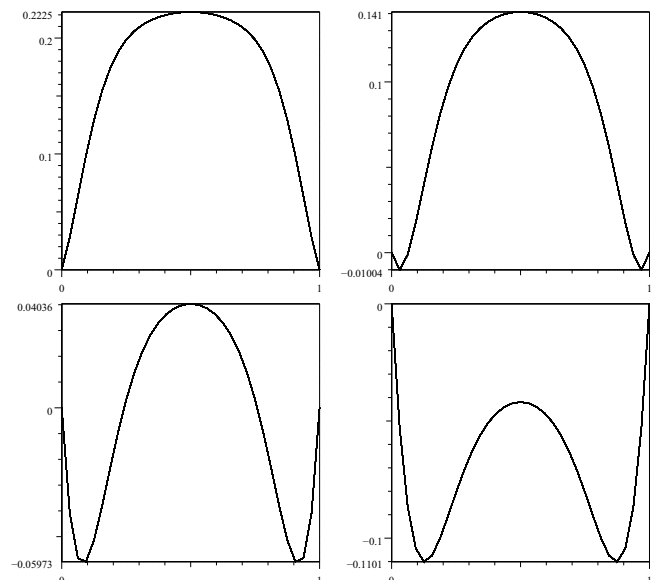


Fig. 14. Velocity 2D profiles of Womersley unsteady flow at different instants (see [116]). Along the  $x$ -axis the transversal (in 3D radial) coordinate is shown, on the  $y$ -axis the velocity. Observe the flow-reversal (i.e. negative velocity) zones in the second, third and fourth pictures

experimental evidence, at least in the human vascular system, shows the presence of disturbances in the ascending aorta (in the immediate neighbourhood of the aortic valve) and in the pulmonary artery; the phenomena are limited in the final part of the systolic phase, after the systolic peak (see [68]). For a discussion about the reasons for and the consequences of these phenomena, see for instance [73]. However, apart from the exceptions pointed out, blood flow can be assumed to be *laminar*. Indeed, in physiological conditions, the values of speed involved are low enough (see [68]). Moreover, generally, the periodicity of the flow, accompanied by the shortness of vascular districts, does not give rise to fully developed turbulence. The disturbances, whenever present, are typically very spotty and localized, both in time and space and they do not have the statistical properties that are featured by turbulent flows.

On the basis of the arguments developed so far, we will hereafter assume equations (11) for an incompressible Newtonian laminar fluid as an acceptable model to describe the blood flow in a specific arterial district.

*Remark 1.* An important indicator of the flow behaviour is the so-called *Reynolds number*,  $Re = \rho \frac{LU}{\mu} = \frac{LU}{\nu}$ , where  $U$  is a characteristic velocity of the problem at hand,  $L$  a length scale (i.e. a linear dimension of the computational domain  $\Omega$ ). In large and medium human vessels, the Reynolds number corresponding to the systolic peak ranges from 400 (common iliac arteries) up to 10 000 (proximal ascending aorta – see [68]).

### 3.3 Boundary treatment

In order to compute (analytically or numerically) the velocity and pressure fields of blood in a district  $\Omega$ , equations (11) must be provided with initial conditions  $\mathbf{v} = \mathbf{v}_0$  at time  $t_0$  and suitable boundary conditions. The initial condition must essentially specify the velocity field at a given (arbitrary) starting time  $t_0$ ; in the sequel, such an initial velocity field will be denoted by  $\mathbf{v}_0$ . For the latter, on the one hand the prescribed data should correspond to physical data which are actually measurable in practice. On the other hand, typical measures for boundary data do not provide enough information to make the associated mathematical problems well posed. Therefore, it is necessary to assess a specific treatment to supply the unavailable data with the further boundary conditions needed to obtain the well-posedness.

To begin with, let us consider a typical domain which can be encountered in blood-flow problems, as illustrated in Fig. 15.

Three parts can essentially be distinguished on the boundary  $\Gamma$  of  $\Omega$ . The first one,  $\Gamma_w$ , is the wall of the vessel. If it is supposed to be rigid, we impose homogeneous Dirichlet boundary conditions,  $\mathbf{v} = \mathbf{0}$  for all  $\mathbf{x} \in \Gamma_w$ . Otherwise, when the compliance of the vascular tissue is accounted for, we will prescribe the continuity of the velocity field (see Sect. 4). In this section, we consider a rigid-wall problem.

Then, we identify two parts of  $\Gamma$ ,  $\Gamma_{up}$  and  $\Gamma_{dw}$ , which can be composed of one or more simply connected sections (in Fig. 15, there are three sections  $\Gamma_{dw}$  and one section  $\Gamma_{up}$ ). We

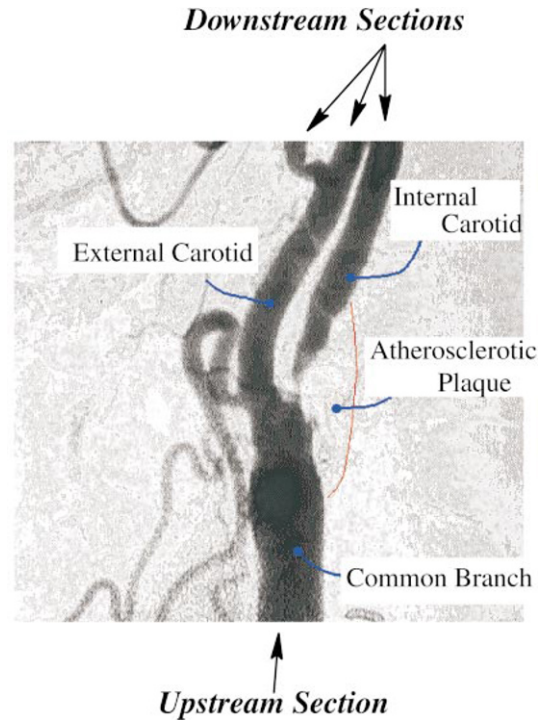


**Fig. 15.** An example of a vascular district of a typical bifurcation (e.g. carotid) with an upstream section and three downstream sections

will denote by  $\Gamma_{up}$  the *upstream* or *proximal* boundary. Then

$$\int_0^T \int_{\Gamma_{up}} \mathbf{v} \cdot \mathbf{n} \, d\omega dt < 0, \quad (16)$$

$T$  being the heartbeat duration and  $\mathbf{n}$  the normal outward unit vector. Generally speaking, due to the presence of recirculation zones, it is not possible to suppose that  $\mathbf{v} \cdot \mathbf{n} < 0$  across a whole upstream section and for all  $t \in (0, T]$ . Similarly, the *downstream* or *distal* section is the one that satisfies the relation:

$$\int_0^T \int_{\Gamma_{dw}} \mathbf{v} \cdot \mathbf{n} \, d\omega dt > 0. \quad (17)$$

Again, since in principle it is not true that  $\mathbf{v} \cdot \mathbf{n} > 0$ , for all  $\mathbf{x} \in \Gamma_{dw}$  and for all  $t \in (0, T]$ , strictly speaking  $\Gamma_{dw}$  is not an outflow boundary. Remark that both  $\Gamma_{up}$  and  $\Gamma_{dw}$  do not correspond to real boundaries, as they are introduced with the purpose of bounding the district at hand. Boundary conditions that are mathematically admissible for artificial sections have been extensively investigated (see [35, 45, 76], Sect. 10.1 in [90] and references therein). A choice often adopted in numerical computations consists of using the following set of equations:

$$\begin{cases} \mathbf{v} = \mathbf{g} & \text{on } \Gamma_{up} \\ -p\mathbf{n} + \nu \nabla \mathbf{v} \cdot \mathbf{n} = d\mathbf{n} & \text{on } \Gamma_{dw}, \end{cases} \quad (18)$$

for all  $t > 0$ , where  $\mathbf{g}$  is an assigned velocity profile. The downstream conditions in (18) amount to prescribing the

normal component of the stress tensor  $\mathbf{T} \cdot \mathbf{n}$  (Neumann conditions).

Conditions (18) provide a mathematically complete set of boundary data, in the sense that, prescribing three scalar conditions in a 3D problem (or two conditions in a 2D problem) at every point of the boundary, the associated differential problem can be well posed. It is possible to prove (see [45, 117]) that the solution of the problem (1) with the boundary conditions (18) and the initial condition  $\mathbf{v} = \mathbf{v}_0$  for  $t = 0$  (in two or three dimensions) exists for all  $t \geq 0$  provided that the forcing term  $\mathbf{f}$  and the boundary datum  $\mathbf{g}$  are smooth enough and  $\nabla \mathbf{v}_0$  is sufficiently small with respect to  $\mathbf{v}$ . Moreover, if these quantities are sufficiently small, the solution is unique. Actually, the smallness of data is not a mandatory restriction for a 2D problem, provided that the downstream sections correspond exactly to the pointwise outflow sections (i.e.  $\mathbf{v} \cdot \mathbf{n} > 0$  on every point of the downstream sections – see [117]). Unfortunately, as we have already pointed out, the presence of flow reversal zones in the vascular system makes this hypothesis seldom applicable in hemodynamics. Moreover, from the practical viewpoint, the prescription of pointwise conditions can be troublesome. Indeed, measures of the velocity field on the whole upstream section are seldom available. For this reason, different strategies have been adopted.

A possibility consists of approximating the unavailable velocity inlet field  $\mathbf{g}$  with a Poiseuille profile (12) in steady problems or a Womersley profile (14) in unsteady cases, assuming that the upstream vascular morphology could be approximately considered as being cylindrical (see e.g. [48, 82, 114]). This is a reasonable approximation in order to fill in the gaps in information at the inlet, even if the complex vascular morphology seldom exhibits a cylindrical geometry, which allows for a fully developed flow (as Poiseuille and Womersley profiles are).

As far as the downstream conditions are concerned, a value of  $d$  can be assigned on the basis of a priori considerations about the flow structure, as for the Dirichlet conditions (typically  $d = 0$ ). In any case, failing to fix the right value for a Neumann condition is by far less critical than for Dirichlet's. In principle, other boundary conditions than (18) can be considered if measurements are available. In this respect, on the upstream/downstream sections, it is possible, for instance, to measure the blood flux; this means that on every section we prescribe the condition:

$$\int_{\Gamma_i} \mathbf{v} \cdot \mathbf{n} d\gamma = F_i(t) \quad (19)$$

$i = 1, \dots, n$ , where  $n$  denotes the number of upstream/downstream sections. Indeed, different techniques can be set up in order to measure  $F_i(t)$  (for an overview, see e.g. [50] and [68], Chap. 6). Among others, one of the most common is based on the measurement at different sites of the concentration of a tracer material injected into the vasculature. If the injected concentration is known, it is possible to deduce the flow rate from the concentration measured downstream. Other methods are based on Ultrasound Techniques (whose performances can be in turn supported by numerical computations – see [72]).

On the other hand, when dealing with a particular vascular district, it should be considered that it is a part of a global,

complex system, including the arterial and venous networks. This system is closed, i.e. it features a *feedback mechanism* such that the downstream state can influence the upstream one. For instance, a stenosis at the level of a carotid bifurcation could influence the blood distribution in the whole vessel system leading to the head. Mathematical descriptions of the whole system, accounting for these mechanisms, are usually based on electrical/hydraulic network analogies (see e.g. [18, 43, 93, 119]), which associate the voltage drop with the pressure drop and the current with the flow rate. Nevertheless, these “lumped” models are not able to provide an accurate description of the hemodynamics in local districts, in particular with respect to the pathogenesis, since they are only able to predict mean values across vascular sections. A strategy for local hemodynamics also accounting for the feedback mechanisms consists of coupling lumped parameter models (based on ordinary differential equations) with distributed parameter models (using partial differential equations), as illustrated in Fig. 16. A delicate point is the exchange mechanism between the two subsystems. A possible strategy consists of prescribing the mean pressure drop computed by the lumped model as a boundary condition for the partial differential equations of the local distributed model and, on the other hand, providing the flow rate computed by the Navier–Stokes equations to the network.

Therefore, a boundary problem arising from these coupling models could be the one prescribing the mean values of the pressure on the upstream/downstream sections, that means that the condition:

$$\frac{1}{|S_i|} \int_{\Gamma_i} p d\gamma = \bar{p}_i(t) \quad (20)$$

is prescribed on every connected upstream/downstream boundary  $\Gamma_i$ ;  $\bar{p}_i$  is indeed computed by the lumped model (mean value) and  $|S_i|$  is the area of the section.

Both the above conditions (19) and (20) prescribe “mean” quantities on the upstream and downstream sections. Unfortunately, from the mathematical viewpoint, they are not enough to ensure the well-posedness of the associated boundary value problem. Therefore, we must introduce further conditions, which do not correspond to physical data. Henceforth, they will very likely perturb the real problem. It is thus interesting

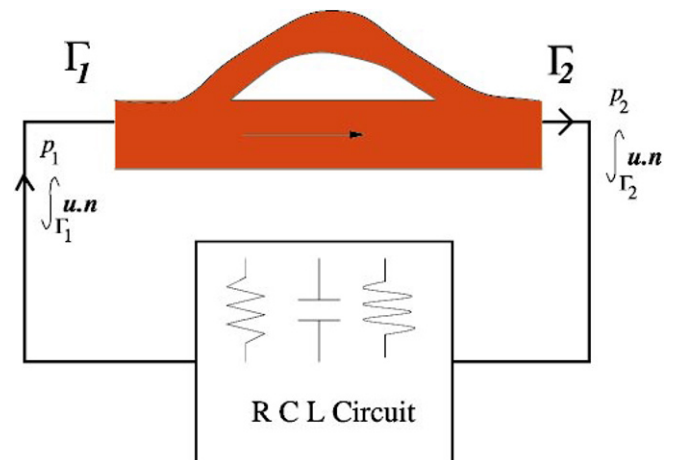


Fig. 16. Coupling of lumped and distributed models

to use those conditions that are able to keep such perturbations low. To this end, a mathematical device is the one based on the so-called *do-nothing principle*, investigated in [45]. The basic idea is to translate the original problems into a *weak* or *variational formulation*, which turns out to be the right formulation for carrying out the mathematical analysis of the problem (see e.g. [54, 113]) and provides the ground for the design of the numerical approximation of these equations based on Galerkin methods such as Finite Element or Spectral methods (see Sect. 5 and e.g. [33, 90]). In this way, the choice of the lacking boundary conditions is reduced to the choice of a suitable variational form. Indeed, the natural boundary conditions associated with the selected form will turn out to be the boundary conditions needed to make the problem well posed. Since the natural (Neumann) boundary conditions are better conditioned than essential ones (Dirichlet), this choice ensures good performances in terms of low perturbations introduced (see [45]).

As an example, let us investigate the case of the mean pressure conditions (20) (considered in [4, 45] and, in the case of vascular problems, in [117], Chap. 3 and [116], together with (19) and other conditions based on the prescription of “mean” values). For the sake of simplicity, suppose that the Dirichlet boundary data prescribed on  $\Gamma_D$  are zero. Let us denote, as usual, the functional space  $L^2(\Omega)$  of the functions with integrable square in  $\Omega$ , and  $H^1(\Omega)$  the subspace of  $L^2(\Omega)$  functions whose first derivative belongs to  $L^2(\Omega)$  too. The corresponding spaces for vector functions will be denoted in bold face. In particular,  $\mathbf{H}_{\Gamma_D}^1(\Omega)$  denotes the subspace of  $\mathbf{H}^1(\Omega)$  of functions vanishing (in the sense of traces) on  $\Gamma_D$ . Then, the variational formulation of the Navier–Stokes problem reads as follows: for all  $t > 0$  find  $\mathbf{v}(t, \mathbf{x}) \in \mathbf{H}_{\Gamma_D}^1(\Omega)$  such that:

$$\begin{cases} \left( \frac{\partial \mathbf{v}}{\partial t}, \boldsymbol{\varphi} \right) + a(\mathbf{v}, \boldsymbol{\varphi}) + b(\mathbf{v}, \mathbf{v}, \boldsymbol{\varphi}) \\ \quad + g(\boldsymbol{\varphi}, p) = (\mathbf{f}, \boldsymbol{\varphi}) + c(d, \boldsymbol{\varphi}) \\ g(\mathbf{v}, \boldsymbol{\psi}) = 0 \end{cases} \quad (21)$$

for all  $\boldsymbol{\varphi} \in \mathbf{H}_{\Gamma_D}^1(\Omega)$ , and  $\boldsymbol{\psi} \in L^2(\Omega)$ , with  $\mathbf{v}|_{t=0} = \mathbf{v}_0$ , where  $g(\boldsymbol{\varphi}, \boldsymbol{\psi}) = -(\nabla \cdot \boldsymbol{\varphi}, \boldsymbol{\psi})$ ,  $\mathbf{f}$  is a forcing term (e.g. gravity force). The forcing term  $\mathbf{f}$  is supposed to be smooth enough to ensure that the written relations are meaningful.

In (21)  $(\boldsymbol{\psi}, \mathbf{w}) = \int_{\Omega} \boldsymbol{\psi} \cdot \mathbf{w} d\omega$  denotes the scalar product in  $L^2(\Omega)$ ;  $a(\cdot, \cdot)$  denotes a continuous bilinear form on  $[\mathbf{H}^1(\Omega)]^2$ ,  $b(\cdot, \cdot, \cdot)$  denotes a continuous trilinear form on  $[\mathbf{H}^1(\Omega)]^3$ , treating the non-linearity of Navier–Stokes equations; finally,  $c(\cdot, \cdot)$  is a term depending on the conditions on  $\Gamma_N$  at hand. Formulation (21) is abstract, accounting for different boundary problems (as (19) and (20)) with different suitable choices of  $a(\cdot, \cdot)$ ,  $b(\cdot, \cdot, \cdot)$  and  $c(\cdot, \cdot)$ . In particular, for problem (20), take

$$\begin{aligned} a(\mathbf{v}, \boldsymbol{\varphi}) &= \nu (\nabla \mathbf{v}, \nabla \boldsymbol{\varphi}), \\ b(\mathbf{v}, \mathbf{v}, \boldsymbol{\varphi}) &= ((\mathbf{v} \cdot \nabla) \mathbf{v}, \boldsymbol{\varphi}), \\ c(\bar{p}_i, \boldsymbol{\varphi}) &= - \int_{\Gamma_i} \bar{p}_i \mathbf{n} \cdot \boldsymbol{\varphi} d\gamma. \end{aligned} \quad (22)$$

The latter is satisfied for every boundary section  $\Gamma_i$ , whose union gives  $\Gamma_N$ . It is possible to prove (see [45]) that if  $\mathbf{v}$  and

$p$  are smooth enough solutions of the Navier–Stokes equations (11) with the associated initial condition and the following conditions:

$$\mathbf{v} = \mathbf{0} \quad \text{on } \Gamma_D, \quad p \mathbf{n} - \nu \frac{\partial \mathbf{v}}{\partial \mathbf{n}} = \bar{p}_i \mathbf{n} \quad \text{on } \Gamma_i \quad (23)$$

for all  $i$  varying on upstream/downstream, then  $\mathbf{v}$  and  $p$  are also solutions of the problem specified by system (21), (22). Conversely, if  $\mathbf{v}$  and  $p$  are solutions of the system (21), with the choice (22), then  $\mathbf{v}$  and  $p$  satisfy equations (23), in the *weak* or *variational* sense (i.e. in the sense of distribution).

In particular, if we consider a cylindrical pipe with axis orthogonal to the  $\Gamma_i$  sections, it is possible to verify that choosing (22) amounts precisely to satisfying the mean pressure problem (see [45]); therefore, the “do nothing” implicit conditions actually prescribed by the variational formulation are obtained taking the second condition in (23) in the directions orthogonal to  $\mathbf{n}$ , i.e.

$$\nu \frac{\partial \mathbf{v}}{\partial \mathbf{n}} \cdot \boldsymbol{\tau}_i = \mathbf{0} \quad \text{on } \Gamma_i, \quad (24)$$

$\{\boldsymbol{\tau}_i\}$  being the set of unit vectors in the plane tangential to the boundary ( $i = 1$  in 2D,  $i = 1, 2$  in 3D).

As a benchmark case, it is shown in [45] that the Poiseuille flow in an infinite straight circular cylinder can be correctly computed by the numerical solution of a steady mean pressure problem (i.e.  $\bar{p}_i$  is constant both in space and time). Similarly, in [116] and [117] Chap. 3, it is shown that the Womersley flow in an infinite straight cylinder is also correctly computed as a mean pressure problem with a pressure drop linearly depending on the longitudinal coordinate and with a sinusoidal dependence on time. The Womersley profiles of Fig. 14 are indeed computed as numerical solutions of (21), with (22), having set  $p_{up} = 0$  and  $p_{dw} = A l \cos(\omega t)$  where  $l$  is the tube length (see (13)) and  $A$  is a constant.

In more complicated geometries, the fulfilment of the mean pressure conditions is no longer ensured by the choice (22). Nevertheless, the adoption of this choice turns out to be satisfactory in the applications as an approximate way of assigning the mean pressure (see [45]).

### 3.4 Some specific features of blood flow in real geometries

In the previous sections, we have pointed out that the vascular morphology features a relevant complexity, especially in some districts. For instance, when the aortic arch is considered, a really complicated structure has to be taken into account ([14]). Even the carotid bifurcation, which has been often modelled as a 2D planar domain (see e.g. [82, 118]), is actually a non-planar structure (see [12]). This geometrical complexity strongly influences the local features of hemodynamics and the mechanical actions of the blood flow on the wall. For these reasons, the vascular geometry plays a relevant role in the onset and development of the atherosclerotic pathologies. As an example, it is observed in [80] that the presence and the position of the recirculation zones in the carotid bifurcation is strongly influenced by the bifurcation angle (i.e. the angle between the internal and the external carotid branches at the bifurcation). Another typical case is given by the anastomosis downstream from a coronary

bypass: a different anastomosis angle induces recirculation zones that are quite different as far as importance and position are concerned (see e.g. [28]), determining the success or the failure of the bypass itself (see also Sect. 6.3 and Sect. 6.4).

All these observations make the adoption of suitable techniques for the reconstruction of geometrical individual morphologies mandatory, in order to obtain results meaningful for clinical purposes.

In this section, we will briefly consider this issue, giving just some ideas of the reconstruction starting from Computer Tomographies (CT). Specific techniques for different data-measurement devices can be considered as well (see e.g. [117], Chap. 5, for the case of Digital Subtraction Angiographies).

**3.4.1 Reconstruction of vascular geometries from Computed Tomographies.** The images given by a CT are analogous to images obtained by freezing the body, slicing it into thick sections (from 1 to 10 mm) perpendicular to its long axis, and forming an X-ray image of the slice producing a radiograph with an X-ray source perpendicular to the plane of the section. The significance of these images relies on the possibility of seeing the sections without superimposition: nothing is “hidden behind” or obscures overlying structures of a thin section. The tomographic images are clear, unambiguous 2D views into the body. A tomographic section is computed from a set of one-dimensional profiles obtained by passing an X-ray beam through the body from multiple coplanar angles of view (see [44]); the intensity of the X-rays passing through the body depends on the density of the different organs crossed. The intensity profiles obtained at different angles are suitably elaborated in order to compute the 2D slices. Then, a “stack” of an adequate number of parallel, sufficiently thin tomographic images (typically 40–80 slices separated by one mm) can make a three-dimensional reconstruction possible. This stack of images is called a *volume image*.

Let us analyze the different steps that are needed for the construction of a volume image suitable for the numerical simulation of blood-flow problems, once the 2D

slices are available. At first, the vascular domain of interest must be identified on every image (*segmentation*), then codified by a suitable set of functions and parameters (*slice interpolation*). Finally, the slices are linked to one another and specific points are identified as “nodes” for the numerical simulation (*stacking* and *meshing*), i.e. points where the velocity and pressure fields will be computed (see Sect. 6).

**Segmentation:** The CT slice image typically includes different parts or organs besides the vascular section which we are interested in. The zone of the image of some interest, and in particular the inner contour of the vascular section, has to be identified on each image (on the basis e.g. of the grey level). This step is called *segmentation*: the result of the segmentation, therefore, is a set of points on the image, or *pixels* for every slice, identifying the contour of every section.

**Slice Interpolation:** A suitable interpolation of these points (pixels) is now operated in order to have a set of equations for the domain contour. In the case of CT, where the pixels identified are in most cases a good approximation of the real vascular boundary, the curve fitting is achieved by Bezier splines (see [20] for more details). In some cases, when the original image is particularly unclear, the specialist can indicate directly some specific point for the interpolation.

**Stacking:** On the interpolating curves, it is possible to identify some significant points for the final meshing. These points can also be used for the connection of the different slices. Once the connection is obtained, we have the 3D reconstruction of the vascular district.

The connection of the slices in a 3D stack is simple in the case of a single vessel, but it can be very difficult for complex morphologies, like e.g. a carotid bifurcation. In this case, indeed, we have a modification of the topology when two downstream sections collapse in the common upstream one. Usually, the data set features a contour with a typical “8” form, which is the last one before the bifurcation, and then two

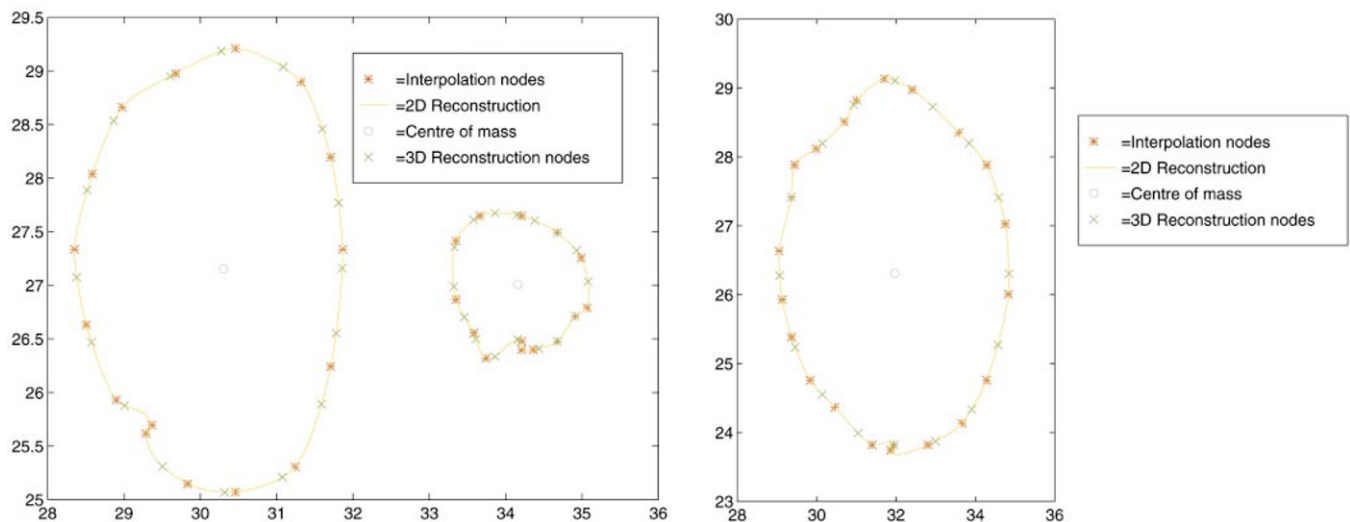


**Fig. 17.** Typical interpolant curves for sections distal (*left*) and proximal (*right*) with respect to the carotid bifurcation

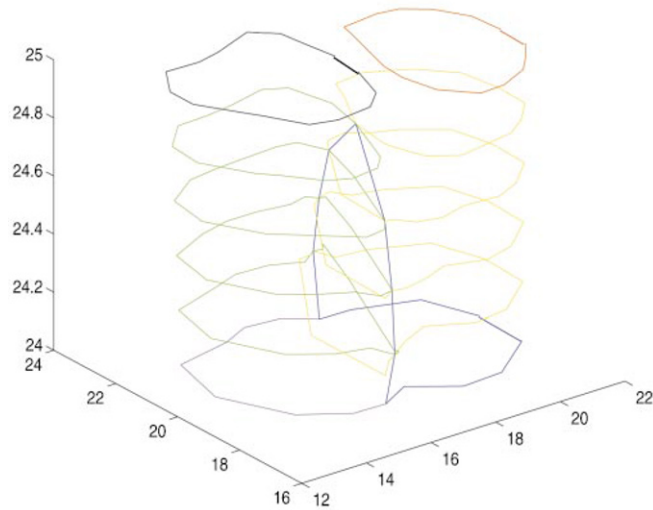


**Fig. 18.** Simplified reconstruction of the sections at the level of the carotid bifurcation

separated contours, referring to the two branches (see Fig. 18).

The treatment of such morphological difficulties can be faced according different strategies. A specific solution developed for vascular geometries can be found in [22] (see also [117], Chap. 5).

*Meshing:* On the basis of the previous steps, we have a set of contours connected by nodes, which implicitly define a set of points, or nodes (*mesh*) of the surface (apart from the upstream and downstream sections, that, however, could be meshed with a 2D grid generator). Starting from this skin-mesh, with a 3D grid-generator, we obtain the complete 3D mesh for the vascular domain suitable for a numerical simulation.

The sequence of images Figs. 19, 20, 21 aims only to give an idea of the results obtained so far.

#### 4 Mathematical models of Vessel walls and fluid-structure coupled problem

Blood and vascular tissue interact in different ways. There is a biochemical interaction: substances soluted in blood are absorbed through the endothelium layer and, in some cases, this process could lead to thickening. Biochemical interaction has been numerically considered in [75, 96], where the Navier–Stokes equations are supplemented by linear advection diffusion equations describing the concentration of soluted in blood. The boundary conditions for the latter equation model the filtration process through the walls, as a function of the shear stress induced by the blood on the vessel.

Another interaction between the blood and the fluid, which will be considered in the present section, is the mechanical one. The pulsatile character of blood flow is responsible for the strong interaction between the flow motion and the vascular wall movement. According to the Windkessel model (see [68]), during the systolic phase (blood ejection), the wall deformation accumulates part of the mechanical energy as elastic energy, which will afterwards be returned back to the fluid during the diastolic phase. Such a mechanism actually guarantees almost uniform velocity and pressure at capillary level.

The correct understanding of this interaction, besides being of primary interest for the analysis of the flow field, may help to simulate tissue-tearing phenomena or atherogenesis which eventually lead to aneurisms or stenoses. From the mathematical and numerical viewpoint, the problems arising from this mechanical interaction are very challenging due to their strongly nonlinear nature. In this section, we will investigate some issues concerned with these problems.

A global approach should describe the whole “continuum”, made of the entire vessel including the innermost (fluid) region and the outer (wall) region, as a unitary interconnected model. The complexity of this approach would generally go beyond the realistic possibility offered by present-day computer simulations. An approach aimed at this description is the *Immersed Boundary Method* developed by C. Peskin (see e.g. [78]); the Navier Stokes equations are assumed to hold

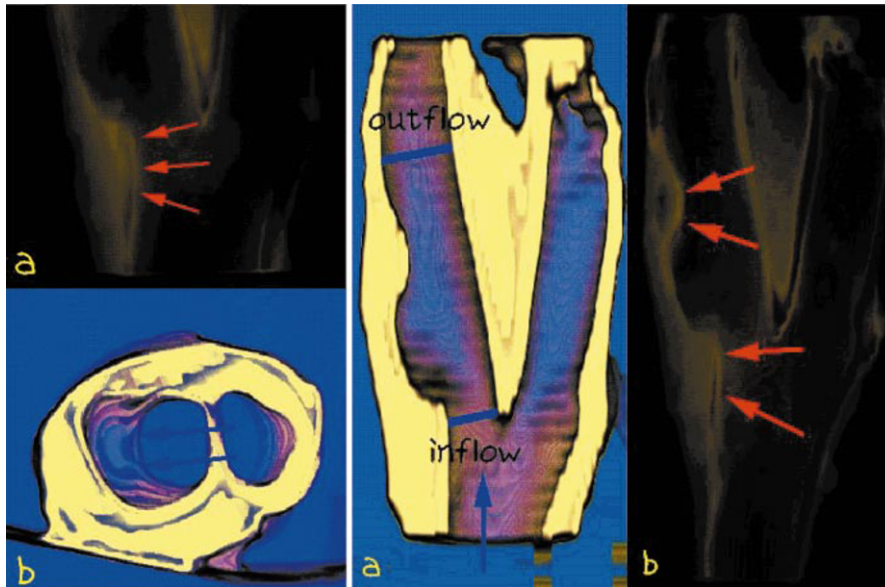


**Fig. 19.** Morphology of an internal carotid artery with 50% of stenosis

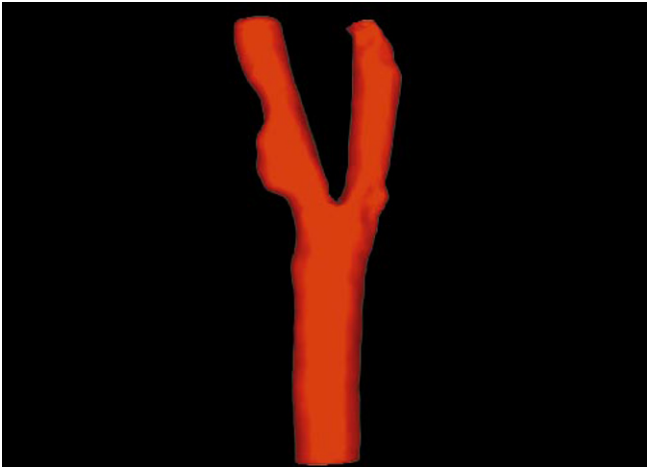


Fig. 20. 3D reconstruction of the carotid bifurcation of Fig. 19

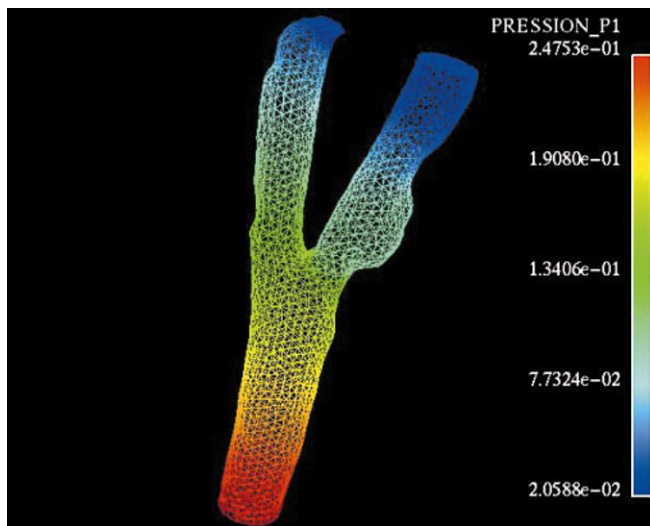


Fig. 21. Mesh of the carotid bifurcation of Fig. 19

everywhere within the heart, and describe a fluid containing an immersed system of contractile fibers.

A coupled approach is instead based on interacting two different models, one for fluids, the other for structures, through suitable matching conditions which play the role of boundary conditions for the submodels. As previously pointed out, the fluid model adopted here is based on Navier–Stokes equations, in particular (but not necessarily) for a Newtonian fluid. The model for the description of vascular-wall dynamics is presented in Sect. 4.1. This approach enables the splitting of the global computation into a sequence of separate computations for the fluid and the vascular wall, therefore yielding a considerable reduction of the computational complexity. On the other hand, maintaining physical and numerical consistency in the splitting approach may not be easy. Indeed, several issues have to be addressed in this regard, noticeably:

1. the matching conditions between fluid and structure must be physically consistent on the one hand; on the other hand, they should provide either model with boundary

conditions that are mathematically admissible for its well posedness;

2. although each sub-model, with the provided boundary condition, yields a stable problem, it is by no means guaranteed that the global problem is stable too;
3. the flow model is naturally written in Eulerian coordinates, whilst the wall model is expressed in Lagrangian coordinates. The interaction between these two heterogeneous frames demands a suitable approach, in order to set up a numerical device for the analysis of the coupled “moving boundary” problem.

In Sect. 4.2, we focus on some issues relevant to point 1 and 2. The third issue is faced in Sect. 5.2.

#### 4.1 Mechanical models of vessel walls

As pointed out in Sect. 2, the soft tissues of the vessel walls consist of different materials with different mechanical features such as collagen fibers, elastin, smooth muscle and water. Due to this complex structure, it is difficult to provide a synthetic mathematical description of the mechanical behavior of vessel walls. The investigations of the structural and biochemical properties of human soft tissues and their strict correlations, e.g. in view of the production of biocompatible tissues for vascular prosthesis, have been defined as “tissue engineering” (see e.g. [66]). Here, we limit ourselves to recalling the most relevant structural features and the simplest mathematical models for arterial tissues.

To start with, we point out that arteries are inelastic and anisotropic (cf. [11, 25]). They are *inelastic* since they exhibit different stress-strain curves in loading and unloading. A convenient approach, which falls under the name of *pseudoelasticity*, treats the two phases in a separate manner, since the actual behavior of the arterial tissue, under periodic loading and unloading, does not depend on the strain rate (see [25] and Fig. 22). When the deformations around an interesting point are really small, it is possible to linearize the problem suitably around such an equilibrium point (*incremental elasticity*). In the pseudoelastic approach, the description of the mechanical behavior of the tissues in the two (loading and unloading) phases can be described in terms of a Strain Energy Density Function (*SEDF*), that links stresses and deformations for the two different phases, via a differentiation. Namely, we have:  $\Sigma_{ij} = \frac{\partial(SEDF)}{\partial \varepsilon_{ij}}$ , where  $\Sigma_{ij}$  is the stress

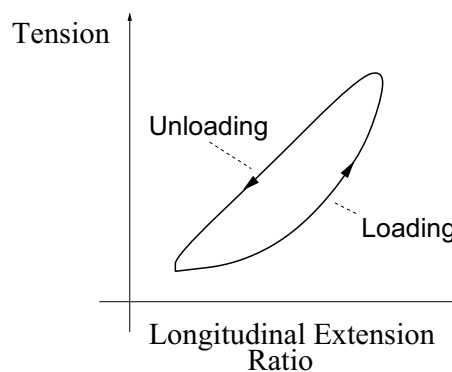


Fig. 22. Typical loading–unloading curves of carotid arteries ([25])

tensor, while  $\varepsilon_{ij}$  denotes the Green (quadratic) strain tensor (see [25]). Obviously, a quadratic *SEDF* corresponds to Hooke's law of linear elasticity. On the other hand, the form of *SEDF* that seems to be more suitable for the arteries is an exponential one (see [25]);

Arteries are *anisotropic* since the fiber structure of the tissue yields a different behavior for different loading directions. More precisely, arteries are *orthotropically cylindrical*: their behavior is described along the cylindrical components (radial, longitudinal and circumferential). Moreover, experimental evidence suggests that radial deformation is much smaller than deformations along the other directions (see [11]).

Neglecting their anisotropic behavior and the circumferential deformations, we can model vascular walls as membrane by means of the Navier equations:

$$\begin{cases} \rho_w h \frac{\partial^2 D_r}{\partial t^2} = k G h \frac{\partial^2 D_r}{\partial z^2} - \frac{E h}{1 - \zeta^2} \left( \frac{\zeta}{R_0} \frac{\partial D_z}{\partial z} + \frac{D_r}{R_0^2} \right) + \Phi_1 \\ \rho_w h \frac{\partial^2 D_z}{\partial t^2} = \frac{E h}{1 - \zeta^2} \left( \frac{\zeta}{R_0} \frac{\partial D_r}{\partial z} + \frac{\partial^2 D_z}{\partial z^2} \right) + \Phi_2 \end{cases} \quad (25)$$

The unknown variables  $D_r$  and  $D_z$  represent radial and longitudinal vessel displacement in the local frame of reference  $(r, z, \theta)$ ;  $h$  is the wall thickness;  $R_0(z)$  is the arterial reference radius at rest;  $k$  is the so called *Timoshenko shear correction factor*,  $G$  the *shear modulus*,  $E$  the Young modulus,  $\zeta$  the Poisson ratio (which is equal to 1/2 for an incompressible material);  $\rho_w$  the arterial wall volumetric mass. Finally,  $\Phi = [\Phi_1 \ \Phi_2]^T$  is the forcing term due to the external forces, including the stress induced by the fluid: indeed, they depend on the velocity  $\mathbf{v}$  and the pressure  $p$  of the blood.

Remark that this model (as well as its simplifications that we are going to introduce) is based on a *Lagrangian* description of motion of the wall motion as it is referred to a material domain  $\Gamma_w^0$ , which the spatial coordinates belong to, corresponding to the (say) "rest position"  $D_r = D_z = 0$ .

We could introduce further useful simplifications of Navier equations (25). Assuming that the effects of the forcing term  $\Phi$  due to the fluid can be reduced only to the pressure of blood, and that the longitudinal displacements and deformations are very small, the second equation in (25) can be disregarded and the first yields the simplified relationship:

$$\rho_w \frac{\partial^2 \eta}{\partial t^2} + \frac{E}{(1 - \zeta^2) R_0} \eta = \frac{\Phi}{h} \quad (26)$$

having set  $\eta = D_r$ ,  $\Phi = \Phi_1 = p_w - p_0$  (which is usually called *transmural pressure*);  $p_w$  is the pressure on the wall essentially due to the fluid, while  $p_0$  is a reference value of external pressure (at rest, when  $p_{wall} = p_0$ , we have  $\eta = 0$ , i.e.  $r = R_0$ ). If we assume a cylindrical vessel of length  $L$  at rest, then  $\eta = \eta(z, \theta, t)$ , where  $z$  and  $\theta$  are, respectively, the longitudinal and angular directions, so that  $0 \leq z \leq L$ ,  $0 \leq \theta \leq 2\pi$  (see Fig. 23).

The scalar model (26) is an ordinary differential equation of second order in time for  $\eta$ ;  $\eta$  depends on  $z$  and  $\theta$ . It is known as the *independent-rings model* (see [41, 79]) as it assumes that the vessel is made of independent-rings which are rigidly linked to one another and can only deform along the radial direction. Despite its intrinsic limitations, the extreme simplicity of model (26) makes it still very popular

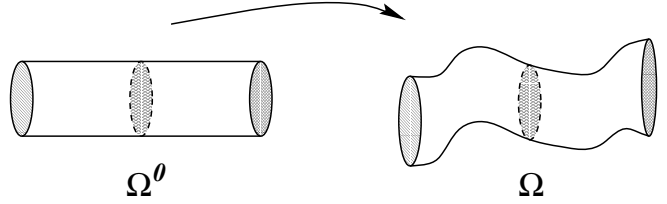


Fig. 23. Geometrical models and notations for the wall motion: 3D model

(see e.g. [41, 60, 79, 86]). More complicated models are based on shell equations, the coupling of two-dimensional domains, both for the fluid and the structure (see e.g. [56]), and axial-symmetric models ([62]).

When the coupling between a 2D fluid and a 1D structure is considered (see Fig. 24), another model of intermediate complexity between (26) and (25), which has been developed to account for longitudinal inner actions as well, is encompassed by the following initial boundary value problems:

$$\rho_w h \frac{\partial^2 \eta}{\partial t^2} = -a \frac{\partial^4 \eta}{\partial z^4} + b \frac{\partial^2 \eta}{\partial z^2} + c \frac{\partial^3 \eta}{\partial t \partial z^2} - e \eta + \Phi. \quad (27)$$

Again  $\eta(z)$  describes the "radial" displacement with respect to the rest configuration

$$\Gamma_w^0 \equiv \{(z, y) \in \mathbb{R}^2 | z \in (0, L), y \in (-R, R)\}.$$

$\Phi = \Phi_1$  is the external force (in the radial direction), while  $a, b, c, e$  are positive constants depending on the physical features of the wall tissue. More precisely, with respect to the *independent-rings model*, equation (27) takes inner longitudinal actions into account:  $a$  accounts for the inner action of bending in the tissue,  $b$  for the tension;  $c$  is a term accounting for the viscoelasticity of the tissue. Equation (27) is supposed to hold for each branch ( $\Gamma_{wall}^+$  and  $\Gamma_{wall}^-$ ) of  $\Gamma_{wall}$ , and needs therefore boundary conditions on  $\eta$  at the endpoints of  $\Gamma_{wall}^+$  and  $\Gamma_{wall}^-$ .

In the case  $a = b = c = 0$ , we recover the 2D independent-rings equation. On the other hand, in the case of zero longitudinal displacements, the equation considered in [62] reduces to (27) with  $a = 0$ . In the case  $b = c = e = 0$ , the law for the wall motion reduces to the very classical equation of the vibrating rod, and we will, therefore, call equation (27) a "generalized rod" model.

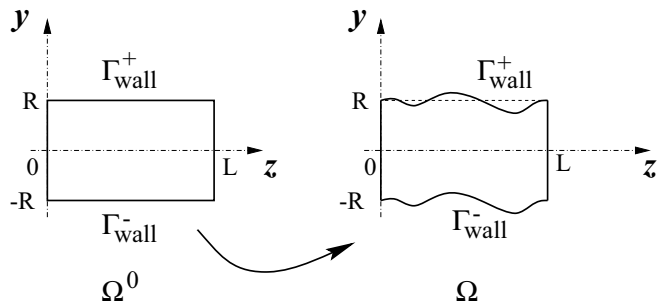


Fig. 24. Geometrical models and notations for the wall motion: 2D model

## 4.2 The coupled problem

To consider the problem arising when coupling fluid and structure models, let us restrict our analysis to a domain  $\Omega$  as the one illustrated in Fig. 24. The boundary  $\Gamma$  is composed of a portion  $\Gamma_C \equiv \Gamma_{wall}^+ \cup \Gamma_{wall}^-$ , which is assumed to be compliant, and a part  $\Gamma_F \equiv \Gamma_{up} \cup \Gamma_{dw}$ , which is assumed to be fixed. As a model for the blood flow, we adopt the Navier–Stokes equations (11). The fluid problem is therefore described by the system:

$$\text{fluid : } \begin{cases} \frac{\partial \mathbf{v}}{\partial t} + (\mathbf{v} \cdot \nabla) \mathbf{v} - \nu \Delta \mathbf{v} + \nabla p = \mathbf{f} & \mathbf{x} \in \Omega(t) \\ \nabla \cdot \mathbf{v} = 0 & \mathbf{x} \in \Omega(t) \end{cases} \quad (28)$$

together with initial condition at  $t = 0$  for  $\mathbf{v}$  and suitable boundary conditions. For the sake of simplicity, we consider the boundary conditions (18) with  $d = 0$  on  $\Gamma_F$ , while the conditions on  $\Gamma_C$  will be specified below, as matching relations between the fluid and the structure.

About the wall, let us consider the “generalized rod model” described in a Lagrangian framework by equation (27) (i.e. for  $(y, z) \in \Gamma^0 \equiv (-R, R) \times (0, L)$ ). If we denote by  $\alpha$ ,  $\beta$ ,  $\gamma$  and  $\sigma$  positive constants, depending on  $a, b, c, e, \rho_w$  and  $h$ , the structure model is therefore specified by:

$$\text{structure : } \begin{cases} \frac{\partial^2 \eta}{\partial t^2} = -\alpha \frac{\partial^4 \eta}{\partial z^4} + \beta \frac{\partial^2 \eta}{\partial z^2} + \gamma \frac{\partial^3 \eta}{\partial t \partial z^2} - \sigma \eta + \hat{\Phi} \\ z \in (0, L) \end{cases} \quad (29)$$

together with initial conditions prescribing  $\eta$  and  $\frac{\partial \eta}{\partial t}$  at the initial time  $t_0$  and boundary conditions which, for the sake of simplicity (see, however, Remark 4), are given by:

$$\eta = 0 \text{ and } \frac{\partial \eta}{\partial z} = 0 \text{ for } z = 0, L. \quad (30)$$

The forcing term  $\hat{\Phi}$  depends on the fluid and will be specified below.

Let us consider the interface conditions between the fluid and the structure. The first condition ensures the continuity of the velocity field, and reads:

$$\mathbf{v} = \frac{\partial \eta}{\partial t} \mathbf{e}_y, \quad \mathbf{x} \in \Gamma_C \quad (31)$$

The second interface condition refers to the continuity of the stresses, which in a 2D-fluid/1D-structure problem means that the forcing term on the structure is due to the stresses exerted by the fluid (and, possibly, by external terms due, for instance, to surrounding organs; we neglect these terms in our analysis). The physical stress exerted on the wall by the fluid is given by:

$$\Phi = \left( -P \mathbf{n} + \mu \frac{\partial \mathbf{v}}{\partial \mathbf{n}} \right) \cdot \mathbf{e}_y = \rho \left( -p \mathbf{n} + \nu \frac{\partial \mathbf{v}}{\partial \mathbf{n}} \right) \cdot \mathbf{e}_y \quad \text{on } \Gamma_C. \quad (32)$$

and consequently, in (29), the forcing term  $\hat{\Phi}$  is given by:

$$\hat{\Phi} = \frac{\Phi}{\rho_w h}.$$

*Remark 2.* If we do not neglect the thickness of the wall and consider the vessel as a 3D continuum in a 3D problem, the fluid stresses are a surface force and should therefore be treated as a (Neumann) boundary data for the structure problem (29). See e.g. [56] (although in a different context).  $\square$

The fluid-structure interaction problem we deal with is therefore specified by (28), (29), (31) and (32) together with (18) and (30). In view of its numerical solution, the coupled problem ought to be split at each time step into two sub-problems, one in  $\Omega$ , the other on  $\Gamma_C$ , communicating to one another through the matching conditions (31) and (32). In particular, the structure problem provides the boundary data for the fluid problem; vice-versa, the fluid problem provides the forcing term for the structure. A typical strategy for the analysis of this problem is therefore to study the two sub-problems separately and then reformulate the coupling as a global “fixed-point” problem (see e.g. [84, 85]). In this perspective, the first step consists of ensuring the well posedness of each subproblem. This aspect has to be addressed carefully, and might require a further investigation on the submodels, since, generally speaking, the smoothness of the interface data ensured by a subproblem could not be sufficient for the other one. In particular, it is possible to prove that if  $\Gamma \equiv \partial \Omega$  is smooth enough, the trace of a  $\mathbf{H}^1(\Omega)$  function on  $\Gamma$ , i.e. the restriction of the function on  $\Gamma$ , belongs to a subspace of  $L^2(\Gamma)$ , called  $H^{1/2}(\Gamma)$  (*trace Theorem*). Therefore, since the theory of Navier–Stokes equations requires that the velocity field  $\mathbf{v}$  belongs to  $\mathbf{H}^1(\Omega)$ , the boundary trace on  $\Gamma_C$ , and therefore, in particular,  $\frac{\partial \eta}{\partial t}$ , must belong to  $H^{1/2}(\Gamma_C)$ . The latter requirement is fulfilled provided that the viscoelasticity of the wall is accounted for. Indeed, if  $c > 0$ , multiplying equation (29) by  $\frac{\partial \eta}{\partial t}$ , and integrating for  $z \in (0, L)$ , we obtain:

$$\begin{aligned} & \frac{1}{2} \frac{d}{dt} \left\| \frac{\partial \eta}{\partial t} \right\|_{L^2(\Gamma^0)}^2 + \frac{\alpha}{2} \frac{d}{dt} \left\| \frac{\partial^2 \eta}{\partial z^2} \right\|_{L^2(\Gamma^0)}^2 + \frac{\beta}{2} \frac{d}{dt} \left\| \frac{\partial \eta}{\partial z} \right\|_{L^2(\Gamma^0)}^2 \\ & + \gamma \left\| \frac{\partial}{\partial z} \frac{\partial \eta}{\partial t} \right\|_{L^2(\Gamma^0)}^2 + \frac{\sigma}{2} \frac{d}{dt} \|\eta\|_{L^2(\Gamma^0)}^2 \\ & = \left( \hat{\Phi}, \frac{\partial \eta}{\partial t} \right)_{L^2(\Gamma^0)} \leq \|\hat{\Phi}\|_{L^2(\Gamma^0)}^2 + \left\| \frac{\partial \eta}{\partial t} \right\|_{L^2(\Gamma^0)}^2. \end{aligned} \quad (33)$$

By the Gronwall Lemma (see e.g. [90]), it follows that:

$$\gamma \left\| \frac{\partial}{\partial z} \frac{\partial \eta}{\partial t} \right\|_{L^2(\Gamma^0)}^2 \leq C \quad (34)$$

where  $C$  is a constant. This inequality ensures that the trace theorem is applicable and moreover  $\frac{\partial \eta}{\partial t}$  belongs to  $H^1(\Gamma^0)$ , i.e. the trace is smooth enough.

Let us now consider the stability of the coupled problem. When one deals with a Navier–Stokes problem in a time-dependent domain, the situation is complicated by the fact that time derivation and space integration are not interchangeable. Indeed, when the domain  $\Omega$  is a function of time, we have the following *Reynolds transport formula* (see e.g. [2]): for any differentiable function  $\psi$  defined in a time dependent domain  $\Omega(t)$ :

$$\frac{d}{dt} \int_{\Omega(t)} \psi d\omega = \int_{\Omega(t)} \frac{\partial \psi}{\partial t} d\omega + \int_{\Gamma(t)} \mathbf{w} \cdot \mathbf{n} \psi d\gamma. \quad (35)$$

where  $\mathbf{w}$  is the velocity of the moving boundary. In our case,  $\mathbf{w}$  is zero on  $\Gamma_F$  and is equal to  $\mathbf{v}$  on  $\Gamma_C$ . Let us multiply the first equation of (31) by  $\mathbf{v}$  and integrate in  $\Omega(t)$ . Using the Green formula, and taking into account the matching conditions, we have:

$$\begin{aligned} \frac{1}{2} \int_{\Omega(t)} \frac{\partial |\mathbf{v}|^2}{\partial t} d\omega + \nu \int_{\Omega(t)} \nabla \mathbf{v} : \nabla \mathbf{v} d\omega + \frac{1}{2} \int_{\Gamma(t)} |\mathbf{v}|^2 \mathbf{v} \cdot \mathbf{n} d\gamma = \\ \int_{\Omega(t)} \mathbf{f} \cdot \mathbf{v} d\omega - \int_{\Gamma} \left[ p \mathbf{n} \cdot \mathbf{v} - \nu \frac{\partial \mathbf{v}}{\partial \mathbf{n}} \right] \cdot \mathbf{v} d\gamma \end{aligned} \quad (36)$$

If we apply the Reynolds transport formula (35) to the first term and use the boundary conditions for  $\mathbf{v}$ , we obtain:

$$\begin{aligned} \frac{1}{2} \frac{d}{dt} \int_{\Omega(t)} |\mathbf{v}|^2 d\omega - \frac{1}{2} \int_{\Gamma_C(t)} |\mathbf{v}|^2 \mathbf{v} \cdot \mathbf{n} d\gamma + \nu \int_{\Omega(t)} \nabla \mathbf{v} : \nabla \mathbf{v} d\omega \\ + \frac{1}{2} \int_{\Gamma_C(t) \cup \Gamma_{dw}} |\mathbf{v}|^2 \mathbf{v} \cdot \mathbf{n} d\gamma = \int_{\Omega(t)} \mathbf{f} \cdot \mathbf{v} d\omega \\ - \int_{\Gamma_C} \left[ p \mathbf{n} \cdot \mathbf{v} - \nu \frac{\partial \mathbf{v}}{\partial \mathbf{n}} \right] \cdot \mathbf{v} d\gamma. \end{aligned} \quad (37)$$

which, bearing in mind (32), reduces to:

$$\begin{aligned} \frac{1}{2} \frac{d}{dt} \|\mathbf{v}\|_{L^2(\Omega)}^2 + \nu \|\mathbf{v}\|_{H^1(\Omega)}^2 + \frac{1}{2} \int_{\Gamma_{dw}} |\mathbf{v}|^2 \mathbf{v} \cdot \mathbf{n} d\gamma = (\mathbf{f}, \mathbf{v}) \\ - \int_{\Gamma_C(t)} \frac{\Phi}{\rho} \cdot \frac{\partial \eta}{\partial t} \mathbf{e}_y d\gamma. \end{aligned} \quad (38)$$

Let us introduce the parameter

$$\omega = \frac{\rho_w h}{\rho}$$

so that  $\omega \hat{\Phi} = \Phi/\rho$ . Summing equations (33) multiplied by  $\omega$  and (38) (where integration on  $\Gamma_C(t)$  is referred to  $\Gamma_C^0$ ), we are left with the equation:

$$\begin{aligned} \frac{1}{2} \frac{d}{dt} \left[ \|\mathbf{v}(t)\|_{L^2(\Omega)}^2 + \omega \left\| \frac{\partial \eta}{\partial t}(t) \right\|_{L^2(\Gamma_C^0)}^2 \right. \\ \left. + \alpha \omega \left\| \frac{\partial^2 \eta(t)}{\partial z^2} \right\|_{L^2(\Gamma_C^0)}^2 + \beta \omega \left\| \frac{\partial \eta}{\partial z}(t) \right\|_{L^2(\Gamma_C^0)}^2 + \sigma \omega \|\eta(t)\|_{L^2(\Gamma_C^0)}^2 \right] \\ + \nu \|\mathbf{v}\|_{H^1(\Omega)}^2 + \frac{1}{2} \int_{\Gamma_{dw}(t)} |\mathbf{v}|^2 \mathbf{v} \cdot \mathbf{n} d\gamma + \gamma \omega \left\| \frac{\partial}{\partial z} \frac{\partial \eta}{\partial t}(t) \right\|_{L^2(\Gamma_C^0)}^2 \\ = (\mathbf{f}, \mathbf{v}) \end{aligned} \quad (39)$$

Applying the Cauchy-Schwarz inequality to the right-hand side and integrating in the time interval  $(0, t)$ , for any  $t \in (0, T)$ , and then using to the Gronwall Lemma (see e.g. [90]),

we obtain the inequality:

$$\begin{aligned} \frac{1}{2} \|\mathbf{v}\|_{L^2(\Omega)}^2(t) + \omega \left\| \frac{\partial \eta}{\partial t} \right\|_{L^2(\Gamma_C^0)}^2(t) + \alpha \omega \left\| \frac{\partial^2 \eta}{\partial z^2} \right\|_{L^2(\Gamma_C^0)}^2(t) \\ + \beta \omega \left\| \frac{\partial \eta}{\partial z} \right\|_{L^2(\Gamma_C^0)}^2(t) + \sigma \omega \|\eta\|_{L^2(\Gamma_C^0)}^2(t) + \nu \int_0^t \|\mathbf{v}\|_{H^1(\Omega)}^2 dt \\ + \frac{1}{2} \int_0^t \int_{\Gamma_{dw}(t)} |\mathbf{v}|^2 \mathbf{v} \cdot \mathbf{n} d\gamma dt + \int_0^t \gamma \omega \left\| \frac{\partial}{\partial z} \frac{\partial \eta}{\partial t} \right\|_{L^2(\Gamma_C^0)}^2 dt \leq k \end{aligned} \quad (40)$$

$k$  being a constant depending on the forcing term and the initial data. Should the integral on  $\Gamma_{dw}$  be positive, the following a-priori estimate would be obtained:

$$\begin{aligned} \frac{1}{2} \|\mathbf{v}\|_{L^2(\Omega)}^2(t) + \omega \left\| \frac{\partial \eta}{\partial t} \right\|_{L^2(\Gamma_C^0)}^2(t) + \alpha \omega \left\| \frac{\partial^2 \eta}{\partial z^2} \right\|_{L^2(\Gamma_C^0)}^2(t) \\ + \beta \omega \left\| \frac{\partial \eta}{\partial z} \right\|_{L^2(\Gamma_C^0)}^2(t) + \sigma \omega \|\eta\|_{L^2(\Gamma_C^0)}^2(t) \\ + \nu \int_0^t \|\mathbf{v}\|_{H^1(\Omega)}^2 dt + \int_0^t \gamma \omega \left\| \frac{\partial}{\partial z} \frac{\partial \eta}{\partial t} \right\|_{L^2(\Gamma_C^0)}^2 dt \leq k. \end{aligned} \quad (41)$$

This is the case *if the downstream sections are actually out-flow sections*, i.e. the condition  $\mathbf{v} \cdot \mathbf{n} \geq 0$  is satisfied for all  $\mathbf{x} \in \Gamma_{dw}$ . Unfortunately, this is true only if the recirculation zones are far away from the downstream sections, as we already pointed out in Sect. 3.3. However, it is possible to show (see [117]) that the same stability estimate (41) could also be obtained without assuming that downstream sections are out-flow, provided that the linear Neumann boundary conditions on the downstream sections are replaced by the nonlinear conditions:

$$-\left(P + \frac{1}{2}\rho |\mathbf{v}|^2\right) \mathbf{n} + \mu \frac{\partial \mathbf{v}}{\partial \mathbf{n}} = \mathbf{0}. \quad (42)$$

*Remark 3.* As already pointed out in [23] and [34], the convective non-linear term of the momentum conservation law is crucial in the deduction of the energy estimate, since it compensates the term arising from the Reynolds transport formula (35). Therefore, the coupled fluid-structure problem with the fluid described by the Stokes equations (where the nonlinear convective term  $(\mathbf{v} \cdot \nabla) \mathbf{v}$  is neglected) fails to be well posed.  $\square$

*Remark 4.* We have introduced homogeneous boundary conditions for the structure for the sake of simplicity only. Indeed, different conditions can be considered as well. More precisely, since the end points  $z = 0, L$  are typically ‘‘artificial boundaries’’, exactly like  $\Gamma_{up}$  and  $\Gamma_{dw}$ , suitable boundary conditions have to be chosen in order not to perturb the numerical results. In particular, ‘‘non-reflective’’ conditions must be selected in order to avoid at the end points spurious reflections in the wave propagation phenomena described by equation (29) (see Sect. 6.2). We remark also that, if  $\alpha = \gamma = 0$ , no boundary condition on  $\frac{\partial \eta}{\partial z}$  is required.

*Remark 5. On the independent-rings model* For the independent-rings model, clearly no boundary conditions on the derivatives of  $\eta$  are needed. In this case, the counterpart of (40) reads:

$$\begin{aligned} & \frac{1}{2} \|\mathbf{v}\|_{L^2(\Omega)}^2(t) + \omega \left\| \frac{\partial \eta}{\partial t} \right\|_{L^2(\Gamma_C^0)}^2(t) + \sigma \omega \|\eta\|_{L^2(\Gamma_C^0)}^2(t) \\ & + \nu \int_0^t \|\mathbf{v}\|_{H^1(\Omega)}^2 dt + \int_0^t \int_{\Gamma_{dw}(t)} |\mathbf{v}|^2 \mathbf{v} \cdot \mathbf{n} d\gamma dt \\ & + \int_0^t \int_{\Gamma_C(t)} \mathbf{v} \frac{\partial \mathbf{v}}{\partial \mathbf{n}} \mathbf{n} d\gamma dt \leq k \end{aligned} \quad (43)$$

Observe, in particular, that, with respect to (40), neglecting the viscous stresses on the walls introduces a boundary integral which is not necessarily positive and this inhibits the deduction of a stability inequality. Conversely, if the viscous stresses are not neglected, we are led to the following inequality:

$$\begin{aligned} & \frac{1}{2} \|\mathbf{v}\|_{L^2(\Omega)}^2(t) + \omega \left\| \frac{\partial \eta}{\partial t} \right\|_{L^2(\Gamma_C^0)}^2(t) + \sigma \omega \|\eta\|_{L^2(\Gamma_C^0)}^2(t) \\ & + \nu \int_0^t \|\mathbf{v}\|_{H^1(\Omega)}^2 dt + \int_0^t \int_{\Gamma_{dw}(t)} |\mathbf{v}|^2 \mathbf{v} \cdot \mathbf{n} d\gamma dt \leq k, \end{aligned} \quad (44)$$

which, in the case of coincidence of outflow and downstream sections (or if the non-linear Neumann flux is prescribed), provides the estimate:

$$\begin{aligned} & \frac{1}{2} \|\mathbf{v}\|_{L^2(\Omega)}^2(t) + \omega \left\| \frac{\partial \eta}{\partial t} \right\|_{L^2(\Gamma_C^0)}^2(t) + \sigma \omega \|\eta\|_{L^2(\Gamma_C^0)}^2(t) \\ & + \nu \int_0^t \|\mathbf{v}\|_{H^1(\Omega)}^2 dt \leq k. \end{aligned} \quad (45)$$

## 5 Numerical methods

Although many (reasonable) simplifications have been adopted for the definition of the coupled problem (28,29,18,31,32), it is impossible to obtain an analytical solution, especially when real human vascular morphologies are considered. Therefore, we need to approximate conveniently the problems at hand in order to obtain a numerical solution. This means that we have to *discretize* both space and time derivatives, replacing the differential operators with algebraic ones.

As already pointed out, a distinctive feature of the fluid-structure problem at hand is the coupling of two different subproblems, the first referring to the fluid (whose solution is characterized by velocity and pressure of the blood), the second to the structure (whose unknown variable is the displacement of the vascular wall). In the previous section, we remarked that the coupled problem is non-linear, since fluid and structure influence themselves according to the matching

relations (31) and (32). The approach we adopt for the numerical study of this problem consists of solving the two subproblems separately, accounting for the reciprocal influence through a suitable approximation of the matching relations. Hence, in the following sections, we consider the approximation of the fluid and the structure problems separately and then we illustrate a simple (explicit) algorithm for the coupling of the two solvers.

### 5.1 Numerical study of the fluid problem

The space discretization of the Navier–Stokes equations (11) can be performed according to many approaches (see e.g. [89, 90, 103]). In the problem at hand, a relevant feature refers to the complex morphologies characterizing the domain where the blood flows. The space discretization method which is probably the most suitable for problems involving such complex geometries is the *Finite Element Method* (FEM). The basic idea is to subdivide the domain into many regions (*elements*) which are typically tetrahedral or prismatic and then approximate the solution with a piecewise polynomial (with respect to the space variables), i.e. with a function which is a polynomial on each element. The interesting feature of this method is that the subdivision (usually called *mesh*) can be unstructured, i.e. it does not necessarily follow preferential directions (as the Cartesian ones) as it is required, for instance, by a finite difference discretization. For this reason, it turns out really suitable for treating complex domains.

Recalling (21) and (22), the problem obtained after the finite element discretization reads as follows.

For every  $t > 0$ , find  $\mathbf{v}_h(t) \in V_h$  and  $p_h(t) \in Q_h$  s.t.

$$\begin{cases} \frac{d}{dt} (\mathbf{v}_h(t), \boldsymbol{\varphi}_h) + a(\mathbf{v}_h(t), \boldsymbol{\varphi}_h) + b(\mathbf{v}_h(t), \mathbf{v}_h(t), \boldsymbol{\varphi}_h) \\ + g(\boldsymbol{\varphi}_h, p_h(t)) = (\mathbf{f}(t), \boldsymbol{\varphi}_h) \quad \forall \boldsymbol{\varphi}_h \in V_h. \\ g(\mathbf{v}_h(t), \boldsymbol{\psi}_h) = 0 \quad \forall \boldsymbol{\psi}_h \in Q_h \end{cases} \quad (46)$$

where  $V_h$  is a suitable piecewise polynomial function subspace of  $\mathbf{H}_{\Gamma_D}^1(\Omega)$ , with dimension  $3 \times N_u$  (in a 3D problem) and  $Q_h$  is a suitable piecewise polynomial function subspace of  $L^2(\Omega)$ , with dimension  $N_p$ . We recall that, in order to have a stable solution for the pressure, the choice of  $V_h$  and  $Q_h$  is not completely free, but should undergo the following *inf-sup condition* (see [5]): *there exists a  $\beta > 0$  such that for all  $q_h \in Q_h$ , there exists  $\boldsymbol{\psi}_h \in V_h$ ,  $\boldsymbol{\psi}_h \neq 0$  s.t.  $(q_h, \boldsymbol{\psi}_h) \geq \beta \|\boldsymbol{\psi}_h\|_1 \|q_h\|_0$  where  $\|\cdot\|_1$  is the norm in  $\mathbf{H}^1(\Omega)$  and  $\|\cdot\|_0$  the norm in  $L^2(\Omega)$ .* This means, for instance, that the same piecewise linear approximation for both velocity and pressure cannot be adopted.

Once the problem has been discretized with respect to the space variables, we have to perform the time discretization of (46). Different strategies are possible. An approach widely adopted relies on a finite difference discretization (see e.g. [90]). In particular, let us adopt a backward Euler time discretization, coupled with a Newton linearization of the convective term. Let  $\mathbf{V}^{n+1} = [\mathbf{V}_i^{n+1}]$  and  $\mathbf{P}^{n+1} = [\mathbf{P}_i^{n+1}]$  denote the vectors of nodal values of  $\mathbf{v}_h(t^{n+1})$  and  $p_h(t^{n+1})$  respectively.

Denote by  $\{\boldsymbol{\varphi}_i\}_{i=1, \dots, N_u}$  a set of basis functions for the space  $V_h$  and by  $\{\boldsymbol{\psi}_i\}_{i=1, \dots, N_p}$  the set of basis functions for

$Q_h$ . Finally, set:

$$M = [m_{ij}] = \left[ \int_{\Omega} (\varphi_i, \varphi_j) d\omega \right] \text{ (the mass matrix),}$$

$$K = [k_{ij}] = [a(\varphi_i, \varphi_j)] \text{ (the stiffness matrix),}$$

$$B_1(\mathbf{W}) = [b_{1,ij}(\mathbf{W})] = \left[ \sum_{k=1}^{N_u} W_k \int_{\Omega} (\varphi_k \cdot \nabla \varphi_j) \cdot \varphi_i d\omega \right],$$

$$B_2(\mathbf{W}) = [b_{2,ij}(\mathbf{W})] = \left[ \sum_{k=1}^{N_u} W_k \int_{\Omega} (\varphi_j \cdot \nabla \varphi_k) \cdot \varphi_i d\omega \right],$$

$$D = [d_{ij}] = [g(\varphi_i, \psi_j)],$$

$$\mathbf{F} = [f_i] = [(\mathbf{f}, \varphi_i)] \text{ and } \mathbf{U}_0 = [U_{0i}] = [(\mathbf{u}_0, \varphi_i)].$$

For instance, in the case of a fully Dirichlet homogeneous problem, the combined Euler–Newton/Finite Element discretization yields at each time level  $t^{n+1}$  in a system of equations of the form

$$A \mathbf{y}^{n+1} = \mathbf{b}^{n+1} \quad (47)$$

where

$$A = \begin{bmatrix} CD^T \\ D \ 0 \end{bmatrix}, \quad \mathbf{y}^{n+1} = \begin{bmatrix} \mathbf{V}^{n+1} \\ \mathbf{P}^{n+1} \end{bmatrix}, \quad \mathbf{b}^{n+1} = \begin{bmatrix} \mathbf{b}_1^{n+1} \\ \mathbf{b}_2^{n+1} \end{bmatrix}. \quad (48)$$

$$C = \frac{1}{\Delta t} M + K + B_1(\mathbf{V}^n) + B_2(\mathbf{V}^n) \quad (49)$$

$$\mathbf{b}_1^{n+1} = \mathbf{F}^{n+1} + \frac{1}{\Delta t} M \mathbf{V}^n + B_1(\mathbf{V}^n) \mathbf{V}^n, \quad \mathbf{b}_2^{n+1} = \mathbf{0}.$$

In particular, the first (block) row of (48) arises from the discretization of the momentum equation, the second from the mass conservation.

It is possible to prove that if the “inf-sup” condition is verified, then the matrix  $A$  is certainly non-singular (see e.g. [5], [90], Chap. 9). In the sequel, we assume this hypothesis to hold.

The solution of system (47) can require a great computational effort, especially in 3D problems. For this reason, many studies have been devoted to the set-up of fractional step methods that aim at solving the whole system as a sequence of smaller problems. The most natural splitting is obviously the separate computation of velocity and pressure fields. A very widespread technique in this perspective refers to the so-called *projection schemes*, which we are going to introduce.

The theoretical framework for projection schemes is provided by the *Helmholtz decomposition principle* (sometimes referred to as *Ladyzhenskaja Theorem*), according to which any vector function  $\mathbf{u} \in \mathbf{L}^2(\Omega)$  can be uniquely represented as  $\mathbf{u} = \mathbf{w} + \nabla \psi$  with  $\mathbf{w} \in \mathbf{L}^2(\Omega)$ ,  $\nabla \cdot \mathbf{w} = 0$ ,  $\mathbf{w} \cdot \mathbf{n} = 0$  on  $\partial\Omega$  and  $\psi \in H^1(\Omega)$ .

Based on this decomposition, the ancestor of projection schemes, formulated by Chorin ([15]) and Temam

([112]), suitably splits problem (46) into the sequence of an advection-diffusion problem computing an intermediate velocity (corresponding to  $\mathbf{u}$ ), a Poisson problem computing the pressure (corresponding to  $\psi$ ) and then the projection of the intermediate velocity on the divergence-free functional space, according to the Helmholtz principle.

An alternative strategy of splitting relies on the following considerations, completely based on the properties of the algebraic system (47). Observe that matrix  $A$  in (48) can be factored according to the following block  $LU$ -decomposition:

$$A = \begin{bmatrix} C & 0 \\ D & -DC^{-1}G \end{bmatrix} \begin{bmatrix} I & C^{-1}G \\ 0 & I \end{bmatrix}. \quad (50)$$

If the original system (48) is now solved through the sequence of steps:

L-step :

$$\begin{cases} C \tilde{\mathbf{U}}^{n+1} = \mathbf{b}_1^{n+1} \\ D \tilde{\mathbf{U}}^{n+1} - DC^{-1}G \tilde{\mathbf{P}}^{n+1} = \mathbf{b}_2^{n+1} \end{cases}$$

U-step :

$$\begin{cases} \mathbf{U}^{n+1} + C^{-1}G \mathbf{P}^{n+1} = \tilde{\mathbf{U}}^{n+1} \\ \mathbf{P}^{n+1} = \tilde{\mathbf{P}}^{n+1} \end{cases} \quad (51)$$

↓

$$\begin{cases} C \tilde{\mathbf{U}}^{n+1} = \mathbf{b}_1^{n+1} \\ -DC^{-1}G \mathbf{P}^{n+1} = \mathbf{b}_2^{n+1} - D \tilde{\mathbf{U}}^{n+1} \\ C \mathbf{U}^{n+1} + G \mathbf{P}^{n+1} = C \tilde{\mathbf{U}}^{n+1} - G \mathbf{P}^{n+1} \end{cases},$$

we have formally reduced the original problem to a sequence of subproblems computing separately velocity and pressure unknowns. Unfortunately, the computational effort is still large, due to the presence of the matrix  $C^{-1}$  in the (2, 2) block of  $L$  and in the (2, 1) block of  $U$ . However,  $C^{-1}$  can be suitably approximated in the  $L$  and  $U$  factors. Should the error introduced by this approximation be of the same order of accuracy (with respect to  $\Delta t$ ) of the unsplit scheme, the corresponding “inexact”  $LU$ -splitting would yield a method that treats the velocity and pressure unknowns separately without loss of accuracy. An analysis of this *inexact factorization approach* can be found in [87]. Here, we limit ourselves to illustrating a particular choice for the approximation of  $C^{-1}$ . Let us substitute the matrix  $DC^{-1}G$  of the (2,2) block in the  $L$  factor with the matrix  $\Delta t DM^{-1}G$ . This choice is formally based on the following approximation, admissible for a  $\Delta t$  sufficiently small:

$$\begin{aligned} C^{-1} &= \left( \frac{1}{\Delta t} M + S \right)^{-1} = \Delta t (I + \Delta t M^{-1}S)^{-1} M^{-1} \\ &= \Delta t \sum_{i=0}^{\infty} (-1)^i (\Delta t M^{-1}S)^i M^{-1} \approx \Delta t M^{-1}, \end{aligned} \quad (52)$$

and yields the following *Yosida* scheme:

$$\begin{cases} C\tilde{U}^{n+1} = b_1^{n+1} \\ -\Delta t D M^{-1} G P^{n+1} = b_2^{n+1} - D\tilde{U}^{n+1} \\ C U^{n+1} = C\tilde{U}^{n+1} - G P^{n+1} \end{cases} \quad (53)$$

The approximation introduced is effective, since the mass matrix  $M$  is easier to invert with respect to  $C$ , especially when the so-called *mass lumping* (i.e. a suitable numerical diagonalization of  $M$ ) is adopted. Moreover, this scheme turns out to be suitable for the treatment of complex boundary conditions, which is often the case in vascular problems, as we have pointed out. An analysis of this scheme can be found in [87, 88].

### 5.2 The Arbitrary Lagrangian Eulerian (ALE) formulation of fluid motion in moving domains

Since the fluid domain is moving, the nodes where the solution is evaluated change their position at every time instant on the boundary and consequently in the inner domain. A specific treatment of this problem is therefore required. A possible strategy is given by the *Arbitrary Lagrangian Eulerian method* (ALE), which is often used as an alternative to the more classical Lagrangian and Eulerian approaches. In the particular case where the moving domain encompasses the coupling of two heterogeneous media, such as a fluid and solid structure, this formulation becomes especially attractive, as it allows the simultaneous use of the Eulerian frame in the fluid domain and the Lagrangian one in the wall structural. Let us illustrate it briefly.

Assume that a continuum occupies at time  $t \geq 0$  a region  $\Omega(t)$  of the space  $\mathbb{R}^n$  that varies along the time, and let  $\Omega_X^0 = \Omega(0)$  be the region occupied at the initial time. A material point of the continuum occupies in  $\Omega_X^0$  the position  $P_0$  whose coordinates are  $X^0 = (X_i^0)$ ,  $i = 1, \dots, n$ , while at time  $t > 0$  it occupies a point  $P$  of coordinates  $x(t) = (x_i)$ ,  $i = 1, \dots, n$  (see Fig. 25). The motion of this point is described by the map:

$$G: \Omega_X^0 \times (0, T) \rightarrow \mathbb{R}^n, \quad (X^0, t) \rightarrow x(t) = G(X^0, t), \quad (54)$$

which is assumed to be continuous and bijective, so that its Jacobian  $J(t) = |\partial x_i / \partial X_j^0|$  is different from zero for all  $t \geq 0$ . The vector

$$\psi(t) = x(t) - X^0 \quad (55)$$

represents the deformation from  $\Omega_X^0$  to  $\Omega(t)$ . Denoting by  $e_i$ ,  $i = 1, \dots, n$  the Cartesian frame of  $\mathbb{R}^n$ ,  $\psi$  can be represented with respect to  $e_i$  either in terms of the *Lagrangian coordinates*  $(X_i^0)$ :

$$\psi(t) = \sum_{i=1}^n \Psi_i(X^0, t) e_i \quad X^0 \in \Omega_X^0 \quad (56)$$

or in terms of the *Eulerian coordinates*  $(x_i)$ :

$$\psi(t) = \sum_{i=1}^n \psi_i(x(t), t) e_i \quad x(t) \in \Omega(t) \quad (57)$$

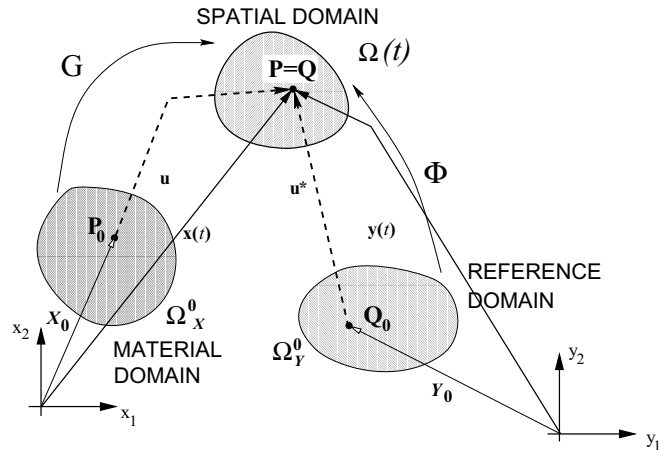


Fig. 25. The ALE perspective: domains, transformations and the corresponding points

The former is called the Lagrangian representation and  $\Omega_X^0$  is usually called the *material domain*, while the latter is called the Eulerian representation and  $\Omega(t)$  is usually called the *spatial domain*.

The Lagrangian coordinate may be thought to be associated to the fluid particle, and the Lagrangian approach follows the material points of the continuum along their displacement in time. At the opposite, in the Eulerian approach, the spatial region at the time  $t$  is considered as fixed and the fluid flows across it (see e.g. [49]).

In particular, for the numerical discretization, in the Eulerian approach the frame of reference is related to the spatial domain, that means that the computational grid is kept fixed, whereas in the Lagrangian approach it changes at the same velocity of the fluid. On the other hand, the fluid velocity is

$$v(t) = \frac{DG(X^0, t)}{Dt} = \frac{\partial x}{\partial t} \Big|_{X^0} = \frac{\partial \psi}{\partial t} \Big|_{X^0} \quad (58)$$

where the symbol  $\frac{\partial x}{\partial t} \Big|_{X^0}$  means partial differentiation of  $x$  with respect to  $t$  with  $X^0$  being fixed, and  $\frac{D}{Dt}$  denotes material derivative.

The ALE approach generalizes both Eulerian and Lagrangian approaches, in that the focus is posed neither on material points nor on a fixed spatial region. Rather, attention is directed at special points or coordinates, say  $Y \in \Omega_Y$  at time  $t = 0$ , that are called ALE coordinates, which will evolve with the continuum, although independently of the motion of material points; the domain  $\Omega_Y$  is usually called *reference domain*.

A choice of remarkable computational interest corresponds to the situation where  $Y$  are the grid coordinates. With this new perspective, the point  $Q$  in the spatial domain  $\Omega(t)$ , corresponding in  $\Omega_Y$  to a point  $Q_0$  of coordinates  $Y$ , has coordinates  $y(t) = \Phi(Y, t)$  at time  $t > 0$ ;  $y(t)$  will still indicate mesh coordinates at time  $t$ , and

$$\psi^*(t) = y(t) - Y \quad (59)$$

the mesh displacement. Correspondingly,

$$w(t) = \frac{\partial x}{\partial t} \Big|_Y = \frac{\partial \psi^*}{\partial t} \Big|_Y \quad (60)$$

is the mesh velocity, which provides the speed of motion of the reference points (the mesh nodes). For a certain time  $t > 0$ , a given point  $\mathbf{x} \in \Omega(t)$  can therefore be regarded as being the image of two different points under two different maps, namely

$$\mathbf{x}(t) = G(\mathbf{X}^0, t) = \Phi(\mathbf{Y}, t) = \mathbf{y}(t). \quad (61)$$

Since the two points  $\mathbf{X}^0$  and  $\mathbf{Y}$  have different motion laws, the identity (61) holds only at that particular time  $t$ .

As previously pointed out, both Lagrangian and Eulerian frames can be recovered as special cases of the ALE approach. Indeed, taking  $\Omega_Y = \Omega_X^0$  and  $\Phi = G$ , one has the Lagrangian formulation, where  $\psi = \psi^*$ . Otherwise, taking  $\Omega_Y = \Omega(t)$  and  $\Phi$  equal to the identity map, one recovers the Eulerian approach, according to which  $\psi^* = 0$  and  $\mathbf{w} = 0$ . Equivalently, we claim that, in the ALE approach, the computational grid is regarded as being an independent frame, moving with velocity  $\mathbf{w}$ . If  $\mathbf{w} = 0$  we reobtain the Eulerian approach, whereas if  $\mathbf{w}$  coincides with the velocity of the fluid  $\mathbf{v}$ , we recover the Lagrangian formulation. If  $\mathbf{w}$  is neither zero nor equal to  $\mathbf{v}$ , we have a truly new formulation.

The arbitrary velocity  $\mathbf{w}$  is chosen in order to enjoy some properties useful in numerical computations. Typically, it is a lifting of the boundary velocities, in order to follow the motion of the boundary domain  $\Gamma(t)$ . At each inner node, it could for instance be chosen to minimize the mesh distortion, defined by means of a suitable functional, as in [19]. Another approach, based on elliptic regularization, is presented in Sect. 5.4.

**5.2.1 The ALE formulation of conservation laws.** In this section, we consider the ALE framework described previously, with the understanding that  $\mathbf{Y}$  denotes the *grid coordinates* (or *ALE coordinates*). The reference domain  $\Omega_Y^0$  will be regarded as the initial domain, and will be denoted by  $\Omega(0)$ . For any scalar function  $g(\mathbf{y}, t)$ , the coordinate transformation  $\mathbf{y}(t) = \Phi(\mathbf{Y}, t)$  yields:

$$\frac{\partial g}{\partial t} \Big|_Y = \frac{\partial g}{\partial t} \Big|_y + \frac{\partial \mathbf{y}}{\partial t} \Big|_Y \cdot \nabla_y g$$

the gradient  $\nabla_y$  being made with respect to the  $\mathbf{y}$  coordinates. Using (60), and noticing that in the current assumption  $\mathbf{w}$  is the grid velocity, we obtain (dropping the suffix for the gradient)

$$\frac{\partial g}{\partial t} \Big|_y = \frac{\partial g}{\partial t} \Big|_Y - \mathbf{w} \cdot \nabla g. \quad (62)$$

This identity highlights the relation between the partial derivative  $\frac{\partial g}{\partial t} \Big|_y$  of  $g$  with respect to  $t$  and the so called *ALE derivative*  $\frac{\partial g}{\partial t} \Big|_Y$  of  $g$ .

We can express (62) in the alternative form

$$\frac{\partial g}{\partial t} \Big|_y = \frac{\partial g}{\partial t} \Big|_Y - \nabla \cdot (\mathbf{w}g) + g(\nabla \cdot \mathbf{w}), \quad (63)$$

which is more suitable when dealing with conservation laws. As a matter of fact, considering the following, scalar, conservation law (unless otherwise specified,  $\frac{\partial g}{\partial t}$  is used instead of

$\frac{\partial g}{\partial t} \Big|_y$  in the remainder of this section):

$$\frac{\partial g}{\partial t} + \nabla \cdot \mathbf{F}(g) = 0 \quad (64)$$

where  $\mathbf{F}$  is the associated flux. Using (63), we obtain

$$\frac{\partial g}{\partial t} \Big|_Y + \nabla \cdot (\mathbf{F}(g) - \mathbf{w}g) = -g(\nabla \cdot \mathbf{w}), \quad (65)$$

or, equivalently

$$\frac{\partial g}{\partial t} \Big|_Y + \nabla \cdot \mathbf{F}_{ALE}(g) = s(\mathbf{w}), \quad (66)$$

where  $\mathbf{F}_{ALE}(g) = \mathbf{F}(g) - \mathbf{w}g$  is the *ALE flux*, and  $s(\mathbf{w}) = -g(\nabla \cdot \mathbf{w})$  is a source term (both depend on the grid velocity  $\mathbf{w}$ ).

The generalization to the vector case is in order. Indeed, consider instead of (64):

$$\frac{\partial g_k}{\partial t} + \sum_{i=1}^n \frac{\partial}{\partial y_i} [h_i(g_k)] = 0 \quad k = 1, \dots, q \quad (q \geq 2). \quad (67)$$

Proceeding as above, we obtain:

$$\begin{aligned} \frac{\partial g_k}{\partial t} \Big|_Y + \sum_{i=1}^n \frac{\partial}{\partial y_i} [h_i(g_k) - w_i g_k] &= -g_k(\nabla \cdot \mathbf{w}), \\ k &= 1, \dots, q, \end{aligned} \quad (68)$$

In compact form, (67) reads:

$$\frac{\partial \mathbf{g}^T}{\partial t} + \nabla \cdot \mathcal{F}(\mathbf{g}) = \mathbf{0}, \quad (69)$$

where  $\mathbf{g}^T$  is the row vector  $(g_1, \dots, g_q)$ ,  $(\nabla \cdot)$  denotes the row vector  $(\frac{\partial}{\partial y_1}, \dots, \frac{\partial}{\partial y_n})$  and  $\mathcal{F}(\mathbf{g})$  the  $n \times q$  matrix of elements  $f_i(g_k)$ ,  $1 \leq i \leq n$ ,  $1 \leq k \leq q$ , while (68) reads

$$\frac{\partial \mathbf{g}^T}{\partial t} \Big|_Y + \nabla \cdot \mathcal{F}_{ALE}(\mathbf{g}) = \mathcal{S}^T(\mathbf{g}), \quad (70)$$

where the modified flux  $\mathcal{F}_{ALE}(\mathbf{v})$  is now the  $n \times q$  matrix of elements  $f_i(u_k) - w_i g_k$  and  $\mathcal{S}^T(\mathbf{v})$  the row vector  $(-g_1(\nabla \cdot \mathbf{w}), \dots, -g_q(\nabla \cdot \mathbf{w}))$ .

If the differential equation is not in conservative form, the identity (62) is often more suitable than (63). For instance, considering the momentum equations in the Navier–Stokes system (1), proceeding as above, its ALE version becomes:

$$\frac{\partial v_k}{\partial t} \Big|_Y - \nu \Delta v_k + \frac{\partial p}{\partial y_k} + (\mathbf{v} - \mathbf{w}) \cdot \nabla v_k = f_k \quad k = 1, \dots, n. \quad (71)$$

In vector form, this is equivalent to:

$$\frac{\partial \mathbf{v}}{\partial t} \Big|_Y - \nu \Delta \mathbf{v} + \nabla p + (\mathbf{v} - \mathbf{w}) \cdot \nabla \mathbf{v} = \mathbf{f}, \quad (72)$$

which amounts to changing the original convective velocity  $\mathbf{v}$

in the new one (relative to the grid velocity)  $\mathbf{v} - \mathbf{w}$ .

The integral form of the conservation law (66), which is at the base of any finite volume approximation, is easily derived using the Reynolds transport formula (35) with  $\psi = g$  and using from (64):

$$\begin{aligned} \frac{d}{dt} \int_{\Omega(t)} g d\omega &= \int_{\Omega(t)} [\nabla \cdot (\mathbf{w}g - \mathbf{F}(g))] d\omega \\ &= - \int_{\Omega(t)} [\nabla \cdot \mathbf{F}_{ALE}(g)] d\omega. \end{aligned} \quad (73)$$

Then, by the Gauss theorem, it follows that:

$$\frac{d}{dt} \int_{\Omega(t)} g d\omega + \int_{\partial\Omega(t)} \mathbf{F}_{ALE}(g) \cdot \mathbf{n} d\gamma = 0. \quad (74)$$

Observe that it is possible to obtain the ALE formulation from the Eulerian one simply by substituting for the real flux  $\mathbf{F}$ , the ALE flux  $\mathbf{F}_{ALE}$ . This is the driving mechanism for the further deduction of ALE formulations. In particular, in view of finite element approximations, an integral variational formulation of (64) has to be derived. On a fixed domain  $\Omega = \Omega_0$ , this would simply be:

$$\frac{d}{dt} \int_{\Omega} \hat{u} g d\omega + \int_{\Omega} \hat{u} \nabla \cdot \mathbf{F}(g) d\omega = 0, \quad (75)$$

for all test function  $\hat{u} = \hat{u}(\mathbf{y})$  defined on  $\Omega$ , belonging to a suitable function space  $\hat{U}$ . The corresponding function space in  $\Omega(t)$  is identified through the ALE map:

$$\begin{aligned} U(t) &= \left\{ u(\mathbf{y}, t) \mid u(\mathbf{y}(\mathbf{Y}, t), t) = \hat{u}(\mathbf{Y}), \mathbf{Y} \in \hat{\Omega} \right\} \\ &= \left\{ u \mid u \circ \Phi = \hat{u}, \hat{u} \in \hat{U} \right\}. \end{aligned} \quad (76)$$

As  $\hat{u}$  is (obviously) independent of time, using (62) with  $\hat{u}$  instead of  $g$ , we obtain:

$$0 = \frac{\partial \hat{u}}{\partial t} \Big|_{\mathbf{y}} + \mathbf{w} \cdot \nabla \hat{u}. \quad (77)$$

Consider now the variational formulation in  $\Omega(t)$  using the test functions  $u \in U(t)$ :

$$\int_{\Omega(t)} u \frac{\partial g}{\partial t} d\omega + \int_{\Omega(t)} u \nabla \cdot \mathbf{F}(g) d\omega = 0 \quad (78)$$

Using the chain rule and (77), we have:

$$u \frac{\partial g}{\partial t} \Big|_{\mathbf{y}} = \frac{\partial u g}{\partial t} \Big|_{\mathbf{y}} - g \frac{\partial u}{\partial t} \Big|_{\mathbf{y}} = \frac{\partial u g}{\partial t} \Big|_{\mathbf{y}} + g (\mathbf{w} \cdot \nabla u). \quad (79)$$

The latter relationship, used in equation (78), yields:

$$\int_{\Omega(t)} \frac{\partial u g}{\partial t} \Big|_{\mathbf{X}} d\omega + \int_{\Omega(t)} g (\mathbf{w} \cdot \nabla u) + u \nabla \cdot \mathbf{F}(g) d\omega = 0.$$

Using the Reynolds transport formula (35) with  $\psi = gv$ , we finally obtain:

$$\frac{d}{dt} \int_{\Omega(t)} u g d\omega + \int_{\Omega(t)} u \nabla \cdot \mathbf{F}_{ALE}(g) d\omega = 0 \quad \forall u \in U(t) \quad (80)$$

which can therefore be regarded as the ALE variational formulation of the conservation law (66). Note that, formally, the integral form (73) is a special case of (80) when taking the test function  $u$  equal to unity. Upon integrating in time from 0 to  $t$ , we derive from (80):

$$\begin{aligned} \int_{\Omega(t)} u(t) g(t) d\omega - \int_{\Omega_0} \hat{u} g(0) d\omega \\ + \int_0^t \int_{\Omega(\tau)} u(\tau) \nabla \cdot \mathbf{F}_{ALE}(g)(\tau) d\omega d\tau = 0, \end{aligned} \quad (81)$$

for all  $u(\tau) \in U(\tau)$ .

In the vector case, the counterpart of (79) reads:

$$\frac{\partial \mathbf{g}}{\partial t} \cdot \boldsymbol{\varphi} = \frac{\partial (\mathbf{g} \cdot \boldsymbol{\varphi})}{\partial t} + (\mathbf{w} \cdot \nabla) \boldsymbol{\varphi} \cdot \mathbf{g}. \quad (82)$$

Using (82) and proceeding as above, we obtain the counterpart of (80) for the Navier–Stokes momentum equation:

$$\begin{aligned} \frac{d}{dt} \int_{\Omega(t)} \mathbf{v} \cdot \boldsymbol{\varphi} d\omega + \int_{\Omega(t)} [(\mathbf{v} - \mathbf{w}) \cdot \nabla] \mathbf{v} \cdot \boldsymbol{\varphi} d\omega \\ - \int_{\Omega(t)} \nabla \cdot \mathbf{w} \mathbf{v} \cdot \boldsymbol{\varphi} d\omega + \nu \int_{\Omega(t)} \nabla \mathbf{v} \cdot \nabla \boldsymbol{\varphi} d\omega \\ - \int_{\Omega(t)} p \nabla \cdot \boldsymbol{\varphi} d\omega = \int_{\Gamma_{wall}} [-p \mathbf{n} + \nu \nabla \mathbf{v} \cdot \mathbf{n}] \cdot \boldsymbol{\varphi} \quad \forall \boldsymbol{\varphi} \in V(t) \end{aligned} \quad (83)$$

which is then integrated in time as in (81).

*Remark 6.* In the frame of the temporal discretization approximation of the conservation law (65), the domains  $\hat{\Omega}$  and  $\Omega(t)$  will typically be replaced by  $\Omega(t^n)$  and  $\Omega(t^{n+1})$ , respectively,  $t^n = n \Delta t$  being the  $n^{\text{th}}$  time level and  $\Delta t$  the temporal step size.  $\square$

**5.2.2 Geometric conservation laws and finite element discretization.** A requirement that is often made for the ALE description is that a uniform flow field should be maintained as such all along the time evolution. This request yields constraints on geometrical quantities (and of course on both the temporal and spatial discretization schemes which are being used), but not on the solution  $g$  of the conservation law at hand. This reason motivates the name *geometric conservation laws* given to these relationships. For a detailed introduction and analysis, see e.g. [30, 53, 129], where this issue is addressed in the framework of finite volume approximations. For variational formulations of conservation laws, we simply report here the results found in [26].

If  $g$  must represent a uniform constant state, then  $F = 0$ , and from (80) we deduce that:

$$\frac{d}{dt} \int_{\Omega(t)} u d\omega - \int_{\Omega(t)} u \nabla \cdot \mathbf{w} d\omega = 0 \quad \forall u \in U(t). \quad (84)$$

or, equivalently,

$$\int_{\Omega(t)} u d\omega - \int_{\Omega_0} \hat{u} d\omega = \int_0^t \int_{\Omega(\tau)} u(\tau) \nabla \cdot \mathbf{w} d\omega d\tau \quad \forall \hat{u} \in \hat{U} \quad (85)$$

Observe that (84) (or (85)) would not change if the conservation law contained diffusion or propagation terms (as in the Navier–Stokes equations). Indeed, both terms vanish in the case of a constant state solution.

The same kind of equation must hold for the discretized problem. When using finite elements for spatial approximations, the test-function space  $\hat{U}$  is approximated by a finite element subspace of the form:

$$\hat{U}_h = \left\{ \hat{u}_h \in \hat{U} : \hat{u}|_{\mathcal{S}} \in \mathbb{P}_k(\mathcal{S}), \quad \forall \mathcal{S} \in \mathcal{T}_h \right\} \quad (86)$$

where  $\mathcal{T}_h$  is the finite element triangulation and  $\mathcal{S}$  a finite element and  $k \geq 1$  is the piecewise polynomial degree. In particular, if we denote by  $\{u_{hj}\}$ ,  $j = 1, \dots, N_h$ , the shape functions which form a basis of  $\hat{U}_h$ , equation (85) is equivalent to requiring that:

$$\int_{\Omega(t)} u_{hj}(t) d\omega - \int_{\Omega_0} \hat{u}_{hj} d\omega = \int_0^t \int_{\Omega(\tau)} u_{hj}(\tau) \nabla \cdot \mathbf{w}(\tau) d\omega d\tau \quad (87)$$

$$\forall j = 1, \dots, N_h$$

where  $u_{hj}(t)$  are such that  $u_{hj} \circ \Phi = \hat{u}_{hj}$ . If isoparametric elements are used to represent the mesh displacement, then:  $\Phi \in \hat{U}$ , therefore

$$\mathbf{y}(t) = \Phi(\mathbf{Y}, t) = \sum_{j=1}^{N_h} \hat{u}_{hj}(\mathbf{Y}) y_{hj}(t). \quad (88)$$

For each  $j$ , the node coordinate  $y_{hj}(t)$  is assumed to be a polynomial of degree  $k$  with respect to  $t$ , for  $t$  varying in each time step  $[t^n, t^{n+1}]$ , in order that the motion of each finite element  $\mathcal{S}$  be described through the motion of all its nodes (see Fig. 26).

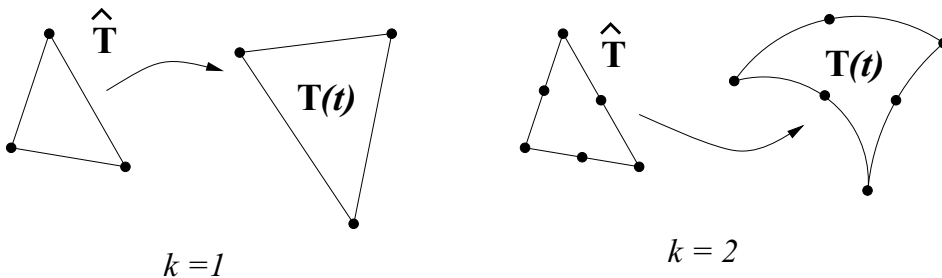


Fig. 26. Isoparametric transformations in time of finite elements (linear and quadratic case)

Consequently, the mesh velocity (60) is given by:

$$\mathbf{w}(t) = \sum_{j=1}^{N_h} \hat{u}_{hj}(\mathbf{Y}) \frac{\partial y_{hj}}{\partial t}(t) \quad (89)$$

and is therefore a piecewise  $\mathbb{P}^k$  in space and  $\mathbb{P}^{k-1}$  in time on each time step  $[t^n, t^{n+1}]$ . After passing to the reference domain  $\Omega_0$ , we can verify that the function under the time integral on the right-hand side of (87) is a polynomial of degree  $k \times d - 1$  with respect to the variable  $t \in [t^n, t^{n+1}]$ , for each  $n \geq 0$ ,  $d$  being the dimension of the domain  $\Omega$ . In other words, (87) on the time interval  $[t^n, t^{n+1}]$  can be written:

$$\int_{\Omega(t^{n+1})} u_{hj}^{n+1} d\omega - \int_{\Omega(t^n)} \hat{u}_{hj} d\omega = \int_{t^n}^{t^{n+1}} \int_{\Omega(\tau)} u_{hj}(\tau) \nabla \cdot \mathbf{w}(\tau) d\tau$$

$$\equiv \int_{t^n}^{t^{n+1}} H(\tau) d\tau \quad (90)$$

where  $H(t)$  is a polynomial for  $t \in [t^k, t^{k+1}]$  with degree  $k \times d - 1$ . Then, we can summarize the previous remarks in the following proposition.

**Proposition 1.** For the time integral in  $[t^n, t^{n+1}]$ , we need to use an integration formula whose degree of exactness must be at least  $k \times d - 1$  in order to guarantee that the time integration be carried out exactly and the geometric conservation laws (90) be satisfied at the discrete level.

In particular, for  $d = 2$  and  $k = 1$  (piecewise linear elements), the quadrature formula should have degree of exactness  $\geq 1$ . Both the mid-point rule and the trapezoidal rule enjoy this property. The former would give:

$$\int_{\Omega(t^{n+1})} u_{hj}^{n+1} d\omega - \int_{\Omega(t^{n-1})} \hat{u}_{hj} d\omega = 2\Delta t H(t^n) \quad (91)$$

(with  $\Omega(t^{n-1})$  playing the role of reference domain) and the latter:

$$\int_{\Omega(t^{n+1})} u_{hj}^{n+1} d\omega - \int_{\Omega(t^n)} \hat{u}_{hj} d\omega = \frac{\Delta t}{2} [H(t^{n+1}) + H(t^n)] \quad (92)$$

(this time, it is  $\Omega(t^n)$  which plays the role of reference domain). Instead, both forward and backward Euler schemes would not guarantee the fulfilment of (90).

For  $k$  greater than one, the integration formula should be upgraded accordingly (e.g., if  $k = 2$  Simpson's rule would be adequate).

*Remark 7.* In particular cases, the accuracy requirement specified in Prop. 1 could be relaxed. Indeed, suppose that the  $\Omega$  is a  $d$  continuum, so that the boundary  $\Gamma$  is a  $d-1$  surface. Suppose that every point of  $\Gamma$  cannot move in the all  $d$ -dimensional space, but there is a restriction to the boundary motion to a  $s$ -dimensional variety, being  $s \leq d-1$ . Then, it is possible to prove that the degree of exactness required by the GCL reduces to  $k \times s - 1$ . In particular, when a 2D fluid is coupled with a 1D structure, and the structure moves only transversally, this means that the degree of exactness is not  $2k-1$ , but  $k-1$ . Therefore, with linear finite elements, the Euler formula is also adequate (see [70]).

### 5.3 Numerical study of the structure problem

For the sake of completeness, we give a sketch of the numerical solution of structure model (29) in the case when  $\alpha = 0$ , i.e.:

$$\frac{\partial^2 \eta}{\partial t^2} = \beta \frac{\partial^2 \eta}{\partial z^2} + \gamma \frac{\partial^3 \eta}{\partial t \partial z^2} + \sigma \eta + \hat{\Phi}, \quad (93)$$

that holds for every part of the compliant wall for  $z \in [0, L]$ , with the associated boundary conditions  $\eta|_{z=0} = \eta|_{z=L} = 0$ . We adopt a discretization by means of piecewise linear finite elements (see Fig. 27).

The space-discretized continuous-in-time formulation of the problem is the following:

$$\begin{aligned} \text{find } \eta_h \in W_h &\equiv \{ \mu_h \in C^0[0, L] : \mu_h|_{[z_{i-1}, z_i]} \in \mathbb{P}^1, \\ &\mu_h(z_0) = \mu_h(z_N) = 0 \} \text{ s.t. :} \\ \frac{d^2}{dt^2} (\eta_h, \xi_h) + \beta \mathcal{A}(\eta_h, \xi_h) + \gamma \frac{d}{dt} \mathcal{A}(\eta_h, \xi_h) + \sigma (\eta_h, \xi_h) \\ &= \langle \hat{\Phi}, \xi_h \rangle. \end{aligned} \quad (94)$$

for all  $\xi_h \in W_h$ .

In (94), we have set  $\mathcal{A}(\xi, \psi) \equiv \left( \frac{\partial \xi}{\partial z}, \frac{\partial \psi}{\partial z} \right) = \int_0^L \frac{\partial \xi}{\partial z} \frac{\partial \psi}{\partial z} dz$ .

Let us consider a second-order time discretization scheme:

$$\begin{aligned} &\frac{(\eta_h^{n+1}, \xi_h) - 2(\eta_h^n, \xi_h) + (\eta_h^{n-1}, \xi_h)}{\Delta t^2} \\ &+ \gamma \frac{\mathcal{A}(\eta_h^{n+1}, \xi_h) - \mathcal{A}(\eta_h^{n-1}, \xi_h)}{2\Delta t} \\ &+ \beta \mathcal{A}(\eta_h^n, \xi_h) + \sigma (\eta_h^n, \xi_h) = \Phi_i^n \end{aligned} \quad (95)$$

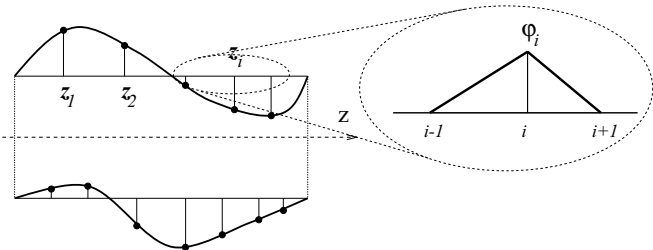


**Fig. 27.** Space discretization of the structure problem with a piecewise linear basis (on the right)

Since the bilinear form  $\mathcal{A}(\cdot, \cdot)$  is symmetric and coercive in  $W_h$ , if  $N$  is the dimension of  $W_h$ , there exists a set of values  $0 \leq \lambda_{1,h} \leq \lambda_{2,h} \leq \dots \leq \lambda_{N,h}$  and a basis  $\phi_{i,h} \in W_h$  orthogonal in  $W_h$  and orthonormal in  $L^2(\Gamma_C)$  such that:

$$\mathcal{A}(\phi_{i,h}, v_h) = \lambda_{i,h} (\phi_{i,h}, v_h) \quad \forall v_h \in V_h. \quad (96)$$

Considering the basis  $\{\phi_{i,h}\}$  as test functions, for  $i = 1, 2, \dots, N$  we have the equations:

$$\begin{aligned} \left(1 + \gamma \frac{\Delta t}{2} \lambda_{i,h}\right) \eta_i^{n+1} + (\Delta t^2 (\beta \lambda_{i,h} + \sigma) - 2) \eta_i^n \\ + \left(1 - \gamma \frac{\Delta t}{2} \lambda_{i,h}\right) \eta_i^{n-1} = f_i^n. \end{aligned} \quad (97)$$

where  $\eta_i \equiv (\eta_h, \phi_{i,h})$  and  $\Phi_i \equiv (\Phi, \phi_{i,h})$ .

For the stability of the system, it is sufficient that the roots of the equation:

$$\begin{aligned} \left(1 + \gamma \frac{\Delta t}{2} \lambda_{i,h}\right) \rho^2 + (\Delta t^2 (\beta \lambda_{i,h} + \sigma) - 2) \rho \\ + \left(1 - \gamma \frac{\Delta t}{2} \lambda_{i,h}\right) = 0 \end{aligned} \quad (98)$$

are such that  $|\rho| < 1$ . A simple algebraic calculation shows that this condition holds if and only if  $\forall i$ :

$$\begin{aligned} \left(1 + \gamma \frac{\Delta t \lambda_{i,h}}{2}\right) > \left(1 - \gamma \frac{\Delta t \lambda_{i,h}}{2}\right) \quad \text{and} \\ -2 < \Delta t^2 (\beta \lambda_{i,h} + \sigma) - 2 < 2. \end{aligned} \quad (99)$$

The first inequality is obviously verified since  $\gamma > 0$ , which is true by hypothesis. The remaining condition reads:

$$0 < \Delta t^2 (\beta \lambda_{i,h} + \sigma) < 4. \quad (100)$$

since by hypothesis  $\beta$  and  $\sigma$  are positive  $\Delta t^2 (\beta \lambda_{i,h} + \sigma) > 0$  always. Therefore, the condition for the stability is:

$$\Delta t^2 < \frac{4}{\beta \lambda_{i,h} + \sigma}. \quad (101)$$

In the case of a Finite Element discretization of a 1D structure,  $\lambda_{i,h}$  are the eigenvalues of the matrix  $M_S^{-1} K_S$ , where  $M_S$  is the mass matrix of the structure and  $K_S$  is the corresponding stiffness matrix. In this case, denoting some positive constants by  $C_i$  ( $i = 1, 2, 3$ ), we have (see e.g. [90], Theorem 2.5.1 and Prop. 6.3.2)  $|\lambda_{i,h}| < C_1 h^{-2}$ , so the stability condition becomes:

$$\Delta t < \frac{C_2 h}{\sqrt{C_3 + h^2}}. \quad (102)$$

### 5.4 Numerical study of the coupled fluid-structure problem

So far, we have illustrated the features of the schemes used for the fluid and the structure problems separately. To match the two solvers, we can proceed in many different ways (see [34] for an overview of the strategies that can be followed in this respect). Similarly, different strategies can be

considered for the computation of the grid velocity in the ALE perspective. In this section, we illustrate, in particular, an explicit algorithm for the coupling of fluid and structure. Different, more complex strategies of coupling have been carried out in [69] (see Sect. 6.2).

The original coupled problem (28), (29), (31), (32), (18) and (30) is split at each time into a structure problem and in a fluid problem, communicating with one another through a forcing term on the wall due to the fluid, and a boundary term for the fluid, given by the velocity of the wall. Figure 28 illustrates the basic steps of the algorithm which we are going to illustrate for advancing from time level  $n$  to time level  $n + 1$ . We will suppose that the pressure nodes of the fluid grid coincide with the nodes of the 1D grid of the structure. In the case of different nodes (non-conforming case – see Fig. 29), the continuity between  $\frac{\partial \eta}{\partial t} e_y$  and  $\mathbf{v}$  is enforced only weakly, through suitable projection operators. Thanks to our hypothesis, we do not face this issue here: an analysis of the non-conforming case is given in [34].

The unknowns referring to the velocity and pressure will be denoted by  $\mathbf{V}$  and  $\mathbf{P}$  respectively as usual, while the ones relative to the structure are denoted by  $\mathcal{H}$ .

1. *Solving the structure problem (vessel wall):* As a first step, we compute the wall configuration by means of the fol-

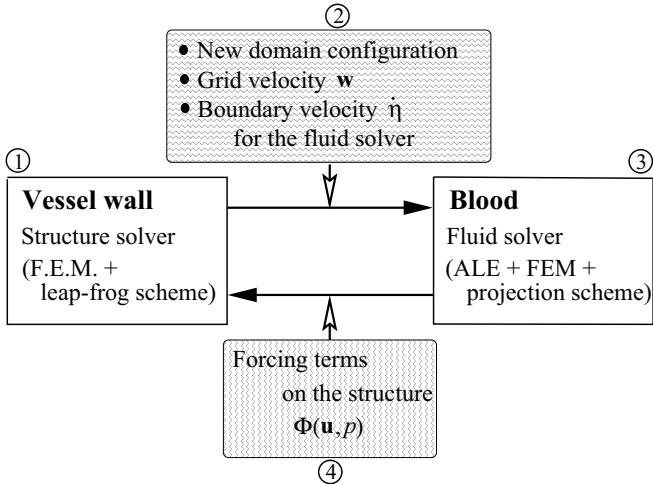


Fig. 28. Representation of the splitting in two subproblems for our approach

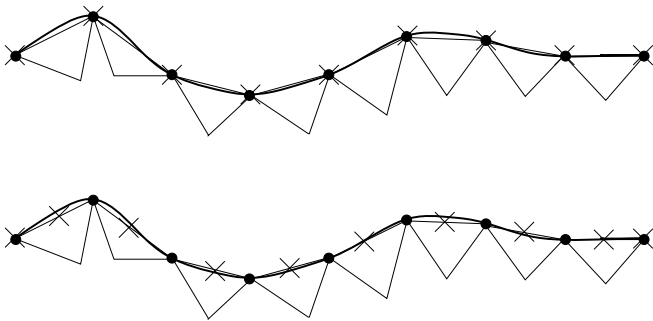


Fig. 29. Domain configuration when structure nodes ( $\times$ ) and boundary nodes for the fluid ( $\bullet$ ) are coincident (top) or are different (bottom)

lowing equation:

$$\begin{aligned} \frac{1}{\Delta t^2} M_s \mathcal{H}^{n+1} + \gamma \frac{1}{2\Delta t} K_s \mathcal{H}^{n+1} &= \frac{2}{\Delta t^2} M_s \mathcal{H}^n \\ &+ \beta K_s \mathcal{H}^n - \sigma M_s \mathcal{H}^n - \frac{1}{\Delta t^2} M_s \mathcal{H}^{n-1} \\ &+ \gamma \frac{1}{2\Delta t} K_s \mathcal{H}^{n-1} + \Phi(\mathbf{V}^n, \mathbf{P}^n), \end{aligned} \quad (103)$$

where  $K_s$  and  $M_s$  are the stiffness and mass matrix for the structure respectively, and  $\Phi$  is the discrete counterpart of the matching relation (32).

At the first time level, the scheme is suitably modified, taking into account the initial data on the position and the velocity at time  $t = 0$ .

2. *Updating domain configuration and boundary conditions for the fluid solver:* Once  $\mathcal{H}^{n+1}$  is known, we can compute the domain deformations and the movement of the nodes of the grid for the fluid. The new position of the boundary is computed through the relations:

$$x_i^{n+1} = x_i^0, \quad y_i^{n+1} = y_i^0 + \eta_i^{n+1}. \quad (104)$$

The displacement of the nodes of the grid for the fluid is obtained as a lifting into the fluid domain of the boundary displacement. More precisely, we introduce the unknowns  $\mathbf{l}^{n+1}$  which denote the displacements of the nodes at time  $n + 1$  and solve the problem:

$$\begin{cases} -\Delta \mathbf{l}^{n+1} = 0 & \text{in } \Omega \\ \mathbf{l}^{n+1} = \begin{bmatrix} 0 \\ \eta^{n+1} - \eta^n \end{bmatrix} & \text{on } \Gamma_C \\ \mathbf{l}^{n+1} = \mathbf{0} & \text{on } \Gamma_F. \end{cases} \quad (105)$$

Then, we update the position  $\mathbf{x}$  of the nodes of the mesh:

$$\mathbf{x}^{n+1} = \mathbf{x}^n + \mathbf{l}^{n+1} \quad \text{in } \Omega. \quad (106)$$

We compute the mesh velocity  $\mathbf{w}$  by the equation:

$$\mathbf{w}^{n+1} = \frac{1}{\Delta t} (\mathbf{x}^{n+1} - \mathbf{x}^n). \quad (107)$$

The idea underlying this approach is to take advantage of the regularization due to the inversion of the Laplace operator in order to have an acceptable mesh. From time to time, however, it could be necessary to remesh the whole domain, if the grid is too distorted after a certain number of steps (see also [69]).

Another strategy consists of computing the boundary velocity by the equations ( $u_1$  is the velocity component along  $x$ ,  $u_2$  is the one along  $y$ ):

$$\begin{cases} u_1 = 0 \\ u_2 = \frac{\eta^{n+1} - \eta^n}{\Delta t} \end{cases} \quad \text{on } \Gamma_C. \quad (108)$$

Then, the mesh velocity is the solution of the problem:

$$\begin{cases} -\Delta \mathbf{w}^{n+1} = 0 & \text{in } \Omega \\ \mathbf{w}^{n+1} = \mathbf{u}^{n+1} & \text{on } \Gamma_C \\ \mathbf{w}^{n+1} = \mathbf{0} & \text{on } \Gamma_F. \end{cases} \quad (109)$$

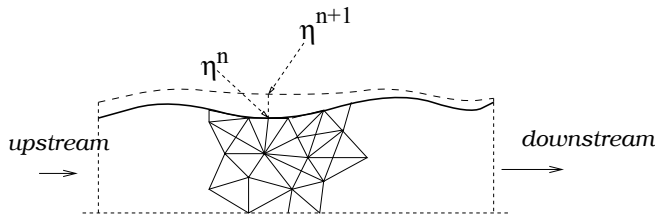


Fig. 30. Updating of the mesh

Finally, the mesh update is obtained by:

$$\mathbf{x}^{n+1} = \mathbf{x}^n + \Delta t \mathbf{w}^{n+1}. \quad (110)$$

For a comparison of the two strategies, see [69].

### 3. Solving the blood flow problem

The ALE formulation of the Navier–Stokes equations (1) is solved by projection schemes or other methods based on inexact factorizations. Remember that the choice of the time-advancing method has to satisfy the Geometric Conservation Laws (90).

### 4. Computing pressure and forcing terms for the structure model.

Finally, we need to update the right-hand side of (103), i.e. we compute the integrals:

$$I(\xi_h) = \int_{\Gamma_{wall}} \Phi(\mathbf{v}_h^{n+1}, p_h^{n+1}) \cdot \mathbf{e}_y \xi_h d\gamma \quad (111)$$

for all  $\xi_h \in W_h$ ,  $\Phi$  being the discrete counterpart of the matching term (32).

This algorithm performs an explicit coupling between the fluid and the structure problems; therefore, it should generally undergo stability limitations on the time step. These limitations could turn out to be restrictive in practical computations. In such cases, different implicit strategies for the coupling have to be investigated (see e.g. [69] and Sect. 6.2).

## 6 Numerical results

In this conclusive section, we illustrate some numerical results obtained so far after application of the techniques discussed in the previous sections. The aim here is to show the potential of the numerical modelling to reproduce realistic flow fields relevant for medical investigations. A thorough quantitative validation of these results is carried out elsewhere.

### 6.1 3D carotid model

The stenosed carotid bifurcation of Fig. 19, reconstructed in Fig. 20 and 21, has been considered for a numerical simulation with the fluid density  $\rho = 1 \text{ g cm}^{-3}$  and the dynamic viscosity  $\mu = 0.04 \text{ g s cm}^{-1}$ . An inflow parabolic profile is prescribed on the upstream section, while, on the downstream sections, Neumann conditions (18)<sub>2</sub> with  $d = 0$  are assigned. The peak Reynolds number is equal to 800.

The computations have been carried out using piecewise quadratic finite elements for velocity components, piecewise

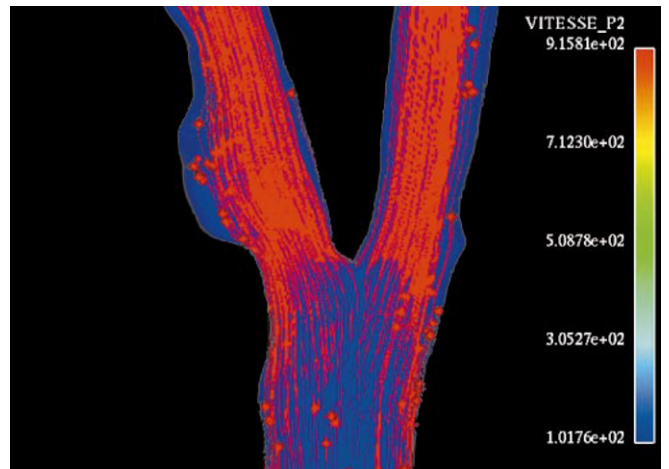


Fig. 31. Computed flow patterns in the carotid bifurcation of Fig. 19 during systole

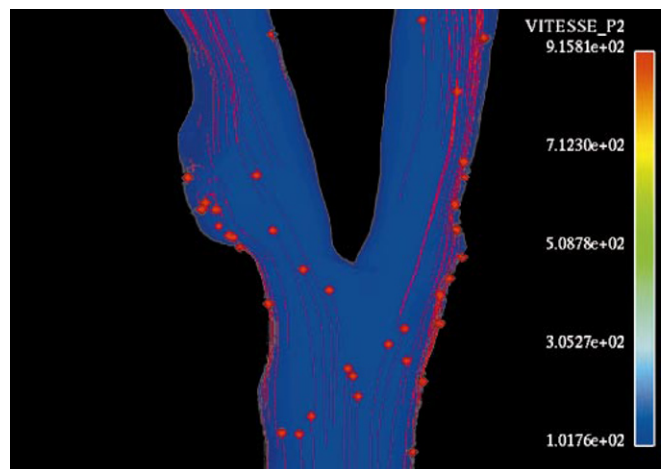


Fig. 32. Computed flow patterns in the carotid bifurcation of Fig. 19 during diastole

linear for pressure, coupled with a Chorin–Temam projection method for the time advancement.

Figures 31 and 32 show the local flow patterns (particle traces) during the systolic and diastolic phase respectively. The presence of flow reversal zones downstream from the plaque, possible responsible for a further development of the stenosis, is rather evident.

### 6.2 2D compliant pipe

The numerical results in this subsection were obtained by F. Nobile in [69]. A simple case of a 2D compliant pipe with 1 cm diameter and 6 cm length was considered as an application of the techniques described in Sect. 4 and 5. The fluid is described by the Navier–Stokes equations (with  $\mu = 0.035 \text{ g cm}^{-1} \text{ s}^{-1}$ ), and the walls are modelled by the “generalized rod” equation (27), with  $a = 0$ ,  $b = 2.5 \times 10^4 \text{ g s}^{-2}$ ,  $c = 10^{-2} \text{ g s}^{-1}$ ,  $e = 4 \times 10^5 \text{ g cm}^{-2} \text{ s}^{-1}$  and  $\rho_{wall} = 0.11 \text{ g cm}^{-2}$ . Homogeneous Dirichlet boundary conditions are assigned.

The fluid equations are solved using an ALE approach, with a piecewise linear finite element space discretization.

More precisely, in order to fulfil the *inf-sup* condition, the pressure is piecewise linear on triangular elements and the velocity is linear over each of the four subtriangles obtained by joining the midpoints of the edges of each pressure triangle (this is the so-called  $\mathbb{P}^1$ -iso $\mathbb{P}^2$ ,  $\mathbb{P}^1$  discretization (see [7])).

For the time discretization, the Yosida scheme was adopted. The equation (27) was solved using a  $\mathbb{P}^1$  finite element space discretization (see Fig. 27), with nodes coincident with the ones of the fluid discretization (see Fig. 29 top). When the time advancement for the structure problem is carried out by means of scheme (95), and the fluid and structure solvers are coupled through the simple explicit algorithm described in Sect. 5.4, the stability requirement on the time-step size becomes too restrictive. For this reason, more complex time-advancing schemes for the structure solver and coupling algorithms are mandatory. In the numerical results of this subsection, a Newmark implicit time-advancing method (see e.g. [97]) and an implicit algorithm for the coupling of the two solvers were considered: more details can be found in [69].

Figure 33 and 34 illustrate different instants ( $t = 0, 0.006, 0.018, 0.02$  s respectively) of the displacement and the velocity of the upper wall and the pressure field in the pipe. The initial conditions prescribe the Hagen-Poiseuille parabolic flow, with a constant pressure gradient. The boundary conditions prescribe a mean pressure drop of  $-6 \times 10^{-4}$  mm Hg between the upstream and the downstream sections according to the “do-nothing” principle, as described in Sect. 3.3. Even

though the displacements are pretty small, it is evident that the compliance of the walls induces the presence of a pressure wave travelling downstream, i.e. advecting the upstream value of the pressure towards the downstream section. Due to the presence of “reflective” boundary conditions (see Remark 4), there is a spurious reflection of the pressure wave when it reaches the downstream artificial section (Fig. 34). The setup of suitable absorbing boundary conditions at the artificial sections for the coupled fluid/structure problem is a field of research in this context.

### 6.3 2D anastomosis models

The simulations of the present subsection aim to illustrate the presence of recirculation zones in a simple 2D anastomosis. We consider the middle plane of a 3D glass model provided by the Vascular Surgery Skejby Sygheus of the Aarhus University Hospital in Denmark (see Sect. 6.4 and [39]). The junction angle is 15 degrees. The normal section of the occluded branch (below) is 1 cm, and the one of the by-pass (above) is 0.96 cm (see Fig. 35). The simulations were carried out setting the dynamic viscosity  $\mu = 0.04 \text{ g cm}^{-1} \text{ s}^{-1}$  and the density  $\rho = 1 \text{ g cm}^{-3}$ . The boundary conditions prescribe zero velocity on the walls and on the upstream section of the stenosed branch; on the upstream section of the bypass, an axial parabolic profile is prescribed, modulated by a waveform similar to the one illustrated in Fig. 13, yielding a peak velocity of

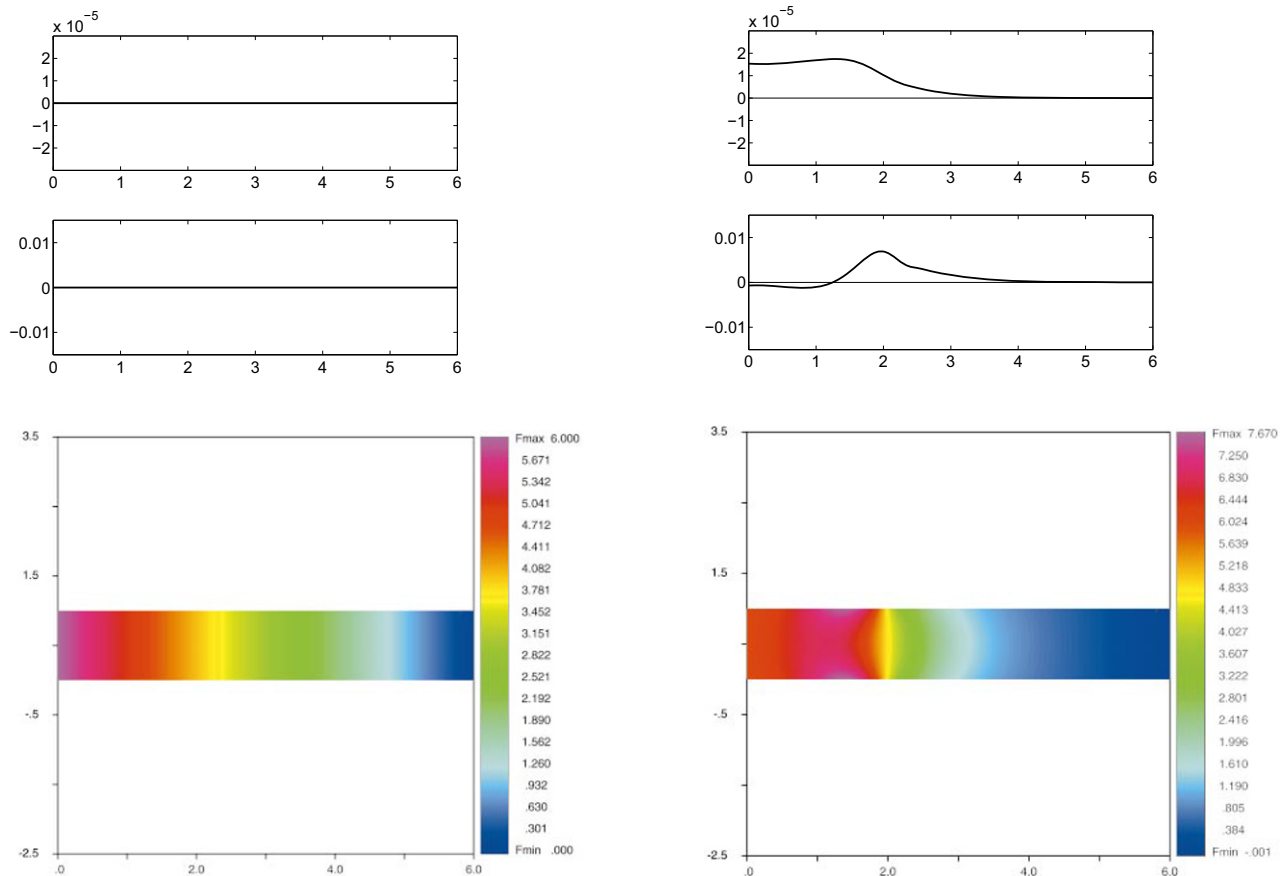
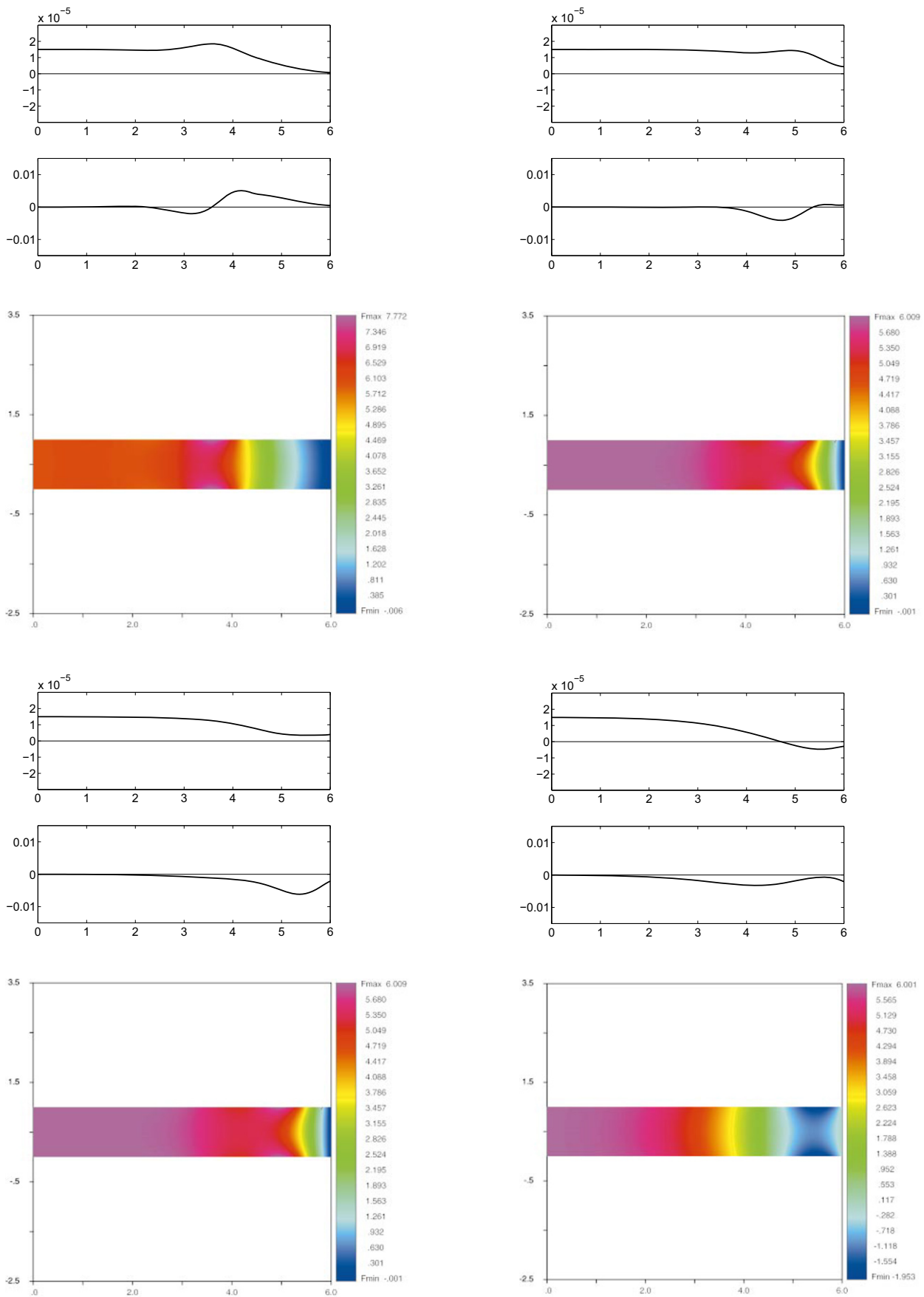
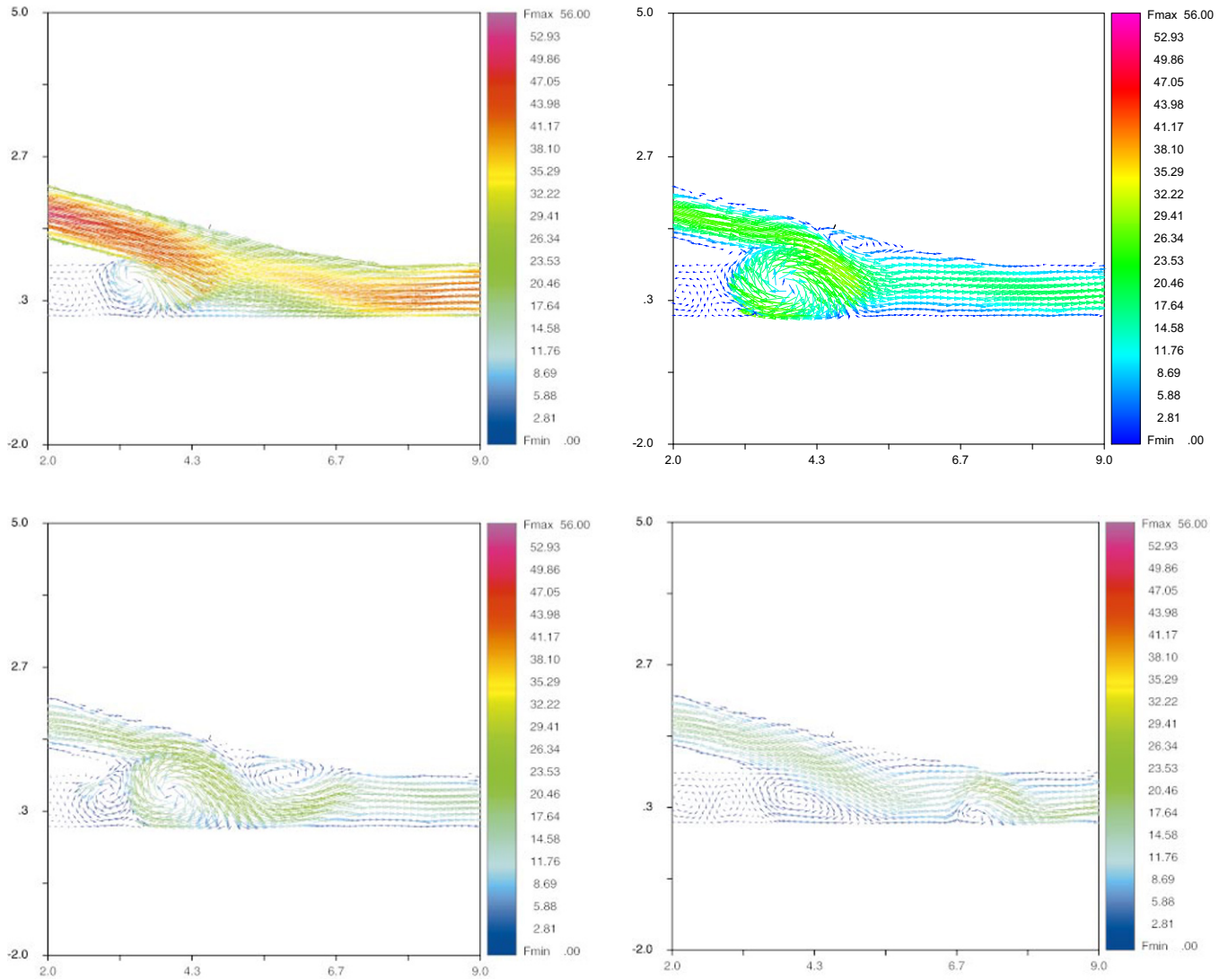


Fig. 33. Wall displacement, wall velocity and pressure in a 2D compliant pipe.  $t = 0$  s (left) and  $t = 0.000$  s (right)



**Fig. 34.** Wall displacement, wall velocity and pressure in a 2D compliant pipe.  $t = 0.012$  s (top, left),  $t = 0.016$  s (top, right),  $t = 0.018$  s (bottom, left) and  $t = 0.02$  s (bottom, right)



**Fig. 35.** Vector field for a 2D simple anastomosis morphology; different instants of the heart beat: peak flow (*top, left*) and initial deceleration phase (*top right*), middle deceleration (*bottom left*) and end of deceleration (*bottom, right*) phases

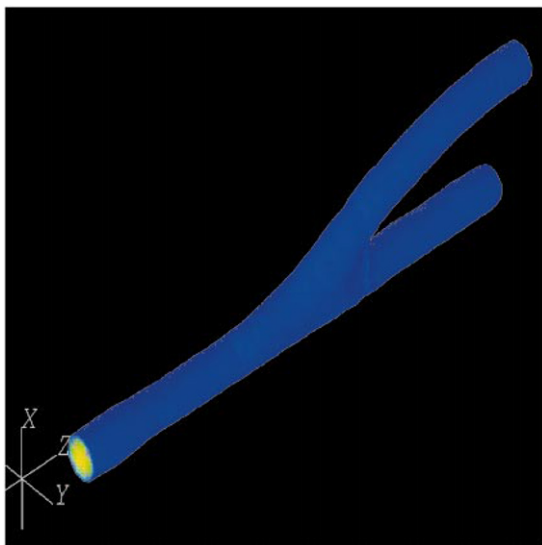


**Fig. 36.** Three-dimensional anastomosis reconstructed by a glass model. See [39]

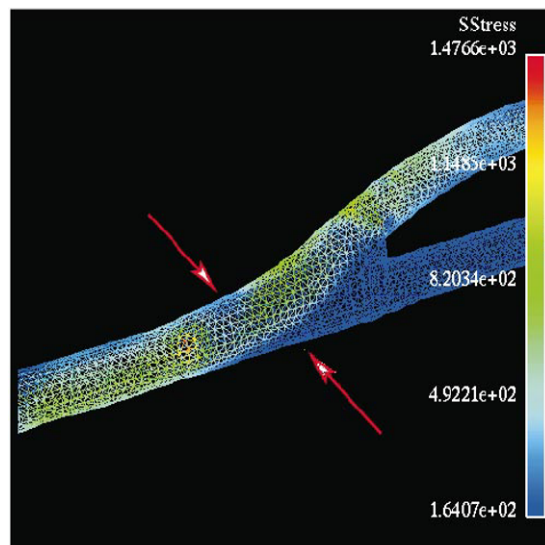


**Fig. 37.** Shear stress computed in the anastomosis of Fig. 36. The *red arrows* show the low shear stress zones

$56 \text{ cm s}^{-1}$ , corresponding to a flow rate of  $1320 \text{ ml min}^{-1}$  (“high flow rate” situation in [39]); on the downstream section, the Neumann condition  $(18)_2$  with  $d = 0$  is assigned.

The computations were carried out using a finite element discretization. The Yosida splitting was adopted for the time advancement. Figure 35 clearly illustrates the appearance and the evolution of the flow reversal zones during different phases of the heart beat.

A 3D numerical study aiming to identify the “optimal design” of the anastomosis morphology, based on the real surgical practice, can be found in [75].

#### 6.4 3D anastomosis model

The glass anastomosis model introduced in the previous subsection was reconstructed starting with a set of Computed Tomographies (see Fig. 36) and then adopted for a numerical simulation, in order to compare measured and computed velocity and pressure data. The results of this comparison are reported in [39]. Here, we limit ourselves to illustrating the magnitude of the shear stress computed on the model during the diastolic phase (see Fig. 35). The low shear stress zones (red arrows) at the toe of the junction are indeed associated with the flow reversal zones, and, as pointed out in Sect. 2, with reocclusion and failure of the bypass.

*Acknowledgements.* The authors wish to thank Dr. Gianluigi Zanetti, Eng. Luca Formaggia, Dr. Andrea Giachetti and all the Group of Biomedical Applications of CRS4. For more details about the simulations illustrated, see the web site [www.crs4.it](http://www.crs4.it). The numerical simulations of Figs. 31, 32 and 35 were carried out by N3S, by EDF-Simulog. The results are visualised by EnSight 5.5.

The authors thank also Eng. Fabio Nobile (Dép. Mathématique, EPFL, Lausanne) for the Figures in Sect. 6.2. Finally, the authors thank Prof. R. Pietrabissa (Dep. of Bioengineering, Technical University of Milan), Eng. G. Dubini (Dep. of Energetics, Technical University of Milan), Eng. G. Pennati (CeBiTec, S. Raffaele Hospital, Milan) and Eng. A. Remuzzi (“M. Negri” Institute for Pharmacological Researches, Bergamo) for some useful suggestions.

The work was supported by the Swiss National Science Foundation, Project N. 21-54139.98, by MURST 40% and “Fondi di Ateneo” Research Contracts, the CNR Special Project: “Mathematical Methods in Fluid Dynamics and Molecular Dynamics” and the CNR Special Project: “Mathematical Models and Methods in Biology: Modelling and Computational issues in Hemodynamics”.

#### References

- Abdoulav, G., Cadeddu, S., Delussu, G., Donizelli, M., Manzi, C., Formaggia, L., Giachetti, A., Gobetti, E., Leone, A., Pili, P., Schenine, A., Tuveri, M., Varone, A., Veneziani, A., Zanetti, G., Zorcolo, A. Viva: The virtual vascular project. *IEEE Transactions on Information Technology in Medicine* 4(2): 268–274 (1998)
- Aris, R.: *Vectors, tensors and the basic equations of fluid mechanics*. Englewood Cliffs: Prentice Hall 1962. Reprinted New York: Dover 1969
- Barbera, M.L.: Optimality in fluid transport systems. *Contemp. Math.* 141: 565–586 (1993)
- Begue, C., Conca, C., Murat, F., Pironneau, O.: *Les équations de Stokes et de Navier–Stokes avec des conditions aux limites sur la pression*. In Brezis, H., Lions, J. (eds.). *Nonlinear Partial Differential Equations and Their Applications*. Collège de France Seminar, Vol. IX. Pitman Research Notes in Mathematics, pp. 179–264. Harlow: Longman 1988
- Brezzi, F., Fortin, M.: *Mixed and Hybrid Finite Elements*. Springer Series in Computational Mathematics No. 15. New York: Springer 1991
- Bauters, C., Meurice, T., Hamon, M., McFadden, E., Lablanche, J., Bertrand, M.: Mechanisms and prevention of restenosis: from experimental models to clinical practice. *Cardiovascular Research* 31: 835–846 (1996)
- Bercovier, M., Pironneau, O.: Error estimates for finite element solution of the Stokes problem in the primitive variables. *Num. Math.* 33: 211–236 (1979)
- Bassiouny, H., White, S., Glagov, S., Choi, E., Giddens, D., Zarins, C.: Anastomotic intimal hyperplasia: mechanical injury or flow-induced. *J. Vasc. Surg.* 15: 708–717 (1992)
- Bank, A., Wang, H., Holte, J., Mullen, K., Shammass, R., Kubo, S.: Contribution of collagen, elastin and smooth muscle to in vivo human brachial artery wall stress and elastic modulus. *Circulation* 94: 3263–3270 (1996)
- Bank, A., Wilson, R., Kubo, S., Holte, J., Dresing, T., Wang, H.: Direct effects of smooth muscle relaxation and contraction on in vivo human brachial artery elastic properties. *Circ. Res.* 77: 1008–1016 (1985)
- Canfield, T., Dobrin, P.: Static Elastic Properties of Blood Vessels. In: Skalak, R., Chen, S. (eds.) *Handbook of Bioengineering*. New York: McGraw-Hill 1987
- Caro, C., Doorly, D., Tarnawski, M., Scott, K., Long, Q., Dumoulin, C.: Non-planar curvature and branching of arteries and non-planar-type flow. *Proc. Royal Soc. London A* 452: 185–197 (1996)
- Caro, C., Fitzgerald, G., Schroter, R.: Atheroma and arterial wall shear: Observation, correlation and proposal of a shear dependent mass transfer mechanism for atherogenesis. *Proc. Royal Soc. London Biol.* 117: 109–159 (1971)
- Chandran, K.: Flow Dynamics in the Human Aorta. *ASME J. Biomech. Eng.* 115: 611–616 (1993)
- Chorin, A.: *Numerical Solution of the Navier–Stokes Equations*. *Math. Comp.* 22: 745–762 (1968)
- Cowan, D., Langille, B.: Cellular and molecular biology of vascular remodeling. *Curr. Opin. Lipidol.* 7: 94–100 (1996)
- Cokelet, G.: The Rheology and Tube Flow of Blood. In: Skalak, R., Chen, S. (eds.) *Handbook of Bioengineering*. New York: McGraw-Hill 1987
- Dubini, G., de Laval, M., Pietrabissa, R., Montevecchi, F., Fumero, R.: A numerical fluid mechanical study of repaired congenital heart defects. Application to the Total Cavopulmonary Connection. *J. Biomech.* 29(1): 111–121 (1996)
- Donea, J., Giuliani, S.: An explicit ALE finite element formulation for 3D transient dynamic fluid-structure interaction problems. *ISPR Joint Research Centre Tech. Rep. EUR 11936 EN* (1989)
- Dierckx, P.: *Curve and Surface Fitting with Splines*. New York: Clarendon Press 1993
- Davies, P., Remuzzi, A., Gordon, E., Devey, C., Gimbrone, M.: Turbulent fluid shear stress induces vascular endothelial cell turnover in vitro. *Proc. Natl. Acad. Sci. USA* 83: 2114–2117 (1986)
- Donizelli, M., Schenine, A.: Distributed computational objects for image segmentation. *Technical report, CRS4* (1997)
- Errate, D., Esteban, M., Maday, Y.: Couplage fluide structure: un modèle simplifié. *Note aux C.R.A.S., Paris t. 318, Série, I* (1994)
- Friedman, M., Deters, O., Mark, F., Barger, C., Hutchins, G.M.: Arterial Geometry Affects Hemodynamics: a potential risk factor for Atherosclerosis. *Atherosclerosis* 46: 225–231 (1983)
- Fung, Y., Fronek, K., Patitucci, P.: Pseudoelasticity of arteries and the choice of its mathematical expression. *Am. J. Phys.* 237: H620–H631 (1979)
- Formaggia, L., Nobile, F.: A stability analysis for the arbitrary lagrangian eulerian formulation with finite elements. *East-West, J. Appl. Math.* 7(2): 105–131 (1999)
- Fry, D.: Acute vascular endothelial changes associated with increased blood flow gradients. *Circ. Res.* 22: 165–197 (1968)
- Fei, D., Thomas, J.D., Rittgers, S.E.: The Effect of Angle and Flow Rate Upon Hemodynamics in Distal Vascular Graft Anastomoses: A Numerical Model Study. *ASME J. Biomech. Eng.* 116: 331–336 (1994)
- Bassiouny, H.S., White, S., Glagov, S., Choi, E., Giddens, D.P., Zarins, C.K.: Intimal thickening: morphogenesis, functional significance and detection. *J. Vasc. Invest.* 1: 2–14 (1995)
- Guillard, H., Farhat, C.: On the significance of the geometric conservation law for flow computations on moving meshes. submitted (1998)

31. Grabowsky, E., Jaffe, E., Weksler, B.: Prostacyclin production by cultured human endothelial cells exposed to step increase in shear stress. *J. Lab. Clin. Med.* 105: 36–43 (1985)
32. Garcia, J., Lazar, V., McClain, L., Gallagher, P., Verin, A.: Myosin light chain kinase in endothelium: molecular cloning and regulation. *Am. J. Respir. Cell. Mol. Biol.* 16: 489–494 (1997)
33. Girault, V., Raviart, P.: Navier–Stokes Equations: Theory and Numerical Analysis. Springer Series in Computational Mathematics. Nr. 5. Berlin, Heidelberg: Springer 1986
34. Grandmont, M.: Analyse mathématique et numérique de quelques problèmes d’interaction fluide structure. Ph.D. Thesis, Université, P. et, M. Curie, Paris VI. (1997)
35. Gresho, P.: Some current CFD issues relevant to the incompressible Navier–Stokes equations. *Computer Methods in Applied Mechanics and Engineering* 87: 201–252 (1991)
36. Glagov, S., Weisenberg, E., Zarins, C., Stankunavicius, R., Kolettis, G.: Compensatory enlargement of human atherosclerotic coronary disease. *N. Engl. J. Med.* 316: 1371–1375 (1987)
37. Gyton, A.: Textbook of Medical Physiology. Philadelphia: Saunders 1986 (7th Edn.)
38. Glagov, S., Zarins, C.: Is intimal hyperplasia an adaptive response or a pathologic process? observation on the nature of non-atherosclerotic intimal thickening. *J. Vasc. Surg.* 10: 571–573 (1989)
39. Giachetti, A., Zanetti, G., Cadeddu, S., Tuveri, M., Staalsen, N.-H., Ringgaard, S.: Comparison between numerical flow simulations and mr measures on glass anastomosis models. submitted to Proceedings of VIII Mediterranean Conference on Medical and Biological Engineering and Computing (Medicon98), June 14–17. Limassol. Cyprus 1998
40. Holzapfel, G., Eberlein, R., Wriggers, P., Weizsacker, H.: Large strain analysis of soft biological membranes: formulation and finite element analysis. *Comp. Meth. Appl. Mech. Eng.* 123: 45–61 (1996)
41. Hilbert, D.: An efficient Navier–Stokes solver and its applications to fluid flow in elastic tubes. *Colloquia Societatis Janos Bolyai* 50: 423–431 (1987)
42. Hron, J., Málek, J.: A Numerical Investigation of Steady Flows of the Power-Law Fluids through Corrugated Channels. submitted (1997)
43. Hppensteadt, F., Peskin, C.: Mathematics in Medicine and the Life Sciences. Texts in Applied Mathematics. New York: Springer 1992
44. Harris, L., Ritman, E., Robb, R.: Computed Tomography and 3D Imaging. In: Skalak, R., Chen, S. (eds.). Handbook of Bioengineering. New York: McGraw-Hill 1987
45. Heywood, J., Rannacher, R., Turek, S.: Artificial Boundaries and Flux and Pressure Conditions for the Incompressible Navier–Stokes Equations. *International Journal for Numerical Methods in Fluids* 22: 325–352 (1996)
46. Hayden, M., Tyagi, S.: Arterial vascular remodeling: the endothelial cell’s central role. *Mo. Med.* 95: 213–217 (1998)
47. Hermiller, J., Tenaglia, A., Kisslo, K., Philips, H., Bashore, T., Stack, R., Davidson, C.: In vivo validation of compensatory enlargement of atherosclerotic coronary arteries. *Am. J. Card.* 71: 665–668 (1993)
48. Hughes, T., Taylor, C., Zarins, C.: Finite element modeling of blood flow in arteries. *Comp. Meth. Appl. Mech. Eng.* 158: 155–196 (1998)
49. Hughes, T., Zimmermann, T.K.: Lagrangian Eulerian Finite Element Formulation for Incompressible Viscous Flows. *Comp. Meth. Appl. Mech. Eng.* 29: 329–349 (1981)
50. Intaglietta, M.: Blood pressure and flow measurements. In: Skalak, R., Chien, S. (eds.) Handbook of Bioengineering, Chapt. 33. New York: McGraw-Hill (1987)
51. Ku, D., Giddens, D., Zarins, C. K., Glagov, S.: Pulsatile flow and atherosclerosis in the human carotid bifurcation. *Arteriosclerosis* 5: 293–302 (1985)
52. Langille, B.: Remodeling of developing and mature arteries: endothelium, smooth muscle and matrix. *J. Cardiovasc. Pharmacol.* 21: S11–S17 (1993)
53. Lesoinne, M., Farhat, C.: Geometric Conservation Laws for Aeroelastic Computations using Unstructured Dynamic Meshes. In AIAA (ed) 12th AIAA CFD Conference. American Institute of Aeronautics and Astronautics (1995)
54. Lions, J.: Quelques méthodes de résolution des problèmes non linéaires. Dunod: Paris 1969
55. Levesque, M., Liepsch, D., Moravec, S., Nerem, R.: Correlation of endothelial cell shape and wall shear stress in a stenosed dog aorta. *Arteriosclerosis* 6: 220–229 (1986)
56. LeTallec, P., Mouro, J.: Structures en grands déplacements couplées à des fluides en mouvement. Technical Report 2961. INRIA (1996)
57. LoGerfo, F., Nowak, M., Quist, W., Crawshaw, H., Bharadvaj, B.: Flow studies in a model of carotid bifurcation. *Arteriosclerosis* 1: 235–241 (1981)
58. Levesque, M., Sprague, E., Nerem, R.: Vascular endothelial cell proliferation in culture and the influence of flow. *Biomaterials* 11: 702–707 (1990)
59. Luscher TF V. P.: The endothelium: modulation of cardiovascular function. Boca Raton Fla: CRC Press 1990, pp. 1–215
60. Lou, Z., Yang, W.: A Computer Simulation of the Blood Flow at the Aortic Bifurcation with Flexible Walls. *ASME J. Biomech. Eng.* 115: 306–315 (1993)
61. Masawa, N., Glagov, S., Zarins, C.: Quantitative morphologic study of intimal thickening at the human carotid bifurcation: II. the compensatory enlargement response and the role of the intima in tensile support. *Atherosclerosis* 107: 147–155 (1994)
62. Ma, X., Lee, G., Wu, S.: Numerical Simulation for the propagation of Nonlinear Pulsatile Waves in Arteries. *ASME J. Biomech. Eng.* 114: 490–496 (1992)
63. Meurice, T., Vallet, B., Bauters, C., Dupuis, B., Lablanche, J., Bertrand, M.: Role of endothelial cells in restenosis after coronary angioplasty. *Fundam. Clin. Pharmacol.* 10: 234–242 (1996)
64. Nerem, R.: Vascular Fluid Mechanics, Arterial Wall and Atherosclerosis. *ASME J. Biomech. Eng.* 114: 274–282 (1992)
65. Nerem, R.: Hemodynamics and the vascular endothelium. *ASME J. Biomech. Eng.* 115: 510–514 (1993)
66. Lewis, R.: Tissue engineering now coming into its own as a scientific field. *The scientist* 9(15): 12–13 (1995)
67. Nikol, S., Huehns, T., Hofling, B.: Molecular biology and post-angioplasty restenosis. *Atherosclerosis* 123: 17–31 (1996)
68. Nichols, W., O’Rourke, M.: Mc Donald’s Blood Flow in Arteries. London: Edward Arnold Ltd. 1990, 3rd Edition
69. Nobile, F.: Fluid-structure interaction problems in hemodynamics. Master’s thesis. Technical University of Milan. in italian (1998)
70. Nobile, F., Veneziani, A.: Fluid-structure interaction in blood flow problems. In Proc. GAMM98. Bremen. ZAMM, Z. Angew. Math. Mech. 79(Suppl. 1): S255–S258 (1999)
71. Naruse, K., Yamada, T., Sokabe, M.: Involvement of sa channels in orienting response of cultured endothelial cells to cyclic stretch. *Am. J. Physiol.* 274: H1532–1538 (1998)
72. Pennati, G., Bellotti, M., Ferrazzi, E., Bozzo, M., Pardi, G., Fumero, R.: Blood flow through the ductus venosus in human fetus: calculation using doppler velocimetry and computational findings. *Ultrasound Med. Biol.* 24(4): 477–487 (1998)
73. Pedley, T.: The Fluid Mechanics of Large Blood Vessels. Cambridge: Cambridge University Press 1980
74. Peskin, C.: Numerical Analysis of Blood Flow in the Heart. *J. of Comp. Phys.* 25: 220–252 (1977)
75. Perktold, K., Hofer, M., Karner, G., Trubel, W., Schima, H.: Computer simulation of vascular fluid dynamics: optimal design of arteria bypass anastomoses. In Proceedings of ECCOMAS 98: pp.484–489. Chichester: Wiley 1998
76. Pironneau, O.: Méthodes des éléments finis pour les fluides. Paris: Masson 1988
77. Prasad, A., Logan, A., Nerem, R., Schwartz, C., Sprague, E.: Flow related responses of intracellular inositol phosphate levels in cultured aortic endothelial cells. *Circ. Res.* 72(4): 827–836 (1993)
78. Peskin, C., McQueen, D.: A Three-Dimensional Computational Method for Blood Flow in the Heart – I Immersed Elastic Fibers in a Viscous Incompressible Fluid. *J. of Comp. Phys.* 81(2): 372–405 (1989)
79. Perktold, K., Rappitsch, G.: Mathematical modeling of local arterial flow and vessel mechanics. In Crolet, J., Ohayon, R. (eds.) Computational Methods for Fluid Structure Interaction. Pitman Research Notes in Mathematics No. 306, pp. 230–245 Harlow: Longman 1994

80. Perktold, K., Rappitsch, G.: Computer simulation of Local Blood Flow and Vessel Mechanics in a Compliant Carotid Artery Bifurcation Model. *J. Biomech.* 28: 845–856 (1995)
81. Perktold, K., Rappitsch, G.: Computer simulation of Local Blood Flow and Vessel Mechanics in a Compliant Carotid Artery Bifurcation Model. *J. Biomech.* 28: 845–856 (1995)
82. Perktold, K., Resch, M., Florian, H.: Pulsatile Non-Newtonian Flow Characteristics in a Three-Dimensional Human Carotid Bifurcation Model. *ASME J. Biomech. Eng.* 113: 463–475 (1991)
83. Perktold, K., Resch, M., Florian, H.: Pulsatile Non-Newtonian Flow Characteristics in a Three-Dimensional Human Carotid Bifurcation Model. *ASME J. Biomech. Eng.* 113: 463–475 (1991)
84. Prouse, G.: On the motion of a viscous incompressible fluid in a tube with permeable and deformable wall. *Rend. Acc. Naz. Lincei, Classe di Scienze Matematiche, Fisiche e Naturali L, s. VIII:* pp. 663–675 (1971)
85. Prouse, G.: On the solution of a non-linear mixed problem for the Navier–Stokes equations in a time dependent domain. *Rend. Acc. Naz. Lincei, Classe di Scienze Matematiche, Fisiche e Naturali L, s. VIII:* pp. 293–298, 413–420, 531–537. Notes I, II and, III (1971)
86. Perktold, K., Thurner, E., Kenner, T.: Flow and stress characteristics in rigid walled and compliant carotid models. *Medic., Biol. Eng., Comp.* 32: 19–26 (1994)
87. Quarteroni, A., Saleri, F., Veneziani, A.: Factorization methods for the Numerical Approximation of Navier–Stokes equations. to appear in *Comp. Meth. Appl. Mech. Eng.*
88. Quarteroni, A., Saleri, F., Veneziani, A.: Analysis of the Yosida method for the numerical approximation of Navier–Stokes equations. *J. Math. Pure Appl. IX S., T. 78(5):* 473–504 (1999)
89. Quartapelle, L.: *Numerical Solution of the Incompressible Navier–Stokes Equations.* ISNM Vol. 113, Basel, Boston, Berlin: Birkhäuser 1993
90. Quarteroni, A., Valli, A.: *Numerical Approximation of Partial Differential Equations.* Springer Series in Computational Mathematics No. 23. Berlin, Heidelberg: Springer 1994
91. Quarteroni, A., Veneziani, A.: Modeling and Simulation of Blood Flow Problems. In *Computational Science for the 21<sup>st</sup> Century*, pp. 339–350. Chichester: Wiley 1997
92. Rajagopal, K.: Mechanics of Non-Newtonian Fluids. In: Galdi, G., Necas, J. (Eds.) *Recent Developments in Theoretical Fluid Mechanics.* Pitman Research Notes in Mathematics. No. 291, pp. 129–162. Harlow: Longman 1993
93. Rideout, V., Dick, D.: Difference-differential equations for fluid flow in distensible tubes. *IEEE Trans. Biomed. Eng. BME-14(3):* 171–177 (1967)
94. Rosales, O., Isales, C., Barrett, P., Brophy, C., Sumpio, B.: Exposure of endothelial cells to cyclic strain induces elevations of cytosolic  $Ca^{2+}$  concentration through mobilization of intracellular and extracellular pools. *Biochem. J.* 326: 385–392 (1997)
95. Ross, R.: The pathogenesis of atherosclerosis: A perspective for the 1990s. *Nature* 362: 801–809 (1993)
96. Rappitsch, G., Perktold, K.: Pulsatile albumin transport in large arteries: a numerical study. *ASME J. Biomech. Eng.* 118: 511–519 (1996)
97. Raviart, P., Thomas, J.: *Introduction à l'analyse numérique des équations aux dérivées partielles.* Paris: Masson 1983
98. Stary, H., Chandler, A., Dinsmore, R., Fuster, V., Glagov, S., Insull, W., Rosenfeld, M., Schaffer, S., Schwartz, C., Wagner, W., Wissler, R.: A definition of advanced types of atherosclerotic lesions and a histological classification of atherosclerosis. a report from the committee on vascular lesions of the council on arteriosclerosis, american heart association. *Arterioscler. Thromb. Vasc. Biol.* 15: 1512–1531 (1995)
99. Stary, H., Chandler, A., Glagov, S., Guyton, J., Insull, W., Rosenfeld, M., Schaffer, S., Schwartz, C., Wagner, W., Wissler, R.: A definition of initial, fatty streak and intermediate lesions of atherosclerosis. a report from the committee on vascular lesions of the council on arteriosclerosis, american heart association. *Circulation* 89: 2462–2478 (1994)
100. Solbert, L., Eggen, D.: Localization and sequence of development of atherosclerotic lesions in the carotid and vertebral arteries. *Circulation* 43: 711–724 (1971)
101. Sadeghipour, M., Hajari, B.: The pulsatile blood-flow in deformable vessels – Non Newtonian behaviour. In: Hochmuth, R., Langrana, N., Hefzy, M. (Eds.) *Proceedings of 1995 Bioengineering Conference, BED – Vol. 29.* ASME 1995
102. Shen, J., Lusinskas, F., Connolly, A., Dewey, C., Gimbrone, M.: Fluid shear stress modulate cytosolic free calcium in vascular endothelial cells. *Am. J. Physiol.* 262: C384–390 (1992)
103. Smith, G.D.: *Numerical Solution of Partial Differential Equations: Finite Difference Methods.* Appl. Math., Comp. Series. Oxford 1986
104. Suzuki, M., Naruse, K., Asano, Y., Okamoto, T., Nishikimi, N., Sakurai, T., Nimura, Y., Sokabe, M.: Up-regulation of integrin beta 3 expression by cyclic stretch in human umbilical endothelial cells. *Biochem. Biophys. Res. Commun.* 239: 372–376 (1997)
105. Sokabe, M., Naruse, K., Sai, S., Yamada, T., Kawakami, K., Inoue, M., Murase, K., Miyazu, M.: Mechanotransduction and intracellular signaling mechanisms for stretch-induced remodeling in endothelial cells. *Heart Vessels Suppl.* 12: 191–193 (1997)
106. Shi, Y., Pieniek, M., Fard, A., O'Brien, J., Zaleski, J.A.M.J.: Adventitial remodeling after coronary arterial injury. *Circulation* 93: 340–348 (1996)
107. Sprague, E., Steinbach, B., Nerem, R., Schwartz, C.: Influence of laminar steady-state fluid imposed wall shear stress on the binding, internalization, and degradation of low-density lipoproteins by cultured arterial endothelium. *Circulation* 76: 648–656 (1987)
108. Stiel, G., Stiel, L., Schofer, J., Donath, K., Mathey, D.: Impact of compensatory enlargement of atherosclerotic coronary arteries on angiographic assessment of coronary artery disease. *Circulation* 80: 1603–1609 (1989)
109. Sthebens, W.: Structural and architectural changes during arterial development and the role of hemodynamics. *Acta Anat. (Basel)* 157: 261–274 (1996)
110. Sato, M., Theret, D., Wheeler, L., Ohshima, N., Nerem, R.: Application of the micropipette technique to the measurement of the cultured porcine aortic endothelial cell viscoelastic properties. *ASME J. Biomech. Eng.* 112: 263–268 (1990)
111. Taylor, C.: *A computational framework for vascular disease investigation.* Ph. D. Thesis. Stanford University 1996
112. Temam, R.: Sur l'approximation de la solution des équations de Navier–Stokes par la méthode de pas fractionnaires (II). *Arch. Rat. Mech. Anal.* 33: 377–385 (1969)
113. Temam, R.: *Navier–Stokes Equations. Theory and Numerical Analysis.* Amsterdam: North-Holland (1986)
114. Taylor, C., Hughes, T., Zarins, C.: *Computational Investigations in Vascular Disease.* *Computers Physics* 10(3): 224–232 (1996)
115. Unthank, J., Fath, S., Burkhart, H., Miller, S., Dalsing, M.: Wall remodeling during luminal expansion of mesenteric arterial collaterals in the rat. *Circ. Res.* 79: 1015–1023 (1996)
116. Veneziani, A.: Boundary conditions for blood flow problems. In Brezzi, F., al. (Eds.) *Proc. ENUMATH97, Heidelberg*, pp. 596–605. World Scientific 1998
117. Veneziani, A.: Boundary Conditions for Blood flow Problems. In Brezzi, F. (ed.) *Proceedings of ENUMATH97.* pp. 596–605. River Edge: World Scientific 1998
118. Wells, D., Archie, J., Kleinstreuer, C.: The effect of carotid artery geometry on the magnitude and distribution of wall shear stress gradients. *J. Vasc. Surg.* 23: 667–678 (1996)
119. Westerhof, N., Bosman, F., Vries, C., Noordergraaf, A.: Analog studies of the human systemic arterial tree. *J. Biomech.* 2: 121–143 (1969)
120. White, F.: *Viscous Fluid Flow.* New York: McGraw-Hill 1986
121. Womersley, J.: Method for the calculation of velocity, rate of flow and viscous drag in arteries when the pressure gradient is known. *J. Physiol.* 127: 553–563 (1955)
122. Wechezak, A., Vigger, R., Sauvage, L.: Fibronectin and f-actin redistribution in cultured endothelial cells exposed to shear stress. *Lab. Invest.* 53: 639–647 (1985)
123. Wolf, S., Werthessen, N.: *Dynamics of arterial flow.* New York: Plenum Press 1976
124. Xu, X., Collins, M., Jones, C.: Flow studies in canine aortas. *ASME J. Biomech. Eng.* 114(11): 504–511 (1992)
125. Yeleswarapu, K.: *Evaluation of Continuum Models for Characterizing the Constitutive Behavior of Blood.* Ph. D. Thesis. University of Pittsburgh 1996
126. Zarins, C.: Hemodynamics in atherogenesis. In: Moore, W. (Ed.) *Vascular Surgery. A Comprehensive Review*, pp. 86–96. Philadelphia, PA: W.B. Saunders 1991
127. Zarins, C., Giddens, D., Bharadvaj, B., Sottiurai, V., Mabon, R.,

- Glagov, S.: Carotid Bifurcation Atherosclerosis: Quantitative Correlation of Plaque Localization with Flow Velocity Profiles and Wall Shear Stress. *Circ. Res.* 53: 502–514 (1983)
128. Zarins, C.K., Lu, C.T., Gewertz, B.L., Lyon, R.T., Rush, D., Glagov, S.: Arterial disruption and remodeling following balloon dilatation. *Surgery* 92: 1086–1095 (1982)
129. Zhang, H., Reggio, M., Trépanier, Y., Camarero, R.: Geometric form of the GCL for moving meshes and its implementation in CFD schemes. *Computers Fluids* 22(1): 9–23 (1993)
130. Zarins, C., Zatina, M., Giddens, D., Ku, D., Glagov, S.: Shear stress regulation of artery lumen diameter in experimental atherogenesis. *J. Vasc. Surg.* 5: 413–420 (1987)